DIRECT CARBON MEASUREMENTS IN ENHANCED WEATHERING FIELD EXPERIMENTS USING KIMBERLITE RESIDUES AND OLIVINE POWDER

A Thesis Submitted to the Committee on Graduate Studies in Partial Fulfillment of the Requirements for the Degree of Master of Science in the Faculty of Arts and Science

TRENT UNIVERSITY
Peterborough, Ontario, Canada
© Copyright by Zivi Raiden Schaffer 2024
Environmental and Life Sciences M.Sc. Graduate Program
September 2024

ABSTRACT

Direct carbon measurements in enhanced weathering field experiments using kimberlite residues and olivine powder

Zivi Raiden Schaffer

Dissolved inorganic carbon in drainage waters is a direct measurement of carbon dioxide (CO_2) removal from enhanced rock weathering (ERW) in soils. In this study, square-metre scale field experiments (2021–2023) were conducted in Peterborough Ontario, Canada, each amended with kimberlite residues from Gahcho Kué Diamond Mine (Northwest Territories, Canada) or olivine powder at high application rates (100–400 t/ha). Porewater chemistry data, coupled with a water budget analysis derived from precipitation and soil moisture data, were used to quantify solubility trapping by amendment weathering revealing maximum rates of 0.04 t CO_2/ha over 2 yr for olivine and 0.9 t CO_2/ha over 3 yr for kimberlite. This research presents kimberlite mine wastes as an ERW feedstock alternative to basalt as projects scale-up and require more rock. Additionally, high dosage monitoring plots ensure detection of a CO_2 removal signal in open systems and should be considered for large scale projects.

Keywords: Kimberlite, mine wastes, olivine, enhanced rock weathering, CO_2 removal, field study, carbon accounting, solubility trapping, soil amendment, water budget.

Co-authorship statements

Contributors to Chapter 2 research include Z.R. Schaffer, K. Rausis, I.M. Power, and C. Paulo. Schaffer wrote the chapter, prepared figures, prepared samples for reactivity analysis, conducted experiments, prepared and analyzed field samples, and interpreted the data. Rausis assisted in initial set-up and monitoring of the field experiments, analyzed samples collected in 2021, and contributed to the final editing of the chapter. Power conceptualized the study and contributed to all aspects of this chapter. Paulo conducted principal component analysis on the batch leach data. This chapter is being prepared for submission to Frontiers in Climate – Carbon Dioxide Removal.

Contributors to Chapter 3 research include Z.R. Schaffer, I.M. Power, and J. Aherne. Schaffer conducted the field experiments, wrote the chapter, prepared figures, and analyzed the data. Power conceptualized the study and assisted on all aspects of this chapter. Aherne assisted in PROFILE analysis and interpretation.

Acknowledgments

Funding was provided via the Ontario Graduate Scholarship and by the Natural Science and Engineering Research Council Grant to I.M. Power. Chapter 2 was a part of a research effort for Project CarbonVault in collaboration with DeBeers group of companies. Thank you first and foremost to my supervisor, Ian Power, whom I have had the privilege of learning from for the past four years, I am honoured to have had the opportunity to learn from him and consider myself very lucky. I promise to visit, if not for research purposes, then at least for Remy to finally meet Winslow.

I extend my sincere gratitude to Kwon Rausis for his instrumental influence on this journey when we first started at the Power Geolab, I have countless fond memories from the start of this study in 2021. In addition, thank you Julian Aherne for being on my supervisory committee and for meeting so spontaneously when I needed guidance (I primarily looked forward to our tangents). I'd like to recognize the staff at SGS Lakefield and Burnaby for analyzing the plenitude of samples I sent their way, De Beers Group of Companies for providing the kimberlite residues, Peter LaFleur for providing the crucial climate data required for this field study, and Marcel Dorken for allowing my field experiments to take up space in his experimental plot behind the DNA building for a whopping 4 years.

To my lab mates, how lucky am I to have found a family among good friends, each one of you has been a pillar supporting this research. Thank you to Duncan for your help and good conversation, I hope our little lunch treats will return someday. To Lance and Ben, thank you for the laughs and support throughout our undergrad. To Victoria, my first ever research assistant, I appreciate all the hard work and help in micronizing samples, taking down the field experiments, and always having a story to share, I always

looked forward to seeing you in the lab. Thank you to the rest of the PowerGeolab, and PowerGeolab alums of which our paths have crossed, you have made this journey most special.

Finally, thank you to all who have encouraged me and listened through my ramblings of new thesis findings and concepts learned. I owe it all to the support from my mum, dad, and step-mum, my brother Qewyn, and my grandparents, all whom I hope I've made proud. To John, thank you for your unwavering support. Last, a very special thank you to my roommates (Amy, Lily, Maddy, and Abby) for being there for the little wins and cheering me on during the big changes – I could not have done it without you four.

Table of Contents

Chapter 4: Conclusions

List of Figures

List of Tables

List of Abbreviations and Symbols

ERW	Enhanced rock weathering
CDR	Carbon dioxide removal
NET	Negative emissions technology
GHG	Greenhouse gas
MRV	Monitoring, reporting, and verification
DIC	Dissolved inorganic carbon
TIC	Total inorganic carbon
XRD	X-ray diffraction
XRF	X-ray fluorescence
CEC	Cation exchange capacity
SSA	Specific surface area
BET	Brunauer–Emmett–Teller
PSD	Particle size distribution
ICP-MS	Inductively coupled plasma mass spectroscopy
ICP-OES	Inductively coupled plasma optical emission spectroscopy
DOC	Dissolved organic carbon
TOC	Total organic carbon
IC	Ion chromatography
PCA	Principal component analysis
GEOROC	Geochemistry of Rocks of the Oceans and Continents
CAPMoN	Canadian Air and Precipitation Monitoring Network
GK	Gahcho Kué
FPK	Fine processed kimberlite
CPK	Coarse processed kimberlite
MOE	Ministry of the Environment
ECCC	Environment and Climate Change Canada
CCME	Canadian Council of Ministers of the Environment
BCw	Weatherable base cations
LOI	Loss on ignition
pCO_2	Partial pressure
MΩ	Milliohm
θ	Volumetric water content
ø	Diameter
‰	Permille
×	Times
ºC	Degree Celsius

Gt	Gigatonne
Mt	Megatonne
t	Tonne
kg	Kilogram
g	Gram
mg	Milligram
µg	Microgram
wt.%	Weight percent
mS	Millisiemens
L	Litre
mL	Millilitre
eq	Equivalents
keq	Kiliequivalents
ppm	Parts per million
mol	Mole
µmol	Micromole
µM	Micromolar
cmol	Centimole
M	Molar mass
yr	Year
mo	Month
d	Day
h	Hour
min	Minute
s	Second
ha	Hectare
km	Kilometre
m	Metre
cm	Centimetre
mm	Millimetre
µm	Micrometre
rpm	Rotations per minute
kPa	Kilopascals

Chapter 1
Introduction

1.1 Climatic change and carbon removal technologies

Atmospheric carbon dioxide (CO_2) concentrations, currently around 420 ppm, continue to increase by 20 ppm per decade as of 2000 (IPCC, 2021). This persistent rise, from pre-industrial levels (~280 ppm), significantly disrupts the natural course of the global climate system, prompting climate initiatives like the Paris Agreement, which aims to prevent CO_2 concentrations from increasing to irreversible levels (IPCC, 2021). Consequently, mitigating CO_2-facilitated climatic changes requires CO_2 removal (CDR) and stabilization, in addition to reducing global CO_2 emissions.

Under the Paris Agreement, signatories remain active in achieving carbon neutrality by 2050 through various CDR strategies, particularly through negative emission technologies (NETs). Established NETs include afforestation/reforestation, biochar applications, bioenergy with carbon capture and storage, direct air capture, ocean fertilization, and enhanced rock weathering (McLaren, 2012). These technologies aim to enhance the effectiveness of natural carbon sinks such as agricultural soils (Paustian et al., 1997), forested areas, and geological storage reservoirs (Voormeij and Simandl, 2004). Geochemical NETs, like enhanced rock weathering (ERW), are actively researched as scalable and feasible approaches to sequester mega to gigatonnes of atmospheric CO_2 using cationic alkaline minerals (Hartmann et al., 2013; Moosdorf et al., 2014; Goll et al., 2021; Campbell et al., 2022). ERW involves accelerating the dissolution of Ca- and Mg-silicate minerals to permanently store CO_2 in a stable aqueous form (bicarbonate) or solid phase (carbonate mineral; Power et al., 2013b; Renforth et al., 2015; Bullock et al., 2021). Natural silicate dissolution removes ~1.1 Gt of atmospheric

CO_2 annually, with the goal of ERW to amplify this process by finely grinding rocks and distributing them over land surfaces (Strefler et al., 2018a). With approximately 11.8–14.7 million square kilometres of suitable agricultural land globally, ERW is equipped with proper management and accessibility (Moosdorf et al., 2014; Almaraz et al., 2022). Furthermore, dispersal of rock powders over croplands could potentially benefit crop yield by releasing nutrients, thereby fostering collaboration with the agriculture industry to introduce these carbon removal techniques into regular practice (Lewis et al., 2021; Almaraz et al., 2022).

1.2 Enhanced rock weathering fundamentals

Ultramafic rocks, mined at a rate of ~420 Mt annually, contain the necessary target minerals suitable for carbon sequestration (Power et al., 2013a). Certain rock powders exhibit significant geochemical capacities for carbon sequestration (Pronost et al., 2011; Mervine et al., 2018; Paulo et al., 2021; Stubbs et al., 2022) and leach beneficial elements that improve soil environments upon mineral dissolution (Gras et al., 2020; Hamilton et al., 2020; Gunnarsen et al., 2023; te Pas et al., 2023). Well-established minerals considered in feedstock assessments include the hydroxide mineral brucite [$Mg(OH)_2$;Harrison, Power and Dipple, 2013], the Ca- and Mg-silicate minerals wollastonite and forsterite (Daval et al., 2009; Renforth, Pogge von Strandmann and Henderson, 2015; Oelkers et al., 2018), and serpentine group silicates such as lizardite [$Mg_3Si_2O_5(OH)_4$; Power, Wilson and Dipple, 2013]. These minerals, prevalent in mafic and ultramafic rocks, are ideal for ERW as they are minerally reactive and readily accessible via mining abundance (Power et al., 2013a).

Despite the generally slow weathering of silicate minerals due to silica polymerization which indicates an increased number of Si–O–Si bonds, wollastonite ($CaSiO_3$) with weaker Ca–O bonds and forsterite (Mg_2SiO_4) featuring unpolymerized structures facilitate faster dissolution mechanics (Power et al., 2013a; Oelkers et al., 2018). Moreover, these minerals are thermodynamically favourable for converting CO_2 into stable phases, such as carbonate minerals or bicarbonate and carbonate ions in fluids (e.g., $CaCO_3$(s), HCO_3^-(aq), or CO_3^{2-}(aq); Power et al., 2013). Estimates compiled by Oelkers et al. (2008) indicate the theoretical amount of mineral feedstock needed to sequester one ton of carbon, with wollastonite requiring 9.68 tonnes, forsterite 5.86 tonnes, and serpentine 7.69 tonnes, assuming complete carbonation (Table 1.1).

Table 1.1. Reaction mechanisms of wollastonite, forsterite, and lizardite with CO_2.

	Weathering reaction	Weathering products	Carbonation reaction	Carbonation products
Wollastonite: $CaSiO_3$	$+ H_2O + 2CO_2$	$Ca^{2+} + 2HCO_3^- + SiO_2$	$+ CO_2$	$CaCO_3 + SiO_2$
Forsterite: Mg_2SiO_4	$+ 4H_2O + 4CO_2$	$2Mg^{2+} + 4HCO_3^- + H_4SiO_4$	$+2CO_2$	$2MgCO_3 + SiO_2$
Lizardite: $Mg_3Si_2O_5(OH)_4$	$+ 5H_2O + 6CO_2$	$3Mg^{2+} + 6HCO_3^- + 2H_4SiO_4$	$+ 3CO_2$	$3MgCO_3 + 2SiO_2 + 2H_2O$

Silicate dissolution directly affects carbon sequestration, facilitated by the neutralization reaction between silicate minerals and carbonic acid. This reaction enables carbon dissociation into a soluble phase (weathering product: HCO_3^- i.e., solubility trapping; Table 1.1) and potentially leads to the precipitation of carbonate minerals from available cations (carbonation product: M^{2+}-CO_3 i.e., mineral trapping; Table 1.1). Solution pH governs the solubilization of CO_2 and determines the dominant form of carbon speciation (e.g., H_2CO_3, HCO_3^-, or CO_3^{2-}); therefore, as most minerals dissolve

more rapidly in acidic pH environments, the liberation of cations enables alkalinity generation, neutralizing pH (Power et al., 2013a).

Aqueous CO_2 in equilibrium with the atmosphere (Eq. 1) hydrates to form carbonic acid (Eq. 2), driving the dissolution of minerals. This process buffers the reacting solution and generates bicarbonate (Eq. 3) and carbonate anions (Eq. 4) in solution. Under relatively neutral pH conditions, HCO_3^- formation predominates, while alkaline pH levels promote reactions between dissolved divalent cations and CO_3^{2-} anions favouring carbonate precipitation, such as calcite, from solution (Eq. 5; Follett et al., 2001; Power et al., 2013a).

$$CO_{2(g)} \leftrightarrow CO_{2(aq)} \quad (1)$$

$$CO_{2(aq)} + H_2O \leftrightarrow H_2CO_3 \quad (2)$$

$$H_2CO_3 \leftrightarrow HCO_3^- + H^+ \quad (3)$$

$$HCO_3^- \leftrightarrow CO_3^{2-} + H^+ \quad (4)$$

$$CO_3^{2-} + Ca^{2+} \leftrightarrow CaCO_3 \quad (5)$$

Feedstock selection for ERW applications is guided by several criteria including the presence of fast-reacting silicate phases, minimal carbonate content, potential co-benefits (e.g., nutrient input), and low risk of deleterious metal leaching (e.g., Ni and Cr). Physical characteristics also influence the attractiveness of rock material for dispersal, such as fine particle sizes and high surface areas (Schuiling and Krijgsman, 2006; Renforth et al., 2015). Augmenting grain size has demonstrated a 2× increase in weathering rate of crushed basalt to the silt-dominated fraction (<45 μm) from sand-sized grains (150–500 μm), exhibiting a CDR difference of ~4 t CO_2/ha/yr (Vanderkloot and Ryan, 2023). However, crushing processes contribute additional CO_2 emissions,

complicating the overall carbon balance (Hangx and Spiers, 2009). Alternatively, natural repositories of crushed rock (e.g., glacial rock flour; Dietzen and Rosing, 2023) and pre-pulverized mine residues deposited on the surface offer ready-made options for ERW applications (Power et al., 2024).

While mineral, geochemical, and physical assessment of a feedstock will determine its CDR capacity, the actual rates of CDR will depend on the environmental conditions at the application site. Promoting silicate dissolution can naturally be achieved by opting for climate-favourable deployment sites. Tropical regions, characterized by higher temperatures and frequent precipitation, accelerate natural mineral weathering rates, whereas arid and polar climates with lower moisture content and less favourable temperatures are considered less suitable for ERW (Power et al., 2013a; Moosdorf et al., 2014). Temperature increases have been shown to significantly enhance dissolution rates (Sverdrup and Warfvinge, 1993; White et al., 1999), with estimates suggesting a 4–14% increase per degree Celsius rise (Gislason et al., 2009). Enhanced fluid exposure (i.e., carbonic acid in precipitation) through greater annual precipitation or increased fluid:rock ratios achieved by application rate, further facilitates dissolution of recalcitrant silicates (Moosdorf et al., 2014; Stubbs et al., 2022; Thorben et al., 2022). Therefore, worked croplands in monsoonal climates (e.g., Malaysia; Larkin et al., 2022) are ideal locations for deploying ERW trials. However, continental climates characterized by significant annual variation (e.g., moderate to hot summers and cold winters) govern wetting and drying cycles where mineral weathering is greatest upon the start of the wetter season (Stubbs et al., 2022).

1.3 Carbon sequestration at mine sites

Ultramafic mine residues possess high reactive surface areas due to their comminution and contain abundant Ca- and Mg-silicates, enabling passive carbonation rates that can sequester up to 10 kg CO_2 per tonne of rock (Power et al., 2013b). The weathering of alkaline residues releases divalent cations, facilitating significant mineral trapping by precipitating secondary Mg-carbonates, including hydromagnesite [$Mg_5(CO_3)_4(OH)_2 \cdot 4H_2O$], dypingite [$Mg_5(CO_3)_4(OH)_2 \cdot 5H_2O$], and nesquehonite [$MgCO_3 \cdot 3H_2O$] on-site if mineral precipitation kinetics are favourable (Wilson et al., 2011, 2014). Accelerated carbonation techniques, such as injection of CO_2-rich fluids or gases (~10–20% CO_2), have substantially improved in-situ CDR rates by over two orders of magnitude (reviewed by Power et al., 2013a). However, the implementation of injection infrastructure is costly and requires rigorous management. Instead, passive CDR by ultramafic residues is achievable by improving CO_2 supply through management modifications (e.g., larger residue impoundments) or manual spreading over the mine site (i.e., ERW).

Some mining by-products that suit the mineral and physical requirements for ERW include brucite-bearing nickel mine wastes (Pronost et al., 2011; Harrison et al., 2013; Wilson et al., 2014; Power et al., 2020), basalts (Dessert et al., 2003; Oelkers et al., 2008), and kimberlite residues produced from diamond mining (Wilson et al., 2011; Mervine et al., 2018; Paulo et al., 2021; Stubbs et al., 2022; Zeyen et al., 2022). Processed kimberlite, which has a global land footprint of 110–450 km^2 (Paulo et al., 2023), has become a well-researched feedstock for NET applications (Wilson et al., 2011; Mervine et al., 2018; Paulo et al., 2021; Stubbs et al., 2022; Zeyen et al., 2022). In-situ CDR rates for processed kimberlite residues are estimated at 4.7 t CO_2/ha/yr in South Africa (Stubbs

et al., 2022; Paulo et al., 2023) and 3.8–5.1 t CO_2/ha/yr in sub-arctic Canada diamond mines (Paulo et al., 2023). Comparatively, nickel mine wastes exhibit faster CDR rates estimated at ~39 t CO_2/ha/yr (Wilson et al., 2014), highlighting the advantageous reactivity of phases like brucite. These documented CDR rates applied a variety of methodologies, including mineralogical and total inorganic carbon assessments, isotopic analyses, and geochemical modelling; however, these approaches rarely assess solubility trapping due to the difficulty in tracking fluid flows, and there are uncertainties regarding how representative these approaches are for the entire residue impoundment (Wilson et al., 2014).

Environmental rehabilitation practices post-mine closure encompasses land restoration, water management, and stakeholder engagement. Yet, an often-overlooked aspect of environmental remediation consists of the cumulated CO_2 emissions over the lifetime of the mine. Mining activities contribute ~2% of global anthropogenic GHG emissions (ICMM, 2012); thus, enhancing CDR rates of mineralogically suitable residues by implementing ERW strategies could lead to carbon-neutralizing of the industry. Furthermore, integrating ERW into mine closure practices can promote long-term CO_2 removal post-closure, potentially reclaiming historic emissions and benefiting land remediation efforts depending on nutrient release. Nevertheless, hesitancy to adopt ERW remains due to the lack of standardized carbon accounting methodologies for open systems.

1.4 Carbon accounting methods

In laboratory settings, methods are standardized and repeatable, enabling accurate determination of mineral dissolution and subsequent CDR rates under controlled conditions. However, field experiments, which aim to condense geologic processes to shorter timescales, face the challenge of climatic randomness (Almaraz et al., 2022). The wide variability of soil types and difficulty in tracking carbon in its various forms in field conditions (e.g., solid vs. aqueous; Renforth et al., 2015) further add to the complexity. For instance, a column experiment investigating the influence of temperature on forsterite CDR reported rates of 0.03 t CO_2/yr at 4ºC and 0.2 t CO_2/yr at 19ºC, illustrating the enhanced dissolution effectiveness in warmer climates (Pogge von Strandmann et al., 2022). Yet, translating laboratory-derived dissolution rates into field sequestration rates, let alone theorized kinetics (e.g., one tonne of fine-grained forsterite sequesters 0.125 t of CO_2 per year), provides an inaccurate portrayal of natural CDR. Even when experiments are conducted in field conditions (e.g., outdoor column experiments), they often overlook chemical efflux and biological influences from local soils, leading to overestimations of naturally slowed weathering rates (Renforth et al., 2015).

To accurately quantify carbon removal, ERW projects require active monitoring and a method for directly measuring stable carbon generation in soil environments. Element proxies, in lieu of direct carbon measurements, are used as an indicator for mineral weathering which are then extrapolated to CDR rates. Rather than assuming ERW impacts to the net carbon budget via cation release, it is most reliable to monitor the various carbon pools: dissolved inorganic carbon (DIC) in porewaters, total inorganic carbon (TIC) in soils, surface CO_2 emissions, sub-surface pore gas CO_2 concentrations, and stable C isotope ratios (Almaraz et al., 2022). Still, tracking weathering products

(e.g., Mg-fluxes) to estimate mineral dissolution rates and monitor nutrient and metal release from feedstocks is beneficial. However, Ca and Mg cations will likely exchange with reactive sites and form pedogenic carbonates in favourable environments (Clarkson et al., 2024), resulting in lower porewater detection despite abundant leaching from ERW-suitable rock powders.

Simple and inexpensive verification platforms for quantifying carbon sequestration employ various methodologies tied to land management practices (Smith et al., 2020). Numerous ERW experiments utilize porewater alkalinity measurements to quantify HCO_3^- generation via solubility trapping (Larkin et al., 2022; Vienne et al., 2022; te Pas et al., 2023), although this method requires accurate water budget accounting when applied to an open system and has primarily been used in contained experiments or catchment water studies. Mineral trapping in ERW studies is typically assessed through TIC measurements using coulometry or by the difference between total carbon and total organic carbon (Manning et al., 2013; Haque et al., 2020b; Vienne et al., 2022). Although widely used, small TIC increases exhibit large uncertainties due to soil heterogeneity (Vienne et al., 2022).

Beyond carbon accounting, field trials must characterize interactions between feedstocks and the environment, particularly with soils. Soils feature pre-existing minerals that readily dissolve and precipitate, possess unquantified natural CO_2 sink or source capacities, and exhibit extreme chemical and physical variability (Almaraz et al., 2022). Other weathering processes affecting signals from amendment silicate dissolution include secondary mineral precipitation, carbonate weathering, and surface passivation, where mineral surface coatings inhibit further dissolution (Renforth et al., 2015; Almaraz et al., 2022). Long-term environmental impacts of mineral weathering are often

overlooked; for instance, applications of rock dust raise concerns about potential eutrophication, adverse effects on biodiversity, and unknown impacts on air and soil quality that manifest over time (Goll et al., 2021). Moreover, weathering of alkaline feedstocks threatens to accumulate deleterious metals in soils and porewaters, posing risks to ecosystem health (Dupla et al., 2023). Understanding these processes comprehensively at deployment sites is crucial for predicting long-term CDR, necessitating direct monitoring methods for quantifying removed carbon.

1.5 Geochemical modelling of mineral weathering rates

Geochemical models used to estimate CO_2 sequestration potential can range from simple programs that consider only the physical characteristics of a mineral to more comprehensive models that incorporate mineral dissolution kinetics and environmental conditions (Calabrese et al., 2022). However, these models attempt to predict natural weathering rates by extrapolating pre-determined laboratory rates, leading to an overestimation of CDR rates. Inverse geochemical models have successfully estimated passive carbonation rates at mine sites verified by mineralogical assessments (Paulo et al., 2023). By developing a mass-balance model from data retrieved from routine water sampling of residue impoundments and groundwater, Paulo et al. (2023) demonstrated how model verification and predictions can become integrated into CDR management within the mining industry.

PROFILE is a steady-state geochemical model used to calculate cation release (e.g., Ca and Mg) from mineral weathering in soils by applying mineral stoichiometry and reaction factors with 26 site-specific soil properties to account for soil variability (Hodson

et al., 1995; Phelan et al., 2014). In addition to soil morphology, PROFILE considers ecosystem parameters, including vegetation and climate (Sverdrup et al., 2019). Therefore, PROFILE can add to interpretations of field experiments by providing information on the reactions between mineral surfaces and water molecules or aqueous hydrogen ions, CO_2, organic ligands, and hydroxy ions (Sverdrup et al., 2019). PROFILE has been proposed for ERW use due to its success in modelling regional and catchment scale soil weathering rates (Taylor et al., 2017). Moreover, this model could assess various climatic data, surface areas, densities, and soil types, establishing a valuable predictive tool for the success of ERW projects.

1.6 Research objectives

Applications of forsterite and forsterite-bearing rocks dominate ERW field experiments with varying methodologies for carbon accounting. The two main goals of this research were to directly measure and quantify CDR by alkaline feedstocks applied to an open soil system and to assess ultramafic residues from diamond mining for ERW applications as an alternative feedstock for CDR.

Chapter 2 primarily consisted of a field trial initiated in 2021 where fine-processed kimberlite residues from De Beers' Gahcho Kué Diamond Mine (Northwest Territories, Canada) were amended to soil plots at Trent University in Peterborough, Ontario, Canada. Initial reactivity assessments using batch leaches with CO_2 determined cation release from the kimberlite versus the soil and were used to partition CDR from silicate and carbonate weathering. The primary objective of this study was to develop a methodology for measuring CO_2 removal rates of a mineralogically complex feedstock,

whereas secondary objectives consisted of assessing the potential environmental impacts and co-benefits of using alkaline mine wastes as a soil amendment.

Chapter 3 reapplied the carbon accounting method developed in Chapter 2, to assess a commonly used ERW silicate feedstock under field conditions. This study used pulverized forsterite (olivine Mg-endmember), which simplified measuring CO_2 removal rates due to the monomineralic application. The objectives of this experiment were to compare CDR rates calculated here to the wide range of reported forsterite dissolution rates under various conditions (e.g., laboratory vs. column vs. field) with consideration of soil-mineral interactions influencing the final removal. Secondary objectives included monitoring the release of elements of concern (e.g., Ni and Cr) from high dosages of alkaline minerals and evaluating a geochemical model with field data and site characteristics. These research efforts will contribute vital field data necessary for measuring and reporting CDR rates derived from a direct carbon monitoring method, while assessing the potential for repurposing an abundant mine waste to aid carbon removal efforts on a global scale.

1.7 References

Almaraz, M., Bingham, N. L., Holzer, I. O., Geoghegan, E. K., Goertzen, H., Sohng, J., et al. (2022). Methods for determining the CO_2 removal capacity of enhanced weathering in agronomic settings. *Frontiers in Climate* 4:970429, 1–18. doi: 10.3389/fclim.2022.970429

Bullock, L. A., James, R. H., Matter, J., Renforth, P., and Teagle, D. A. H. (2021). Global carbon dioxide removal potential of waste materials from metal and diamond mining. *Frontiers in Climate* 3, 694175. doi: 10.3389/fclim.2021.694175

Calabrese, S., Wild, B., Bertagni, M. B., Bourg, I. C., White, C., Aburto, F., et al. (2022). Nano- to global-scale uncertainties in terrestrial enhanced weathering. *Environ Sci Technol* 56, 15261–15272. doi: 10.1021/acs.est.2c03163

Campbell, J. S., Foteinis, S., Furey, V., Hawrot, O., Pike, D., Aeschlimann, S., et al. (2022). Geochemical negative emissions technologies: Part I. review. *Frontiers in Climate* 4:879133. doi: doi: 10.3389/fclim.2022.879133

Clarkson, M. O., Larkin, C. S., Swoboda, P., Reershemius, T., Suhrhoff, T. J., Maesano, C. N., et al. (2024). A review of measurement for quantification of carbon dioxide removal by enhanced weathering in soil. *Frontiers in Climate* 6, 1345224. doi: 10.3389/fclim.2024.1345224

Daval, D., Martinez, I., Corvisier, J., Findling, N., Goffé, B., and Guyot, F. (2009). Carbonation of Ca-bearing silicates, the case of wollastonite: Experimental investigations and kinetic modeling. *Chem Geol* 265, 63–78. doi: 10.1016/j.chemgeo.2009.01.022

Dessert, C., Dupré, B., Gaillardet, J., François, L. M., and Allègre, C. J. (2003). Basalt weathering laws and the impact of basalt weathering on the global carbon cycle. *Chem Geol* 202, 257–273. doi: 10.1016/j.chemgeo.2002.10.001

Dietzen, C., and Rosing, M. T. (2023). Quantification of CO_2 uptake by enhanced weathering of silicate minerals applied to acidic soils. *International Journal of Greenhouse Gas Control* 125, 103872. doi: 10.1016/j.ijggc.2023.103872

Dupla, X., Möller, B., Baveye, P. C., and Grand, S. (2023). Potential accumulation of toxic trace elements in soils during enhanced rock weathering. *Eur J Soil Sci* 74, e13343. doi: 10.1111/ejss.13343

Follett, R. F., Kimble, J. M., and Lal, R. (2001). *The potential of U.S. grazing lands to sequester carbon and mitigate the greenhouse effect*. Lewis Publishers.

Gislason, S. R., Oelkers, E. H., Eiriksdottir, E. S., Kardjilov, M. I., Gisladottir, G., Sigfusson, B., et al. (2009). Direct evidence of the feedback between climate and weathering. *Earth Planet Sci Lett* 277, 213–222. doi: 10.1016/j.epsl.2008.10.018

Goll, D. S., Ciais, P., Amann, T., Buermann, W., Chang, J., Eker, S., et al. (2021). Potential CO_2 removal from enhanced weathering by ecosystem responses to powdered rock. *Nat Geosci* 14, 545–549. doi: 10.1038/s41561-021-00798-x

Gras, A., Beaudoin, G., Molson, J., and Plante, B. (2020). Atmospheric carbon sequestration in ultramafic mining residues and impacts on leachate water chemistry at the Dumont Nickel Project, Quebec, Canada. *Chem Geol* 546. doi: 10.1016/j.chemgeo.2020.119661

Gunnarsen, K. C., Jensen, L. S., Rosing, M. T., and Dietzen, C. (2023). Greenlandic glacial rock flour improves crop yield in organic agricultural production. *Nutr Cycl Agroecosyst* 126, 51–66. doi: 10.1007/s10705-023-10274-0

Hamilton, J. L., Wilson, S. A., Morgan, B., Harrison, A. L., Turvey, C. C., Paterson, D. J., et al. (2020). Accelerating mineral carbonation in ultramafic mine tailings via direct CO_2

reaction and heap leaching with potential for base metal enrichment and recovery. *Economic Geology* 115, 303–323. doi: 10.5382/ECONGEO.4710

Hangx, S. J. T., and Spiers, C. J. (2009). Coastal spreading of olivine to control atmospheric CO_2 concentrations: A critical analysis of viability. *International Journal of Greenhouse Gas Control* 3, 757–767. doi: 10.1016/j.ijggc.2009.07.001

Haque, F., Santos, R. M., and Chiang, Y. W. (2020). CO_2 sequestration by wollastonite-amended agricultural soils – An Ontario field study. *International Journal of Greenhouse Gas Control* 97. doi: 10.1016/j.ijggc.2020.103017

Harrison, A. L., Power, I. M., and Dipple, G. M. (2013). Accelerated carbonation of brucite in mine tailings for carbon sequestration. *Environ Sci Technol* 47, 126–134. doi: 10.1021/es3012854

Hartmann, J., West, A. J., Renforth, P., Köhler, P., De La Rocha, C. L., Wolf-Gladrow, D. A., et al. (2013). Enhanced chemical weathering as a geoengineering strategy to reduce atmospheric carbon dioxide, supply nutrients, and mitigate ocean acidification. *Reviews of Geophysics* 51, 113–149. doi: 10.1002/rog.20004

Hodson, M. E., Langan, S. J., and Wilson, M. J. (1995). A critical evaluation of the use of the PROFILE model in calculating mineral weathering rates. *Water Air Soil Pollut* 98, 79–104.

ICMM (2012). The role of minerals and metals in a low carbon economy.

IPCC (2021). Summary for policymakers. In: Climate change 2021: The physical science basis. Contribution of working group I to the sixth assessment report of the Intergovernmental Panel on Climate Change.

Larkin, C. S., Andrews, G. M., Pearce, C. R., Yeong, K. L., Beerling, D. J., Bellamy, J., et al. (2022). Quantification of CO_2 removal in a large-scale enhanced weathering field trial on an oil palm plantation in Sabah, Malaysia. *Frontiers in Climate* 4:959229, 1–20.

Lewis, A. L., Sarkar, B., Wade, P., Kemp, S. J., Hodson, M. E., Taylor, L. L., et al. (2021). Effects of mineralogy, chemistry and physical properties of basalts on carbon capture potential and plant-nutrient element release via enhanced weathering. *Applied Geochemistry* 132, 105023. doi: 10.1016/j.apgeochem.2021.105023

Manning, D. A. C., Renforth, P., Lopez-Capel, E., Robertson, S., and Ghazireh, N. (2013). Carbonate precipitation in artificial soils produced from basaltic quarry fines and composts: An opportunity for passive carbon sequestration. *International Journal of Greenhouse Gas Control* 17, 309–317. doi: 10.1016/j.ijggc.2013.05.012

McLaren, D. (2012). A comparative global assessment of potential negative emissions technologies. *Process Safety and Environmental Protection* 90, 489–500. doi: 10.1016/j.psep.2012.10.005

Mervine, E. M., Wilson, S. A., Power, I. M., Dipple, G. M., Turvey, C. C., Hamilton, J. L., et al. (2018). Potential for offsetting diamond mine carbon emissions through mineral carbonation of processed kimberlite: an assessment of De Beers mine sites in South Africa and Canada. *Mineral Petrol* 112, 755–765. doi: 10.1007/s00710-018-0589-4

Moosdorf, N., Renforth, P., and Hartmann, J. (2014). Carbon dioxide efficiency of terrestrial enhanced weathering. *Environ Sci Technol* 48, 4809–4816. doi: 10.1021/es4052022

Oelkers, E. H., Declercq, J., Saldi, G. D., Gislason, S. R., and Schott, J. (2018). Olivine dissolution rates: A critical review. *Chem Geol* 500, 1–19. doi: 10.1016/j.chemgeo.2018.10.008

Oelkers, E. H., Gislason, S. R., and Matter, J. (2008). Mineral carbonation of CO_2. *Elements* 4, 333–337. doi: 10.2113/gselements.4.5.333

Olsson, J., Bovet, N., Makovicky, E., Bechgaard, K., Balogh, Z., and Stipp, S. L. S. (2012). Olivine reactivity with CO_2 and H2O on a microscale: Implications for carbon sequestration. *Geochim Cosmochim Acta* 77. doi: 10.1016/j.gca.2011.11.001

Paulo, C., Power, I. M., Stubbs, A. R., Wang, B., Zeyen, N., and Wilson, S. A. (2021). Evaluating feedstocks for carbon dioxide removal by enhanced rock weathering and CO_2 mineralization. *Applied Geochemistry* 129, 104955. doi: 10.1016/j.apgeochem.2021.104955

Paulo, C., Power, I. M., Zeyen, N., Wang, B., and Wilson, S. A. (2023). Geochemical modeling of CO_2 sequestration in ultramafic mine wastes from Australia, Canada, and South Africa: Implications for carbon accounting and monitoring. *Applied Geochemistry* 152, 105630. doi: 10.1016/j.apgeochem.2023.105630

Paustian, K., Andrén, O., Janzen, H. H., Lal, R., Smith, P., Tian, G., et al. (1997). Agricultural soils as a sink to mitigate CO_2 emissions. *Soil Use Manag* 13, 230–244. doi: https://doi.org/10.1111/j.1475-2743.1997.tb00594.x

Phelan, J., Belyazid, S., Kurz, D., Guthrie, S., Cajka, J., Sverdrup, H., et al. (2014). Estimation of soil base cation weathering rates with the PROFILE model to determine critical loads of acidity for forested ecosystems in Pennsylvania, USA: Pilot application of a potential national methodology. *Water Air Soil Pollut* 225. doi: 10.1007/s11270-014-2109-4

Pogge von Strandmann, P. A. E., Tooley, C., Mulders, J. J. P. A., and Renforth, P. (2022). The dissolution of olivine added to soil at 4°C: Implications for enhanced weathering in cold regions. *Frontiers in Climate* 4, 827698. doi: 10.3389/fclim.2022.827698

Pokrovsky, O. S., and Schott, J. (2000). Kinetics and mechanism of forsterite dissolution at 25°C and pH from 1 to 12. *Geochemica et Cosmochimica Acta* 64, 3313–3325.

Power, I. M., Dipple, G. M., Bradshaw, P. M. D., and Harrison, A. L. (2020). Prospects for CO_2 mineralization and enhanced weathering of ultramafic mine tailings from the Baptiste nickel deposit in British Columbia, Canada. *International Journal of Greenhouse Gas Control* 94. doi: 10.1016/j.ijggc.2019.102895

Power, I. M., Harrison, A. L., Dipple, G. M., Wilson, S. A., Kelemen, P. B., Hitch, M., et al. (2013a). Carbon mineralization: From natural analogues to engineered systems. *Rev Mineral Geochem* 77, 305–360. doi: 10.2138/rmg.2013.77.9

Power, I. M., Paulo, C., and Rausis, K. (2024). The mining industry's role in enhanced weathering and mineralization for CO_2 removal. *Environ Sci Technol* 58, 43–53. doi: 10.1021/acs.est.3c05081

Power, I. M., Wilson, S. A., and Dipple, G. M. (2013b). Serpentinite carbonation for CO_2 sequestration. *Elements* 9, 115–121. doi: 10.2113/gselements.9.2.115

Pronost, J., Beaudoin, G., Tremblay, J., Larachi, F., Duchesne, J., Hébert, R., et al. (2011). Carbon sequestration kinetic and storage capacity of ultramafic mining waste. *Environ Sci Technol* 45, 9413–9420. doi: 10.1021/es203063a

Rausis, K., Ćwik, A., and Casanova, I. (2020). Phase evolution during accelerated CO_2 mineralization of brucite under concentrated CO_2 and simulated flue gas conditions. *Journal of CO_2 Utilization* 37, 122–133. doi: 10.1016/j.jcou.2019.12.007

Renforth, P., Pogge von Strandmann, P. A. E., and Henderson, G. M. (2015). The dissolution of olivine added to soil: Implications for enhanced weathering. *Applied Geochemistry* 61, 109–118. doi: 10.1016/j.apgeochem.2015.05.016

Schuiling, R. D., and Krijgsman, P. (2006). Enhanced weathering: An effective and cheap tool to sequester CO_2. *Clim Change* 74, 349–354. doi: 10.1007/s10584-005-3485-y

Smith, P., Soussana, J. F., Angers, D., Schipper, L., Chenu, C., Rasse, D. P., et al. (2020). How to measure, report and verify soil carbon change to realize the potential of soil carbon sequestration for atmospheric greenhouse gas removal. *Glob Chang Biol* 26, 219–241. doi: 10.1111/gcb.14815

Strefler, J., Amann, T., Bauer, N., Kriegler, E., and Hartmann, J. (2018). Potential and costs of carbon dioxide removal by enhanced weathering of rocks. *Environmental Research Letters* 13, 034010. doi: 10.1088/1748-9326/aaa9c4

Stubbs, A. R., Paulo, C., Power, I. M., Wang, B., Zeyen, N., and Wilson, S. A. (2022). Direct measurement of CO_2 drawdown in mine wastes and rock powders: Implications for enhanced rock weathering. *International Journal of Greenhouse Gas Control* 113, 103554. doi: 10.1016/j.ijggc.2021.103554

Sverdrup, H. U., Oelkers, E., Erlandsson Lampa, M., Belyazid, S., Kurz, D., and Akselsson, C. (2019). Reviews and synthesis: Weathering of silicate minerals in soils and watersheds: Parameterization of the weathering kinetics module in the PROFILE and ForSAFE models. *Biogeosciences Discussions*, 1–58. doi: 10.5194/bg-2019-38

Sverdrup, H., and Warfvinge, P. (1993). Calculating field weathering rates using a mechanistic geochemical model PROFILE. *Applied Geochemistry* 8, 273–283.

Taylor, L. L., Beerling, D. J., Quegan, S., and Banwart, S. A. (2017). Simulating carbon capture by enhanced weathering with croplands: an overview of key processes highlighting areas of future model development. *Biol Lett* 13, 20160868. doi: 10.1098/rsbl.2016.0868

te Pas, E. E. E. M., Hagens, M., and Comans, R. N. J. (2023). Assessment of the enhanced weathering potential of different silicate minerals to improve soil quality and sequester CO_2. *Frontiers in Climate* 4, 954064. doi: 10.3389/fclim.2022.954064

Vanderkloot, E., and Ryan, P. (2023). Quantifying the effect of grain size on weathering of basaltic powders: Implications for negative emission technologies via soil carbon sequestration. *Applied Geochemistry* 155, 105728. doi: 10.1016/j.apgeochem.2023.105728

Vienne, A., Poblador, S., Portillo-Estrada, M., Hartmann, J., Ijiehon, S., Wade, P., et al. (2022). Enhanced weathering using basalt rock powder: Carbon sequestration, co-benefits and risks in a mesocosm study with solanum tuberosum. *Frontiers in Climate* 4, 869456. doi: 10.3389/fclim.2022.869456

Voormeij, D. A., and Simandl, G. J. (2004). Geological, ocean, and mineral CO_2 sequestration options: A Technical Review. *Geoscience Canada* 31.

White, A. F., Blum, A. E., Bullen, T. D., Vivit, D. V, Schulz, M., and Fitzpatrick, J. (1999). The effect of temperature on experimental and natural chemical weathering rates of granitoid rocks.

Wilson, S. A., Dipple, G. M., Power, I. M., Barker, S. L. L., Fallon, S. J., and Southam, G. (2011). Subarctic weathering of mineral wastes provides a sink for atmospheric CO_2. *Environ Sci Technol* 45, 7727–7736. doi: 10.1021/es202112y

Wilson, S. A., Harrison, A. L., Dipple, G. M., Power, I. M., Barker, S. L. L., Ulrich Mayer, K., et al. (2014). Offsetting of CO_2 emissions by air capture in mine tailings at the Mount Keith Nickel Mine, Western Australia: Rates, controls and prospects for carbon neutral mining. *International Journal of Greenhouse Gas Control* 25, 121–140. doi: 10.1016/j.ijggc.2014.04.002

Zeyen, N., Wang, B., Wilson, S. A., Paulo, C., Stubbs, A. R., Power, I. M., et al. (2022). Cation exchange in smectites as a new approach to mineral carbonation. *Frontiers in Climate* 4, 913632. doi: 10.3389/fclim.2022.913632

Chapter 2
Enhanced weathering of kimberlite mine residues in field experiment: Implications for carbon accounting and verification

2.1 Introduction

The failure to achieve greenhouse gas (GHG) reduction targets necessitates the adoption of negative emissions technologies (NETs) that remove carbon dioxide (CO_2) from the atmosphere (UNFCCC, 2015; Hoegh-Guldberg et al., 2018). Concurrently, the metals and mining industry generates ~100 Gt/yr of solid waste and contributes 4–7% to global GHG emissions (Wani et al., 2022; Weiler et al., 2024). While the industry aims to reduce GHG emissions through electrification, it can also benefit from implementing NETs that have robust carbon accounting measures to fortify their efforts in achieving decarbonized operations (Power et al., 2024).

Carbon mineralization of processed kimberlite from diamond mining has been previously estimated through isotopic carbon accounting in precipitated carbonates (Wilson et al., 2014), and laboratory experimentation adjusting environmental controls of carbonation rate (Paulo et al., 2021; Stubbs et al., 2022). Despite mineralogical suitability (e.g., 10.8–90 wt.% lizardite [$Mg_3Si_2O_5(OH)_4$]), the rate of fine processed kimberlite carbonation in impoundments is slow (e.g., Venetia Diamond Mine, South Africa: 0.59 g CO_2/kg/yr, Diavik Diamond Mine, Canada: 0.13–0.18 g CO_2/kg/yr; Paulo et al., 2023) relative to the pace at which industrial CO_2 emissions are produced. Further, tailings impoundments are designed to prevent reactions facilitated by atmospheric CO_2; however, there have been recommendations to modify tailings management practices to improve CO_2 ingress (e.g., reduce water content in tailing ponds; Power et al., 2013;

Wilson et al., 2014). Similar adjustments to mine waste management could include spreading wastes over mine sites or adjacent land to optimize atmospheric exposure.

Enhanced rock weathering (ERW) involves spreading silicate rocks to accelerate the weathering and dissolution of target minerals [e.g., lizardite and forsterite (Mg_2SiO_4)], an approach that is in stark contrast to mine waste storage. This NET has potential for a global impact on CO_2 mitigation given the abundance of suitable rock formations (Moosdorf et al., 2014; Renforth et al., 2015; Goll et al., 2021; Paulo et al., 2021; Stubbs et al., 2022). Recent ERW field trials have primarily applied crushed basalt to agricultural fields (Larkin et al., 2022; Guo et al., 2023; Kantola et al., 2023); however, monitoring, reporting, and verification (MRV) of carbon storage derived from the weathering of other rock types is needed to progress ERW. Environmental variabilities (e.g., climatic variance and soil types) prevent the development of a standardized method, with site-specific carbon accounting requiring a tailored method for each feedstock and environment (Almaraz et al., 2022). Still, the benefits of spreading Si-bearing rock powders encourages research and implementation of ERW as co-benefits may include increased nutrient availability, vegetation promotion, and potentially aid mine closure remediation (Schuiling and Krijgsman, 2006; Moosdorf et al., 2014; Gunnarsen et al., 2023).

This study aimed to advance ERW implementation of mine wastes by defining a measurable approach for CO_2 removal quantification and introduce a significant contribution to the circular economy by repurposing an industrial waste. The goals of this study were to (1) quantify CO_2 removal by kimberlite residues amended to soil field plots, (2) evaluate several approaches for MRV, and (3) assess the suitability of kimberlite as a soil amendment through considerations of released elements of concern (e.g., Ni and Cr) and elements of interest (e.g., P and K). To achieve these goals,

kimberlite residues from the Gahcho Kué Diamond Mine (Northwest Territories, Canada) were characterized to determine geochemical, mineralogical, and physical properties in the context of ERW applications, followed by batch leaching experiments for an initial assessment of reactivity and element release. Two square-metre soil plots amended with varying dosages of kimberlite residues and a soil control were monitored for 3 years as an ERW field experiment in Peterborough, Ontario, Canada. Best practices for monitoring carbon removal in climates similar to this field site consisted of determining loadings of cations and hydrochemistry of soil waters via a water balance approach derived from hydrological parameters.

2.2 Site description

Field experiments were conducted from June 2021 to October 2023 on the Trent University Symons Campus in Peterborough, Ontario, Canada (44°N 21′ 0″, 78°W 17′ 24″) using fine processed kimberlite from the Gahcho Kué Diamond Mine applied to local soil plots. The site has an elevation of ~230 MAMSL, is relatively flat (2º), and thus has a low potential for runoff generation and accumulation. Peterborough has a humid continental climate with the average warmest temperature in July (26.8°C) and coldest average temperature in January (-13.0ºC), and an average annual precipitation of 882 mm, 16% of which falls as snow (Environment Canada, 2021). Weather data, including rainfall, air temperature, and relative humidity were recorded quarter-hourly at the Trent Climate Station, 1 km south of the study site (Environment Canada, 2021).

Vegetation cover consisted primarily of a variety of grasses and forbs including *Trifolium repens* (White clover), *Taraxacum officinale* (Dandelion), and *Cirsium arvense* (Canada Thistle). Grass species, *Andropogon gerardii* (Big Bluestem), *Achillea*

millefolium (Common yarrow), and *Anthoxanthum hirtum* (Sweetgrass) were prevalent with some *Daucus carota* (Queen Anne's lace) found in each experimental plot.

Soils at the study site are classified as an Orthic Melanic Brunisol, characterized by high organic content ($LOI_{550°}$: 4.6%–15.1%), calcareous parent material, and thus a neutral pH (7–8; Smith et al., 2011). The mineralogical component of these sandy loam soils is dominated by quartz ([SiO_2]; 30.7 wt.%), albite ([$NaAlSi_3O_8$]; 23.4 wt.%), microcline ([$KAlSi_3O_8$]; 23.4 wt.%), and calcite ([$CaCO_3$]; 16.1 wt.%), with lesser abundances of ferro-pargasite ([$NaCa_2(Fe^{2+}{}_4Al)(Si_6Al_2)O_{22}(OH)_2$]; 6.5 wt.%; Table 2.2). Although this site has a history of agriculture (pre-20th century; Jones et al., 2002), it is currently undisturbed buffer land with the nearest agricultural activity ~500 m east.

2.3 Acquisition of kimberlite residues

As part of De Beers' Project CarbonVault, approximately 300 kg of fine processed kimberlite (FPK) were transported as a slurry from the Gahcho Kué Diamond Mine to Trent University in 2020. The mine is an open pit operation located in the Northwest Territories, Canada (63°N 26′ 29.5″, 109°W 10′ 36″) that extracts diamond-bearing kimberlite from three main pipes emplaced into the Archaeon Slave Craton granitoids (Hetman et al., 2004). In addition to extensive characterization, these residues were used for the batch leaches with CO_2 and ERW field experiment.

In addition, kimberlite residues were obtained from the Jwaneng and Orapa (n=12) diamond mines in Botswana, and Voorspoed (n=3) and Venetia (n=34) Diamond Mine in South Africa. These residues were only analyzed by X-ray fluorescence spectroscopy to compare their geochemical composition to the Gahcho Kué residues.

2.4 Materials characterization

The Gahcho Kué (GK) kimberlite residues and local field soil were analyzed for their mineralogical and geochemical composition, and physically characterized. Quantitative mineralogical data were obtained by Rietveld refinement of powder X-ray diffraction (XRD) data analyzed by a Bruker D8 Advance and Bruker D2 Phaser θ-θ X-ray diffractometer. Geochemical data were obtained by X-ray fluorescence (XRF) spectroscopy and inductively coupled plasma optical emission spectroscopy (ICP-OES) after samples were prepared using a 4-acid digestion. Additional chemical characterization included initial total inorganic carbon (TIC) content of the residues measured via carbon coulometry, and total cation exchange capacity (CEC) measured by ICP-OES analysis of leachate extractions. Specific surface areas (SSA) were determined using the Brunauer-Emmett-Teller (BET) method of N_2 adsorption (Brunauer et al., 1938), and particle size distribution (PSD) were determined using a Horiba LA-950V2 laser scattering particle size distribution analyzer. Detailed analytical methods with detection limits and analytical error are provided in Appendix A.

Three hammer core samples (98 cm^3) were collected at the ERW field experiment site with each soil profile divided into the surface (0–5 cm), middle (5–15 cm), and bottom (15–30 cm) fractions (Table 2.1). Samples were dried under ambient conditions, disaggregated, and sieved (2 mm) before characterization of geochemical and physical properties. The bulk density of the soil weatherable fraction was determined by water displacement of an undisturbed soil core, with the >2 mm mass fraction subtracted from the total soil mass. Bulk surface samples were used for the batch leaching experiment.

Table 2.1. Field site soil properties at the surface, middle, and bottom of the profile (n=3).

Soil properties	**Surface (0–5 cm)**	**Middle (5–15 cm)**	**Bottom (15–30 cm)**
pH_{H2O}	7.9	8.3	8.4
Bulk density (g/cm^3)	1.2 ± 0.1	1.3 ± 0.1	1.0 ± 0.1
SSA (m^2/g)	3.4	2.2	1.6
$LOI_{550°}$ (%)	13.1 ± 2.0	9.3 ± 2.8	7.9 ± 3.3
Total carbon (%)	5.3 ± 0.9	4.5 ± 0.2	4.6 ± 0.7
TIC (%)	1.9 ± 0.4	2.1 ± 0.1	1.3 ± 0.2
D80 (µm)	268 ± 45	166 ± 105	339 ± 46
Total CEC (cmol/kg)	15.3	10.9	8.8
Texture	sandy loam	silt loam	sandy loam

2.5 Experimental methods

2.5.1 Batch leaches with CO_2

Kimberlite residues and soils were mixed for a total mass of 5.0 g, with varying kimberlite concentrations (0, 0.5, 1, 5, 10, 25, 50, and 100 wt.%), and are henceforth referred to as Soil100, 0.5GK, 1GK, 5GK, 10GK, 25GK, 50GK, and 100GK. Mixtures (n=1), in 2.5 g aliquots, were micronized for 7 min in anhydrous ethanol using a McCrone Micronizing Mill prior to analysis for geochemical compositions.

Differentiating the easily extractable cations from the field soil and added GK residues was achieved using the CO_2 batch leaches. The batch leach method was modified from Paulo et al. (2021) and used 250.0 mg aliquots of soil-kimberlite mixtures (adding 15 wt.% and 75 wt.% kimberlite mixtures denoted 15GK and 75GK) added to 100 mL of deionized water (18.2 MΩ·cm). The experiment consisted of triplicate polyethylene flasks for control soil (0GK) and kimberlite residues (100GK), one of deionized water only, and one flask each for the remaining mixtures for a total of 15 flasks. A ThermoScientific™ CO_2 Resistant Shaker table set to 150 rpm was used to mix the

suspensions inside a ThermoScientific™ HERAcell VIOS 160i CO_2 incubator (35°C, 10% CO_2, 21.9% O_2) at nearly 100% relative humidity. Uncapped flasks were mixed inside the chamber for 2 weeks. Upon completion of the batch leach, pH was measured, and leachates were filtered (0.22 μm) into 50 mL plastic centrifuge tubes and acidified (2% v/v ultrapure HNO_3, Aristar ®, UK). Water samples were stored at 4ºC prior to cation analysis by inductively coupled plasma mass spectrometry (ICP-MS).

2.5.2 ERW field experiments

2.5.2.1 Design and setup

Small-scale field plots were used to comprehensively monitor the weathering of Gahcho Kué residues applied to soil and determine the CDR achieved over three monitoring periods – essentially 3 yr. Three circular plots (1 m^2) were created in June 2021, orientated so that ~2 m of space was achieved between each plot (Fig. 2.1A) within a fenced enclosure (Fig. 2.1B). Vegetation was removed from the plots, tilling the soil lightly with a garden cultivator to create a loose soil layer (~2 cm) to ease amendment mixing. In each plot, one SoilMoisture 1900L 18-B02M2 Near Surface porewater sampler (46 cm length), and TEROS 12 soil moisture probe (METER Group Inc.) was installed at 15 and 30 cm depths (Fig. 2.2). The probes measured soil volumetric water content (m^3/m^3) and temperature (°C) every 15 min, recording values on an on-site ZL6 data logger (METER Group Inc.). A soil gas lance (BGLD-300; METER Group Inc.) was used to sample soil pore gas for CO_2 concentration measurements at a depth of 20 cm (Fig. 2.2). All holes created during instrument installation were backfilled with a ~1:1 slurry of the excavated soil and deionized water.

One plot was used as a control to assess natural background weathering (Fig. 2.1C). The other two plots were amended with 10 and 20 kg of Gahcho Kué fine kimberlite residues in June 2021; however, in June 2022, an additional 30 kg of kimberlite residues was added to the 10 kg plot to assess a repeated application of kimberlite residues (Fig. 2.1D). The amended plots are denoted K10+30 and K20, respectively. The kimberlite residues were applied by hand, mixing into the loosened soil. A polyvinyl chloride (PVC) collar (ø = 20 cm) was inserted into each plot after amendment at a depth of 14 cm, leaving a 2 cm offset for CO_2 flux measurements; however, over time this offset increased to ~5 cm from natural compaction of the soil and was accounted for during CO_2 flux measurements.

The equipment was first removed in October 2021 for the winter, and the plots left unmonitored for 6 months between November 2021 and May 2022 upon which equipment was reinstalled, and monitoring continued uninterrupted for the next 16 months (to end of September 2023). The experiment was divided into three monitoring periods: the first (June 2021–October 2021, inclusive), second (May 2022–December 2022, inclusive), and third monitoring period (January 2023–September 2023, inclusive), concluding after ~3 yr.

Figure 2.1. Orientation of the three square-metre plots, with two different application rates of kimberlite residues (K10+30: 10+30 kg/m^2; K20: 20 kg/m^2) and a control (A). Outdoor experimental area at Trent University (B). The control plot showing one of two water samplers and the CO_2 analyzer measuring CO_2 surface fluxes (C). Fine processed kimberlite amendment on the K10+30 plot after reamendment (D).

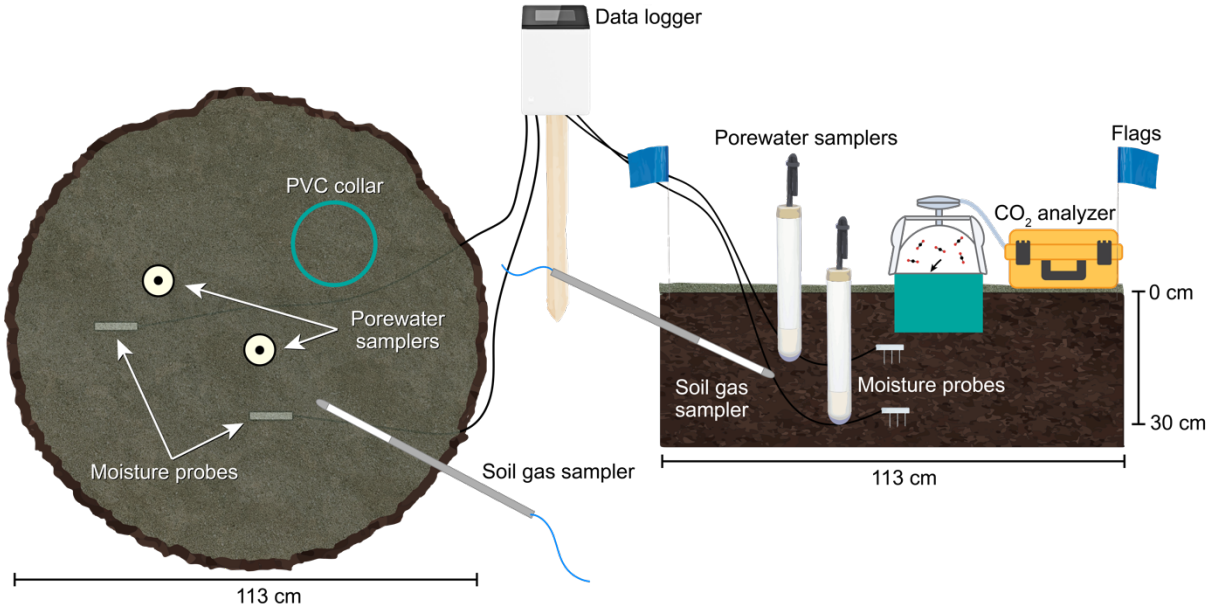

Figure 2.2. Experimental setup for field plots that were equipped with porewater samplers at 15 and 30 cm depths and a soil gas sampler at 20 cm depth. TEROS 12 moisture probes were installed at 15 and 30 cm depths, recording data onto a ZL6 data logger located outside of the plot. A 20 cm diameter PVC collar with a 2 cm offset was used for CO_2 flux measurements using a LI-COR survey chamber and LI-8100A CO_2 analyzer.

2.5.2.2 CO_2 fluxes and pore gas measurements

CO_2 fluxes were measured daily for two weeks immediately following kimberlite amendments using an LI-8100 soil CO_2 flux system equipped with a survey chamber (LI-COR, Lincoln, Nebraska, USA), and once weekly throughout each monitoring period. This instrument, which was positioned on the PVC collar of an experimental plot, monitored the diffusion rate of CO_2 ($\mu mol/m^2/s$) over a programmed period of 3 min. The control plot was used to compare natural fluxes to the amended soil fluxes, where negative values indicate CO_2 drawdown and positive indicate CO_2 efflux. The instrument was programmed to pre-purge the chamber for 1 min prior to measurement and post-purge for 2 min between plot measurements. Measurements were completed in triplicate. The offset, indicating the distance between the top of the PVC collar and the soil surface,

was adjusted throughout the experiment increasing from 2 cm over time due to natural compaction of the soils. The CO_2 fluxes were determined using the program SoilFluxPro 4.0.1, which is for viewing and processing data from the LI-8100 system. Fluxes were calculated based on the change in CO_2 concentration from typically 30–179 s of the 180 s measurement, fitted to an exponential curve with the instantaneous rates extrapolated to 1 yr. In the second (May 2022–December 2022) and third (January 2023–September 2023) monitoring period, the CO_2 analyzer was re-programmed to measure the CO_2 diffusion rate over 2 min with a pre- and post-purge of 10 s. Shortening the analysis time provided a more instantaneous rate of the soil CO_2 fluxes, less disturbance to the surface with quicker pre-purges, and was acceptable later in the experiment when fluxes maintained positive values within the control range. Fluxes were thereafter calculated from the CO_2 concentration change over a ~120 s interval.

Soil pore gas was sampled at 20 cm depths using a 60 mL syringe to draw pore gas out of the soil gas lance and plunged through a Vaisala CARBOCAP® Carbon Dioxide Probe GMP251 (0–20% CO_2) that measures the CO_2 concentrations that are displayed using an MI70 indicator. Values were recorded bi-monthly with a ±0.2% accuracy in each reading in a 0–8% CO_2 range.

2.5.2.3 Water sampling

The plots were initially wetted with 20 L of deionized water in 5 L increments over 2 h to test water sampler installation and to allow instruments to settle into the surrounding soil. A vacuum hand pump with pressure gauge was used to achieve a vacuum of at least 70 kPa in each of the surface porewater samplers, allowing porewater to be drawn into the porous ceramic cup at the base of the sampler. Samplers were

pumped weekly, or following a rain event, for opportunistic sample collection; however, sample collection was limited during dry periods such as August 2021. From December 2022 to March 2023, which was a particularly mild winter, water samples were collected during periods of snow melt.

The pH of the water samples was measured immediately after sampling using a ThermoScientific Orion 4-Star pH/ISE meter that was calibrated daily. Samples were filtered (0.22 μm) into 50 mL plastic centrifuge tubes with aliquots of 30 mL being acidified (2% v/v ultrapure HNO_3, Aristar ®, UK) for major and trace element analysis. All non-acidified samples were analyzed for alkalinity (methods in Appendix A) and dissolved inorganic carbon (DIC), while only select samples were analyzed for major anions ($n \geq 4$ per monitoring period) and stable carbon and oxygen isotopes ($n=2$). Samples were stored at 4°C prior to analysis. One way ANOVA ($p < 0.05$) was used to compare the three plots in mean DIC, alkalinity, and pH at 15 and 30 cm, coupled with Tukey's post hoc test for pairwise comparisons.

2.5.2.4 Soil sampling

To determine pedogenic carbonate precipitation in the experiment plots, triplicate soil cores were sampled using a soil core sampler down to ~25 cm in each plot in December 2022 and November 2023. Soil cores were divided into 2–5 cm increments upon collection, dried in a fume hood, and homogenized prior to storage. Due to the limited space in the square metre plots, and magnitude of material removed while disturbing the plots, regular water sample collection was preferred over repeated core

collection. Dried soils at each depth were micronized (~1 g) and ~100 mg aliquots were analyzed for TIC.

2.5.3 Analytical methods

2.5.3.1 Dissolved inorganic carbon analysis

DIC was measured using a Model CM5017 Coulometer from UIC Inc. at Trent University. The coulometer was calibrated prior to each use, blanks and 250 and 500 mg/L standards of $NaHCO_3$. Detection limits of the instrument range from 0.0001–100% C with a precision of 0.01 mg C/L. Samples were pipetted (1.0 mL) into 25 mL glass flasks, acidified with 2N H_2SO_4 (10 mL), and mixed with an 8 mm stir bar at 50°C with a carrier gas rate of 100 mL/min through the acidification module. The pre-scrubber used potassium hydroxide (45%) to remove any CO_2 present in the carrier gas, while the post-scrubber removed H_2S, SO_x, and halogens using silver nitrate (3%). This method for the coulometer facilitates CO_2 reactions with mono-ethanolamine to form a titratable acid (hydroxyethylcarbamic acid) and electrochemically generates OH^- in the platinum electrode, neutralizing the solution until it returns to its original colour. The colour change is measured as a percent transmittance (%T) by a photodetector, which is proportional to the concentration of hydroxyethylcarbamic acid formed and, therefore, equivalent to the amount of inorganic carbon injected into the cell sourced from the sample. Samples were analyzed in duplicate, analyzing for a third time if values were not within ±5 mg C/L.

2.5.3.2 Cation and anion analyses

Major and trace elements were analyzed at either SGS Canada Inc. in Lakefield, Ontario or in the Water Quality Centre at Trent University. SGS Canada Inc. used an Agilent 8000 Triple Quadrupole inductively coupled plasma-mass spectrometer (ICP-MS) which has detection limits for major cations Si, Ca, Na, K, P, and Mg of 0.02, 0.01, 0.01, 0.009, 0.003, and 0.001 mg/L, respectively, and trace elements Ni and Cr of 0.1 and 0.08 µg/L, respectively.

At Trent University, an Agilent 8800 Triple Quadrupole ICP-MS was used and operated in MS/MS on-mass mode using He or H_2 (dependent on analyte) as the reaction cell collision gases. Sample introduction used a MicroMist nebulizer (nominal uptake rate 400 µL/min) coupled with a Scott double pass spray chamber. Calibration standards were prepared for the µg/L and mg/L range, diluting 100 mg/L multi-element standard and 1000 mg/L major cation stock solutions for each range, respectively. Accuracy and precision were monitored by analyzing quality check standards (1.25 and 2.50 mg/L) every 15 samples, with instrument bias continuously corrected by an internal standard of Ge, In, Sc, Tb, Y, and Li-6 at a final concentration of 200 µg/L. Phosphorus concentrations were negligible in differences between the plots for the 2021 and 2022 monitoring period and was therefore not analyzed for the 2023 period. Aliquots of 15 mL were analyzed for major anions (Br^-, Cl^-, SO_4^{2-}, NO_3^-, NO_2^-) at SGS Canada Inc. (Lakefield) by ion chromatography (IC) using a Thermo Scientific™ Dionex™ ICS-1100 with detection limits of 0.3, 0.2, 0.2, 0.06, and 0.03 mg/L, respectively.

2.5.3.3 Total inorganic carbon analysis

TIC was determined using a UIC CM5017 Coulometer at Trent University, the same instrument used for DIC analysis. Calibration of the instrument was conducted before each use, using blanks and $CaCO_3$ standards (Alfa Aesar; 99.95–100.05% purity). Detection limits of the instrument range from 0.0001-100% C with a precision of 0.01 µg C. Micronized samples (250 mg) were digested in 2N H_2SO_4 (10 mL) and mixed with an 8 mm stir bar at 50°C, with a carrier gas rate of 100 mL/min through the acidification module. The pre-scrubber used potassium hydroxide (45%) to remove any CO_2 present in the carrier gas, while the post-scrubber removed H_2S, SO_x, and halogens using silver nitrate (3%). Identical to the DIC method, the colorimetric cell contained a mixture of mono-ethanolamine and a colour indicator, hosting a platinum electrode and silver anode. A generated titratable acid changes the colour of the cell solution (%T) corresponding with the amount of inorganic carbon injected into the cell. Samples were analyzed in triplicate.

2.5.3.4 Stable C and O isotopes

All stable carbon and oxygen isotopic compositions were analyzed at the Ján Veizer Stable Isotope Laboratory (Ottawa, Ontario, Canada). Filtered (<0.22 µm) porewater samples were analyzed for $\delta^{13}C$ using an OI Analytical Aurora 1030 Wet Oxidation TOC analyzer interfaced to a Thermo Finnigan DeltaPlus XP IRMS via a Conflo VI (± 0.3‰). $\delta^{18}O$ values were measured using a Picarro L2130-*i* cavity ring-down spectrometer coupled with a A0211 Vaporizer (± 0.1‰) and A0214 Micro-Combustion Module.

Stable carbon and oxygen isotopes of carbonate minerals in the bulk kimberlite residues and control soils were measured in triplicate. Isotope compositions were analyzed using a Thermo Finnigan DeltaPlus XP continuous-flow isotope-ratio mass spectrometer and Gas Bench II (± 0.1‰). Additionally, triplicate control soils were washed with 10% HCl and dried and rinsed with deionized water via vacuum filtering to measure the ^{13}C and ^{18}O compositions of the organics. These samples were analyzed using a DeltaPlus Advantage isotope ratio mass spectrometer coupled with a ConFlo IV interface (± 0.2‰) and a Thermo DeltaPlus XP continuous-flow isotope-ratio mass spectrometer coupled with a ThermoScientific thermal conversion elemental analyzer (± 0.3‰), respectively.

Stable carbon and oxygen isotopic compositions of soil pore gas CO_2 were determined using a Thermo-Fisher Delta V isotope ratio mass spectrometer coupled with a ConFlo IV interface (± 0.2‰) and GC-Isolink system equipped with combustion and pyrolysis furnaces. Using a syringe and needle, soil pore gases were stored in 125 mL serum vials (butyl stopper and crimped) that were flushed with N_2 gas prior to sample injection. Vials were pressurized by injecting a 60 mL syringe of sample gas. Caps were wrapped in parafilm to prevent mixing with atmospheric CO_2.

2.6 Results

2.6.1 Material characterization

The Gahcho Kué residues had a D80 particle size of 175 µm which was within the same order of magnitude as the grain sizes observed in the soils used in the batch leaches and field experiment (Table 2.1; Table 2.2). The resulting surface area for the residues (20.6 m^2/g; Table 2.2) was greater than that of the soils (~3.4 m^2/g; Table 2.1), whereas

CEC was greater in the soils. Essential soil nutrients, P_2O_5 and K_2O, were near identical in the residues and field soils with only a slight enrichment of K_2O in the residues (Table 2.3). On the other hand, the residues were significantly enriched in metals of concern, Ni (1151 mg/L) and Cr (704 mg/L; Table 2.2), while these metals in the field soil were present at lower concentrations of 16 and 34 mg/L, respectively (Table 2.4).

The kimberlite residues were mainly composed of SiO_2 (42.9 wt.%) and MgO (27.1 wt.%), with lower percentages of Fe_2O_3 (7.0 wt.%), Al_2O_3 (5.1 wt.%), CaO (4.0 wt.%), K_2O (2.5 wt.%), and remaining oxide abundances under 1 wt.% (Table 2.3). Major silicate abundances included lizardite (29.4 wt.%), saponite (21.54 wt.%), phlogopite (15.1 wt.%), forsterite (9.2 wt.%), sepiolite (2.4 wt.%), talc (2.2 wt.%), augite (1.1 wt.%), and clinochlore (0.8 wt.%), and calcite (1.9 wt.%); the latter equating to 0.25 ± 0.01% TIC (Table 2.2). Resistant minerals in the residues that were unlikely to contribute to the cation pool for carbon sequestration included microcline (12.1 wt.%), quartz (2.7 wt.%), and albite (1.7 wt.%; Table 2.2).

Table 2.2. Physical, geochemical, and mineralogical characteristics of fine processed kimberlite (FPK) and surface soil (n=3).

	Fine processed kimberlite	Soil
SSA (m^2/g)	20.6	3.4
TIC (%)	0.25 ± 0.01	1.9 ± 0.4
D80 (µm)	175	166–339
Total CEC (cmol/kg)	6.02 ± 0.1	11.7 ± 3.3
Ni (mg/kg)	1151	16
Cr (mg/kg)	704	34
Mineralogy		
Ca- and Mg-bearing silicate phases	Lz (29.4 wt.%), Sap (21.5 wt.%), Phl (15.1 wt.%), Fo (9.2 wt.%), Sep (2.4 wt.%), Tlc (2.2 wt.%), Aug (1.1 wt.%), Clc (0.8 wt.%)	Prg (6.5 wt.%)
Carbonates	Cal (1.9 wt.%)	Cal (16.1 wt.%)
Non-Ca, Mg-bearing phases	Mc (12.1 wt.%), Qtz (2.7 wt.%), Ab (1.7 wt.%)	Qtz (30.7 wt.%), Ab (23.4 wt.%), Mc (23.4 wt.%)

Minerals identified include Lz–lizardite, Sap–saponite, Phl– phlogopite, Fo– forsterite, Sep– sepiolite, Tlc–talc, Aug– augite, Clc– clinochlore, Cal– calcite, Mc– microcline, Qtz– quartz, Ab– albite.

Table 2.3. Geochemical compositions of local soils and fine processed kimberlite (FPK) given as weight percentages.

	Al_2O_3	CaO	Cr_2O_3	Fe_2O_3	K_2O	MgO	Mn_3O_4	Na_2O	P_2O_5	SiO_2	TiO_2	V_2O_5	$LOI_{1000°C}$
Soil	10.7	8.89	<0.01	3.97	2.14	1.44	0.12	1.87	0.27	53.3	0.53	0.01	16.8
FPK	5.04	4.03	0.16	7	2.46	27.1	0.11	0.56	0.27	42.9	0.53	0.02	9.95

2.6.2 Batch leaches with CO_2

The calcareous field soil (16.1 wt.% calcite; Table 2.2) mainly released Ca (~49 g/kg) into solution with all other elements releasing <0.5 g/kg of the initial solids content (Table 2.4). The Ca release substantially declined once 50% of the mixture was composed of GK residues, with the 100GK sample only releasing half (~14 g/kg) of the initial Ca content (~28 g/kg) into solution. Mg release increased with increasing GK residue proportion (~9 g/kg released from the 100GK sample; Table 2.4). Similarly, Si release

was also ~9 g/kg in the 100GK sample (<5% of the total Si in the sample). Although field soils were greater in SiO_2 (53.3 wt.%) due to the abundance of quartz (30.7 wt.%), the amount of Si leached (~0.5 g/kg) was near negligible (Table 2.4).

Table 2.4. Initial element concentrations (g/kg) of solids and element concentrations leached from the initial material (g/kg) into solution after two weeks in a CO_2 incubator. Labels indicate the percentage of Gahcho Kué kimberlite residues (e.g., 25GK = 25% kimberlite, 75% soil).

Proportion of GK residues	Concentration (g/kg)					Leached from solids (g/kg)				
	Ca	Mg	Si	Ni	Cr	Ca	Mg	Si	Ni	Cr
Soil100	61.5	7.6	244	0.02	0.03	48.9	0.5	0.5	0.0005	0.0001
0.5GK	59.5	7.9	245	0.02	0.04	48.8	0.6	0.5	0.0003	0.0001
1GK	60.0	8.7	246	0.03	0.04	47.6	0.6	0.5	0.0005	0.0001
5GK	56.9	14.4	244	0.08	0.07	44.8	1.2	1.0	0.001	0.0001
10GK	57.8	22.2	242	0.1	0.1	48.4	2.0	1.7	0.002	0.0002
25GK	53.0	44.2	232	0.3	0.2	42.8	3.5	3.2	0.006	0.0002
50GK	44.9	82.0	221	0.6	0.4	30.6	6.1	6.0	0.01	0.0001
100GK	27.8	163	197	1.2	0.7	14.3	9.1	8.9	0.04	0.0001
DI Blank (mg/L)						0.02	0.003	0.2	0.003	0.0002

The Ni content in the leachate increased with kimberlite content (100GK: ~0.04 g Ni/kg; Table 2.4), although leachate concentrations of Ni and Cr were three orders of magnitude lower than in the starting material (Fig. 2.3). Leachates from the field soil contained 0.7 and 0.3 mg/L of Ni and Cr, while the residue leachate contained 90 and 0.2 µg/L (Fig. 2.3). However, Cr concentrations are within analysis noise as the blank flask of DI water yielded a Cr concentration of 0.2 µg/L (Table 2.4). The blank also had a Ni concentration of 3 µg/L which is lower than any flask containing >5 wt.% GK residues (Table 2.4).

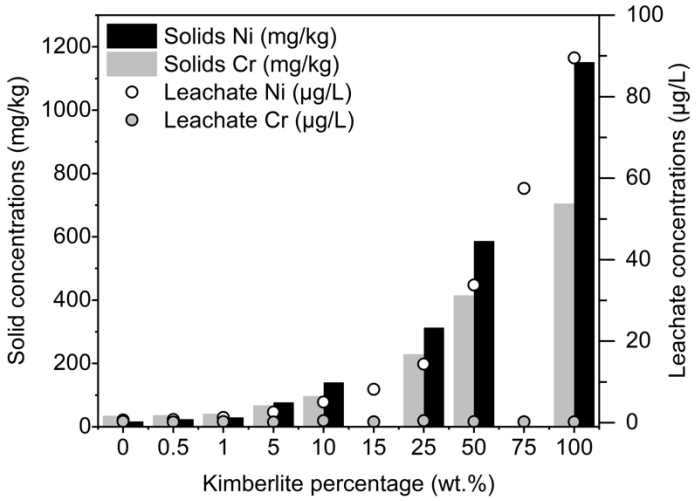

Figure 2.3. Concentrations of Ni and Cr from the flask leachates (µg/L) are represented by circles. The amount of each element in the solid soil-kimberlite mixtures (mg/kg) is represented by bars on the secondary Y-axis.

Principal component analysis (PCA) was performed to identify the element release influenced by the kimberlite residues, which is inferred to isolate weathering activity of the residues and soil. The first two principal components (PCs) of the leachate water chemistry represented 94.7% of the total variance, with PC1 and PC2 accounting for 88% and 6.68%, respectively (Fig. 2.4). The biplot of PCA loadings scores presents a strong negative correlation between PC1 and P, Cu, U, Al, Ti, Ca, V, and Fe, which is mainly distributed in leachates from kimberlite-poor mixtures (<50% GK; Fig. 2.4). Positive correlation between PC1 and Mn, Co, Ni, Sr, Ba, B, Na, Si, Mg, K, and Mo indicates kimberlite residue influence and leachates from kimberlite-rich (≥50% GK; Fig. 2.4) samples. The minimal contribution from PC2 for explaining the total variance indicates a negligible influence on data interpretation.

The PCA biplot represents water chemistry associated with each sample leached and identifies elements linked to the dissolution of minerals within each material. The clustering of elements indicates that the potential for target mineral dissolution influence

on final leachate concentrations were significant in kimberlite-rich samples. This relationship is conspicuous in the biplot, exhibiting a strong positive correlation and close clustering of Mg and Si within PC1 (Fig. 2.4).

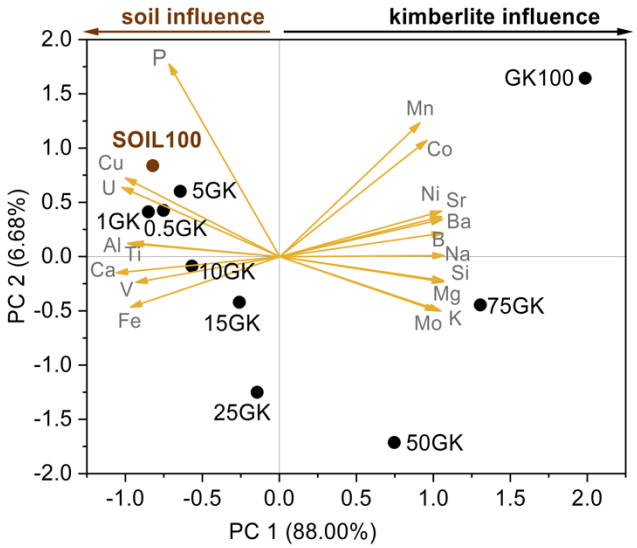

Figure 2.4. Principal component analysis (PCA) biplot showing the multivariance in 10 leached soil-kimberlite mixtures in terms of element variables. Vectors illustrate the direction and overall variable influence strength. PC1 correlates to the influence of soil (negative values) and kimberlite (positive values). Labels indicate the percentage of Gahcho Kué kimberlite residues (e.g., 25GK = 25% kimberlite, 75% soil).

2.6.3 Field experiment

The first (June 2021–November 2021, inclusive), second (May 2022–December 2022, inclusive), and third monitoring period (January 2023–September 2023, inclusive) include data from surface CO_2 fluxes, soil porewater chemistry, and TIC with depth; overall contributing to the calculated CO_2 sequestered by kimberlite residue weathering.

2.6.3.1 CO_2 fluxes and soil pore gas

The average CO_2 flux, derived from instantaneous rates extrapolated to a year, was 6.5, 7.4, and 5.2 kg/m^2/yr in the control, K10, and K20 plots, respectively (Fig. 2.5).

Fluxes were only negative for the K10 and K20 plots on the day of amendment, -4.0 and -5.5 kg/m^2/yr, and became positive and indistinguishable from the control soil after 1 day (0.6–13.6 kg CO_2/m^2/yr; Fig. 2.5). Near negative flux values in the control plot were only recorded at the beginning of the first monitoring period due to artificial wetting of the soils when testing sampling equipment (Fig. 2.5A). The greatest CO_2 efflux values of 13.6, 18.1, and 13.8 kg/m^2/yr in the control, K10, and K20 plots, respectively were observed in August and gradually decreased thereafter until near-net zero CO_2 emissions by the end of the first monitoring period in November 2021 (Fig. 2.5).

During the second monitoring period (May 2022–December 2022, inclusive), there were no negative CO_2 fluxes; however, when 30 kg of residues were added to the K10 plot in June (thereafter referred to as K10+30), fluxes decreased from 8.9 to 1.9 kg CO_2/m^2/yr within 1 h (Fig. 2.5B). The control (3.3–11.6 kg CO_2/m^2/yr with an average of 6.8 kg CO_2/m^2/yr), K10+30 (1.9–13.7 kg CO_2/m^2/yr with an average of 6.3 kg CO_2/m^2/yr), and K20 (2.9–11.1 kg CO_2/m^2/yr with an average of 6.6 kg CO_2/m^2/yr) plots observed the greatest CO_2 efflux in June and July, correlating with soil temperature (Fig. 2.5).

The third monitoring period (January 2023–September 2023, inclusive) similarly observed no negative fluxes with ranges of 1.9–15.5, 1.8–12.9, and 1.4–18.1 kg CO_2/m^2/yr for the control, K10+30, and K20 plots and averages of 9.4, 7.6, and 10.2 kg CO_2/m^2/yr, respectively (Fig. 2.5). Fluxes throughout all monitoring periods exhibited a seasonal oscillation, becoming more positive in warmer months and less positive approaching the winter months when soil temperature began to decline. Soil temperature at 15 cm was monitored to coincide with the soil pore gas measurements from ~20 cm and assist in the ^{13}C and ^{18}O isotopic compositions analyzed in gas samples collected at

this depth. Soil temperature in the control, K10+30, and K20 yielded ranges of 0.4–32.6, 0.8–27.7, and 0.7–37.4ºC over the three monitoring periods with averages of 13.4, 13.2, and 13.0ºC, respectively. Soil pore gas CO_2 concentrations exhibited no significant difference ($p > 0.05$) between the plots and sporadically fluctuated within a few hours yielding ranges of 0.6–1.9%, 0.4–2.1%, and 0.6–1.7% CO_2 over the first two monitoring periods.

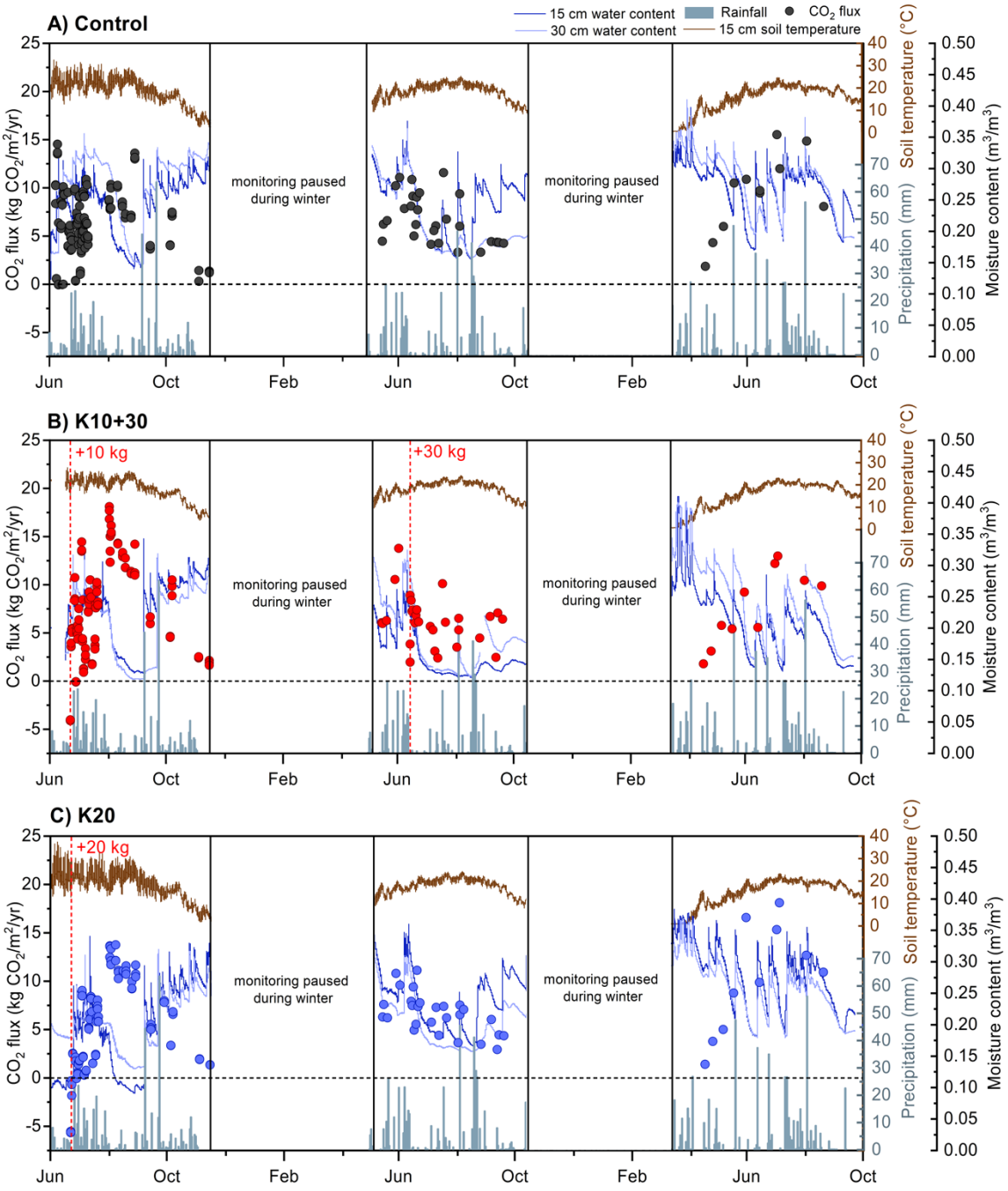

Figure 2.5. CO_2 fluxes (kg $CO_2/m^2/yr$; solid circles) for the control (A), K10+30 (B), and K20 (C) plots at Trent University. Volumetric water contents (m^3/m^3) from moisture probes at 15 and 30 cm depths are plotted as dark blue and light blue lines, respectively, while 15 cm soil temperature (ºC) is represented as a brown line. Daily precipitation (mm) is illustrated as light blue bars and is identical across all plots. Respective kimberlite dosages were added on June 23, 2021 and June 15, 2022 as denoted by the vertical red dashed lines.

2.6.3.2 Soil porewater chemistry

In the amended plots, alkalinity was only statistically different ($p < 0.05$) from shallow control porewater concentrations at 30 cm of the K20 plot in the first monitoring period, and at 15 cm of the K20 in the second monitoring period (Fig. 2.6A). Shallow porewater alkalinity in the K10+30 was significantly increased from all plot porewaters in the third monitoring period (Fig. 2.6A). Concentrations of DIC were only significantly elevated ($p < 0.05$) in the K20 plot compared to the control at 15 cm depths in the first and second monitoring period, whereas the K10+30 concentration only became significantly increased by the second and third monitoring period following reamendment in 2022 (Fig. 2.6B). Throughout the experiment, pH did not vary significantly ($p > 0.05$) between the amended and control plots, fluctuating within one pH unit for all monitoring periods (7.2–8.2; Fig. 2.6C).

A distinct increase in alkalinity and DIC from 15 cm control levels (69.8 ±7 mg C/L and 60.5 ±12 mg C/L) occurred during the first monitoring period with values reaching averages of 80.8 ±10 mg C/L and 72.5 ±15 mg C/L in K10 and 92 ±16 mg C/L and 96.1 ±13 mg C/L in K20, respectively (Fig. 2.6A, B). The K20 plot maintained an average alkalinity measurement of ~90 mg C/L for the next two monitoring periods but declined to a DIC average of 67.7 mg C/L by the third monitoring period (Fig 2.6A, B). Alkalinity values declined in the K10+30 plot returning to 30 cm control signals despite the 30 kg kimberlite addition; however, alkalinity increased significantly by the third monitoring period in shallow porewaters to the highest values recorded in this experiment (averaging 120 ±30 mg C/L Fig. 2.6A). The K10+30 plot experienced a similar significant increase in DIC (93.8 ±23 mg C/L), surpassing the K20 plot (Fig. 2.6B).

Overall, alkalinity correlated with DIC concentrations, showing a maximum variance of ~20%, confirming that DIC was the primary contributor to alkalinity.

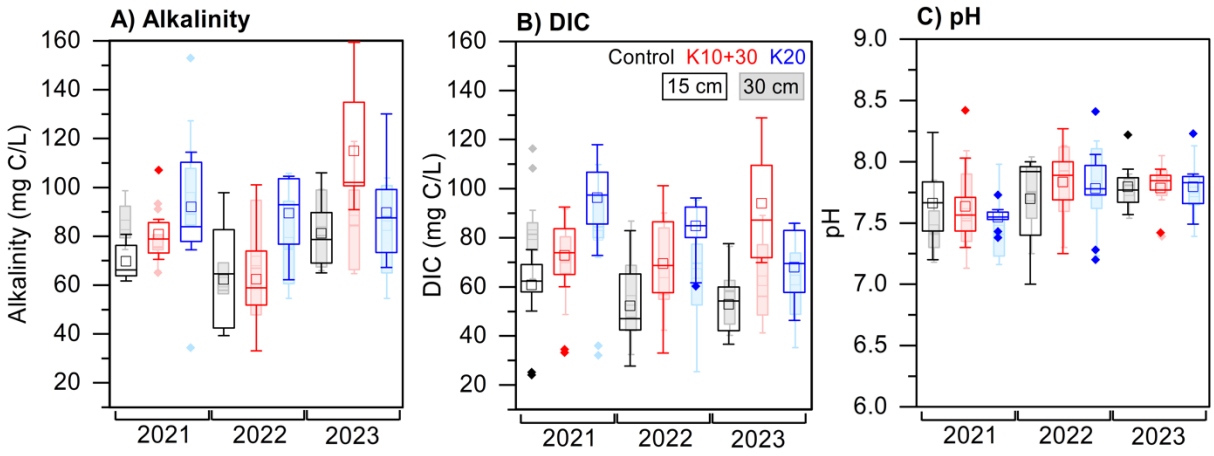

Figure 2.6. Alkalinity (A), DIC (B), and pH (C) at 15 (open box) and 30 cm (shaded) depths in the control, K10+30, and K20 plot over three monitoring periods. The rectangular box represents 25th–75th percentile range, the horizontal line inside the box is the median, the hollow square inside the box the mean, and the vertical lines outside the box are lower (5th percentile) and upper (95th percentile) whiskers. Outliers are shown as solid diamonds.

All porewaters in the control were dominated by Ca (74.3–148 mg/L) with lower concentrations of Mg (1.8–3.9 mg/L), Na (1.2–7.4 mg/L), Si (1.8–6.6 mg/L), K (0.1–5.4 mg/L), Ni (0.5–1.2 µg/L), and Cr (0.03–0.3 µg/L) relative to the amended plots (n = 18–21; Fig. 2.7). The K10 and K20 plot observed their highest Ca concentrations of 230 and 310 mg/L, respectively, in the month following the first amendment, declining to match the control for the remainder of the first monitoring period (Fig. 2.7C). Ca concentrations peaked again in the K10+30 four months after the addition of the 30 kg, reaching 307 mg/L before declining to control Ca levels (Fig. 2.7C).

Kimberlite-influenced elements (e.g., Mg, Si, Na, K, and Ni) derived from PCA of the batch leach data increased above control levels after amendment, reflecting the dissolution of the labile component of the material; however, maximum concentrations of these cations were observed in later monitoring periods (Fig. 2.7). Mg ranged from 3.4–31.5 mg/L and 5.1–16.0 mg/L in the K10+30 and K20 plots, respectively, with the lowest concentrations at the end of the first monitoring period (Fig. 2.7A). Si concentration ranges were 3.6–20.8 mg/L and 5.7–13.2 mg/L in the K10+30 and K20 plots, respectively, where both maximums were experienced at the end of the third monitoring period (Fig. 2.7B). After three monitoring periods, both Mg and Si increased by ~3× and ~1.5× in the K10+30 and K20 plots, respectively. Following the +30 kg, Na increased substantially in the K10+30 plot from initial concentrations of ~7.5 mg/L to ~130 mg/L, roughly 100× control levels (Fig. 2.7D). These Na concentrations declined over the next year to ~40 mg/L, whereas Na concentrations in the K20 plot had declined back to control levels (Fig. 2.7D). Although K concentrations in the K20 plot were immediately increased and remained elevated from the control following amendment (6.0±1.3 mg/L), K did not increase above control signals until the second amendment in the K10+30 plot (thereafter 9.3–22.5 mg/L; Fig. 2.7E). Elements of concern, Ni and Cr, were highest in concentration in later monitoring periods, but remained <12 and <1 µg/L, respectively, in the amended plots (Fig. 2.7F, G).

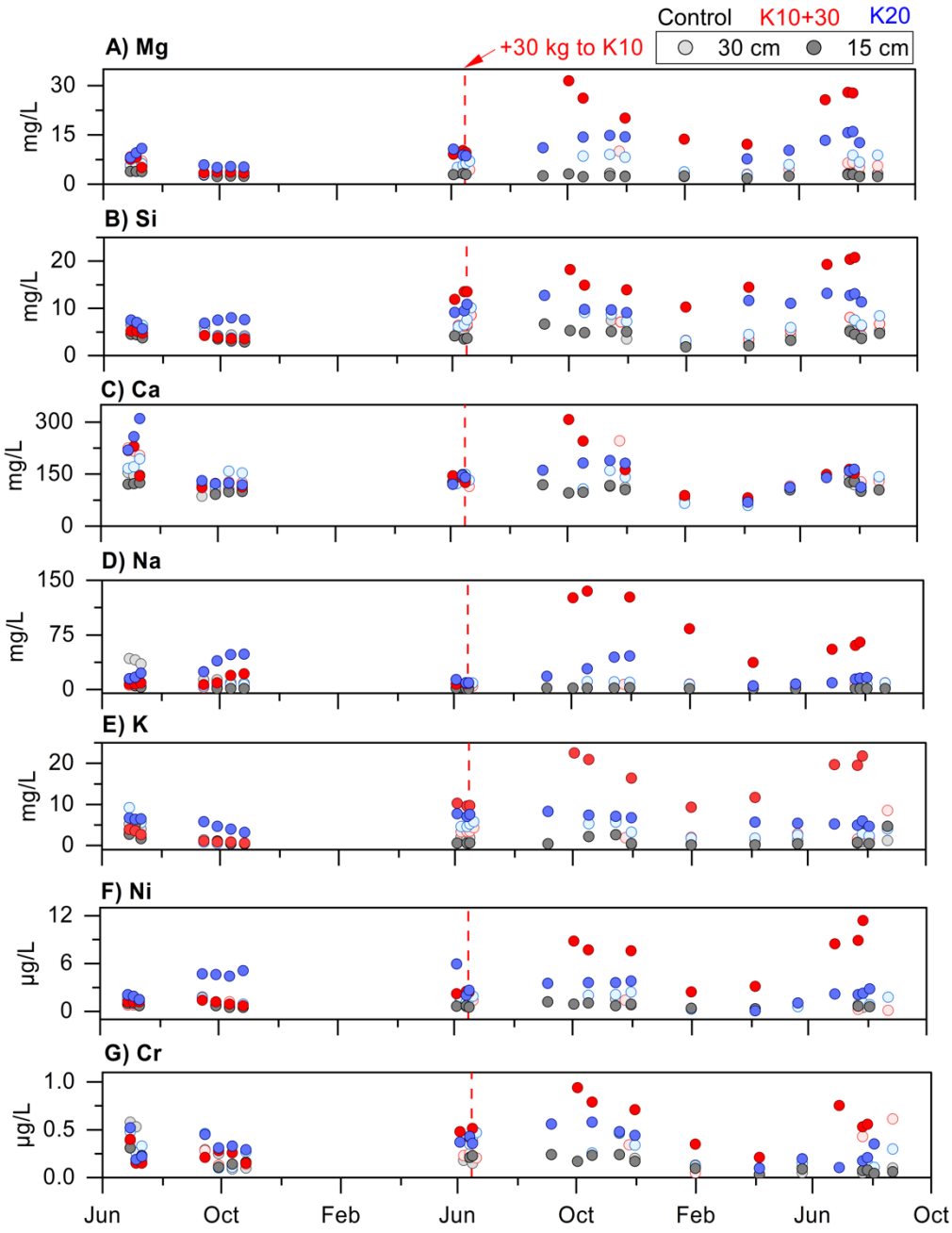

Figure 2.7. Concentrations of major cations, trace elements, and macronutrients in porewaters at 15 and 30 cm depths in the control, K10+30, and K20 plot over three monitoring periods. Larger data gaps occur when water samples were unobtainable, e.g., during winter months.

Porewaters were overall dominated by alkaline metals Ca and Mg rather than alkali earth elements Na and K for the entirety of the experiment; however, four groups of sample clusters are identified (Fig. 2.8). Samples for Figure 2.8 and Figure 2.9 are numbered 1 through 22 corresponding with the date of sample collection (e.g., 1 = the first sample day on June 30, 2021, 22 = the last sample day on August 23, 2023). If samples were not collected on a given date, the number ID is skipped until the next date of sampling. The first group contains all the control samples, and K10 and K20 samples from the end of the first monitoring period showing near negligible Na and K concentrations and Ca and Mg concentrations within the control range. The second group is characterized by elevated Ca and Mg relative to the control, and slightly elevated Na and K levels; this group is most notably comprised of porewaters collected within one month of amending the plots, but also K20 samples from the second monitoring period and the K10+30 in the final monitoring period. The third group is characterized by elevated concentrations of Ca and Mg as well as Na and K and are represented by K10+30 porewaters collected near the end of the second monitoring period following the second amendment. The fourth group, which consists of K20 samples at the end of the first and K10+30 at the beginning of the third monitoring period, shows porewaters slightly elevated in Na and K but within the control range for Ca and Mg.

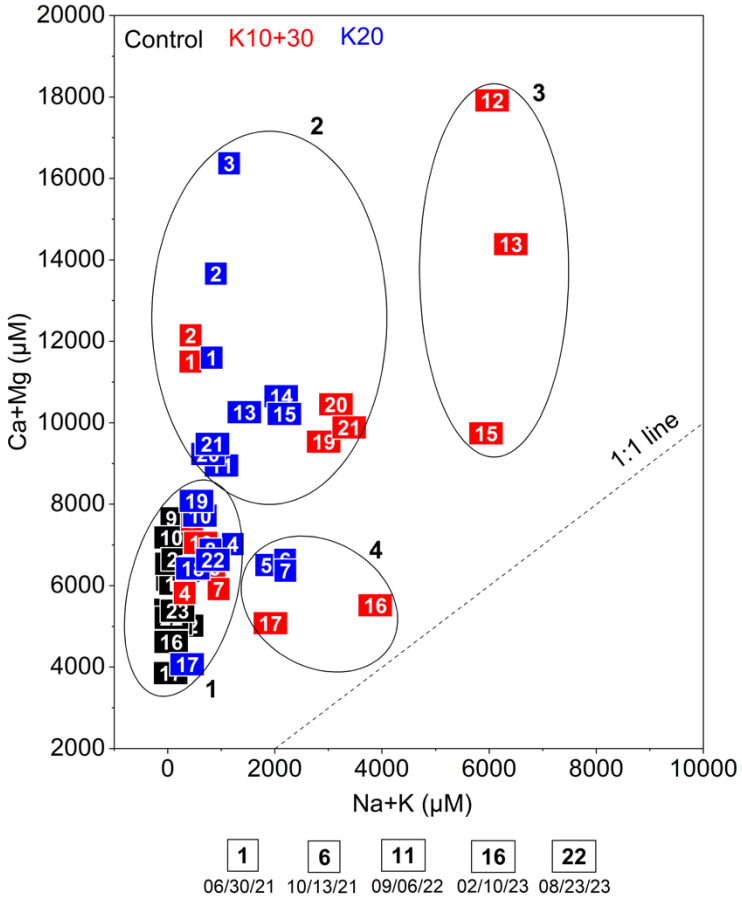

Figure 2.8. Ionic relationships between Ca + Mg and Na + K concentration sums in water samples collected at 15 cm from the control, K10+30, and K20 plots.

All control data points plot near or on the 1:1 calcite weathering relation between major cations and alkalinity regardless of weathering agent correction, suggesting calcite weathering in the control plot is the primary source of cations (Fig. 2.9). Once corrected for additional weathering agents [e.g., nitric (NO_3^-) and sulfuric acid (SO_4^{2-}); Appendix D] and the effects of NaCl dissolution derived from high rock:water ratios, mineral weathering producing divalent and monovalent cations exhibit a near 1:1 increasing trend with alkalinity (Fig. 2.9C). Initial data points following amendment of the K20 plot, final K20 concentrations, and final concentrations 1.5 yr after reamending the K10+30 plot

demonstrate the greatest observed relation between cations and alkalinity plotting on the 1:1 weathering line (Fig. 2.9A, C).

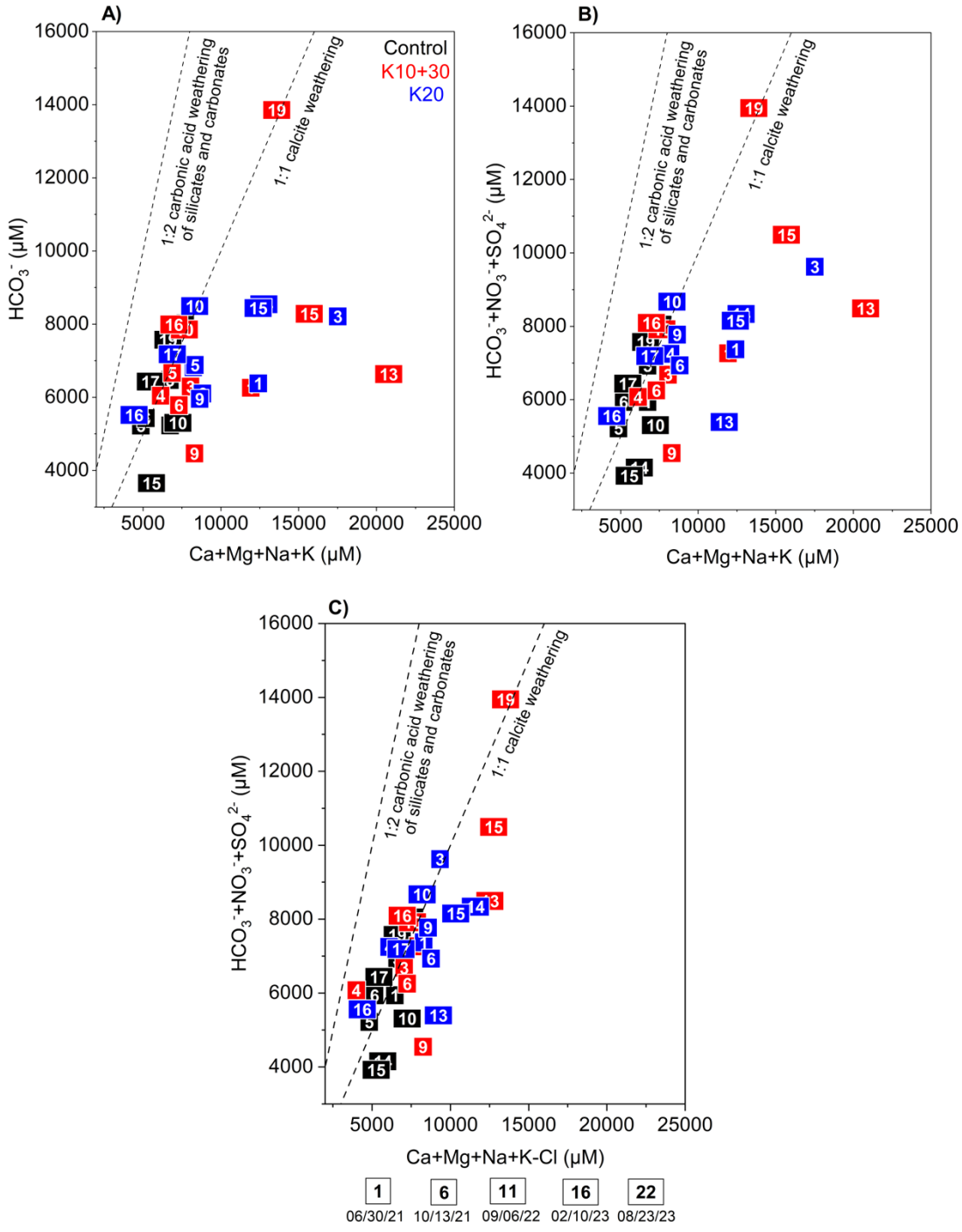

Figure 2.9. Major cation sum (Ca+Mg+Na+K) concentrations as a function of alkalinity in 15 cm porewater samples (A), alkalinity corrected for additional weathering agents (B), and total cation corrected for NaCl (C). Dashed lines indicate the stoichiometric ratio for calcite weathering and bicarbonate formation (1:1) and carbonic acid weathering of silicate and carbonate minerals (1:2).

2.6.3.3 Stable C and O isotopes

The $\delta^{13}C$ and $\delta^{18}O$ values of the carbonates within the Gahcho Kué kimberlite residues averaged -11.6‰ and +19.0‰, respectively, while soil carbonate averaged -0.01‰ and +20.9‰, respectively (Fig. 2.10). Marine carbonates (0‰) are depicted and are the typical carbon isotopic signature for limestone and soils formed in limestone, while negative values indicate secondary or pedogenic carbonates as a result of soil weathering processes (Rabenhorst et al., 1984). As the kimberlite residues did not contain any measurable organics, only the soils were analyzed for organic isotopic signatures, averaging -27.0‰ and +9.9‰ for $\delta^{13}C$ and $\delta^{18}O$ values, respectively. These organic carbon isotopic signatures are dependent on photosynthetic pathways of plants, most commonly C3 plants (-27‰) as depicted in Figure 2.10.

Samples for isotopic analyses collected from the field experiments included gases from 20 cm depths and porewater DIC from 15 cm depths. Soil pore space CO_2 yielded average $\delta^{13}C$ and $\delta^{18}O$ values of -24.3‰, -24.9‰, and -17.1‰, and +22.9‰, +28.3‰, and +25.5‰ for the control, K10+30, and K20 plots, respectively. Porewater DIC yielded $\delta^{13}C$ values of -15.5‰, -19.8‰, and -18.1‰ and $\delta^{18}O$ values of -6.5‰, -6.9‰, and -7.2‰ for the control, K10+30, and K20 plots, respectively. Isotopic compositions of DIC are composed of essentially two sources of inorganic carbon, atmospheric carbon in rainfall that has reacted with carbonates and CO_2 derived from soil respiration (Dubois et al., 2010).

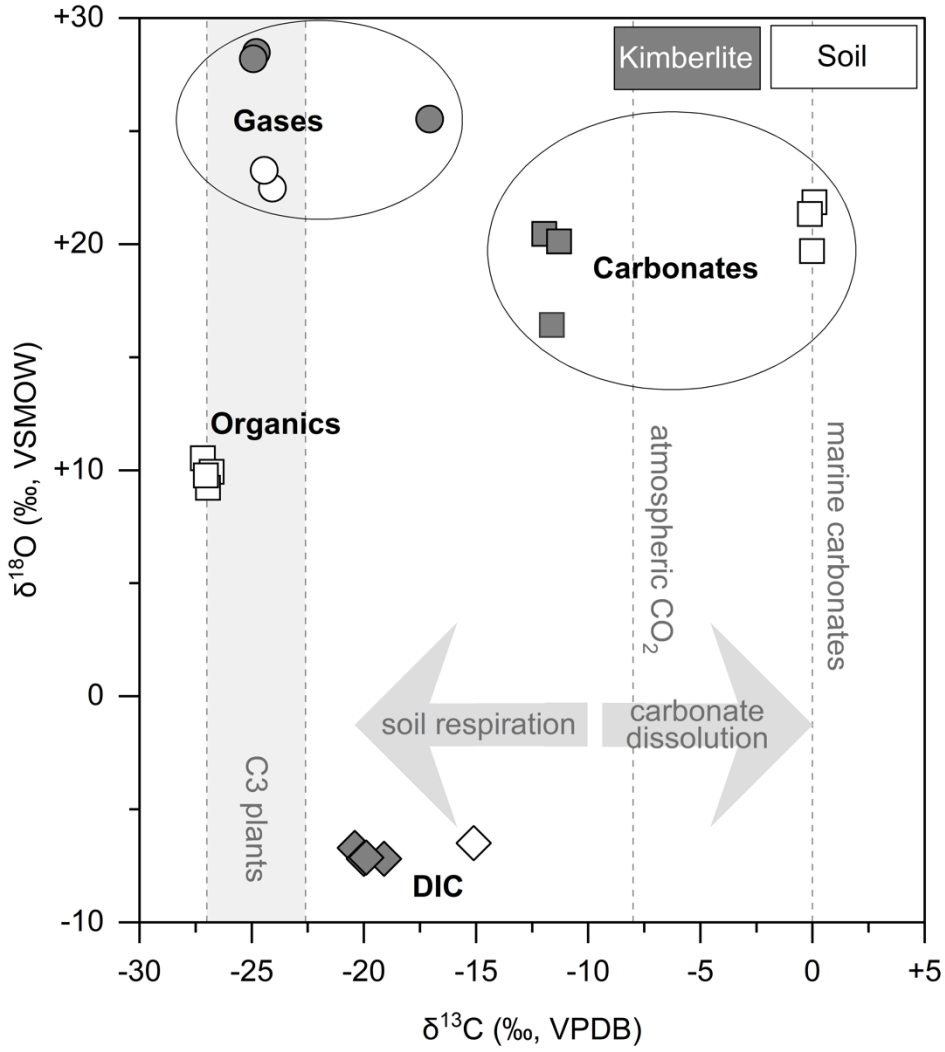

Figure 2.10. Stable carbon ($\delta^{13}C_{VPDB}$) and oxygen ($\delta^{18}O_{VSMOW}$) isotope compositions for organic and inorganic carbon in soils and kimberlite, and porewater DIC and gaseous CO_2 in the control, K10+30, and K20 plots. $\delta^{13}C$ values for marine carbonates is from Rabenhorst et al. (1984) while atmospheric CO_2, the range for soil respiration, and organics derived from C3 plants are provided by Dubois et al. (2010) and Schulte et al. (2011).

2.6.3.4 Carbonate precipitation

No increase of TIC relative to the control was observed in either amended plot within a 25 cm soil profile in the second monitoring period, but in the third monitoring period, a ~1.5%C increase was observed in the amended plots 15 cm from the surface (Fig. 2.11). The TIC of the control plot remained within a 1–2% range throughout the soil profile (Fig. 2.11). The amended plots exhibited lower percentages of TIC at the surface and increased to control levels with depth, exceeding the control range only in the third monitoring period.

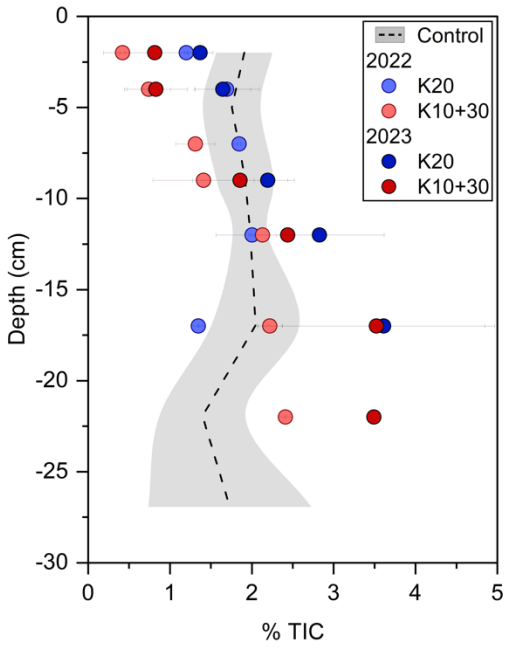

Figure 2.11. The TIC (%C) of field plot soil cores (0–25 cm) from the K10+30 and K20 plots in 2022 (n=6) and 2023 (n=6), approximately 1 yr apart. The control range for TIC is averaged over the second and third monitoring periods (n=12).

2.7 Discussion

2.7.1 Suitability of kimberlite residues for ERW

Passive carbonation of kimberlite residues has been documented at Canadian and South African mines and suggests these mine wastes could be utilized as an ERW feedstock (Wilson et al., 2011; Mervine et al., 2018; Paulo et al., 2021; Stubbs et al., 2022). The Gahcho Kué residues, notably rich in MgO (27.1 wt.%), offer relatively fast dissolution rates due to the presence of forsterite (9.2 wt.%) and lizardite (29.4 wt.%) which have been studied extensively in the context of CO_2 removal (Oelkers et al., 2008, 2018; Daval et al., 2013; Power et al., 2013b; Moosdorf et al., 2014; Farhang et al., 2017; Goll et al., 2021). These residues are also fine grained (D80 ≈ 175 µm) with high surface areas making them suitable for ERW (Table 2.2). Similarly, South African kimberlite residues from the Voorspoed and Venetia Diamond Mine show promise having substantial abundances of Mg-silicates (e.g., lizardite and diopside), low carbonate content and minimal potential for metal and sulfur release. McDonald et al. (2024) outline other favourable attributes, including D80 particle sizes ranging from ~100–520 µm. Comparatively, ERW field experiments have applied basalt powders with D80 particle sizes within a 267–1770 µm range and surface areas within a 1.0–2.7 m^2/g range (Larkin et al., 2022; Paessler et al., 2023; Beerling et al., 2024). Column and mesocosm studies have managed applications of finer grained material (D80: <100 µm), although their corresponding surface areas (1.5–20 m^2/g) are less than or similar to that of the aforementioned kimberlite residues (6.5–20.6 m^2/g; Amann et al., 2020; te Pas et al., 2023; Honvault et al., 2024). Thus, the finer grain size of processed fine residues compared to field applications of basalt, and high surface areas despite coarser grains

than intentionally pulverized material, renders this mass produced mine waste physically suited for ERW applications.

According to the Geochemistry of Rocks of the Oceans and Continents (GEOROC) database, Gahcho Kué kimberlite and South African kimberlite from Venetia and Voorspoed Diamond Mine exceeded the average SiO_2 content of kimberlites (32.3 wt.%) but fell below or near the CaO+MgO average (35.5 wt.%; Fig. 2.12A). Basalt, the leading feedstock in ERW applications (Beerling et al., 2018, 2020), exhibited a CaO+MgO average (16.6 wt.%) nearly half that of kimberlite and a higher SiO_2 average (49.2 wt.%; Fig. 2.12A). Basalt has demonstrated efficient rates in CO_2 removal, nutrient provision, and increasing crop yield across various agricultural settings (Haque et al., 2019a; Lefebvre et al., 2019; Larkin et al., 2022) and modelling studies (Beerling et al., 2020; Goll et al., 2021; Lewis et al., 2021). Assuming complete carbonation of the average CaO (9.5% ±2.2) and MgO (7.1% ±3.1) content in basalt, 0.15 ±0.05 t of CO_2 could be trapped as carbonate minerals per tonne of basalt, and ~0.30 t CO_2/t basalt if considering solubility trapping. Compared to the average CaO (10.7% ±6.4) and MgO (24.8% ±7.3) content in kimberlite, full carbonation rates at a 1:1 molar ratio with carbon amount to 0.35 ±0.13 t CO_2/t kimberlite and ~0.70 t CO_2/t kimberlite if considering solubility trapping.

Major constituent minerals common between kimberlite and basalt are relatively faster weathering silicates and are more efficient in CO_2 removal. In neutral pH environments, dissolution rates of forsterite ($10^{-10.6}$ mol/m^2/s) and pyroxene minerals (10^{-12} to $10^{-11.1}$ mol/m^2/s) are some of the fastest rates observed in each rock composition (Palandri and Kharaka, 2004), varying in abundance due to their ultramafic and mafic

nature. Primary differences in mineralogy include higher abundances of plagioclase feldspars ($10^{-12.6}$ to $10^{-10.9}$ mol/m^2/s) and varying traces of amorphous glass ($10^{-11.9}$ mol/m^2/s) in basalt (Lewis et al., 2021), and considerable quantities of serpentine minerals (e.g., lizardite: $10^{-12.4}$ mol/m^2/s) in kimberlite (Mervine et al., 2018; Kjarsgaard et al., 2022). Serpentine minerals contribute the most to the CDR capacity of kimberlites owing to their high potential for Mg release, large surface areas to facilitate reactions with CO_2, and abundance in their mineralogical assemblage (Power et al., 2013a, 2013b). One mineral group, common in basalt and kimberlite, that has gained increasing attention for CDR potential are smectites ($10^{-12.8}$ mol/m^2/s; Palandri and Kharaka, 2004; Zeyen et al., 2022). In kimberlites, the smectite mineral saponite has demonstrated incredible reactivity contributing to high specific surface areas (13.8–48.0 m^2/g; Mervine et al., 2018) and providing a significant source for cation exchange, releasing labile interlayer Mg and Ca ions rather than from dissolution (Zeyen et al., 2022).

Basalt is generally preferred in agricultural ERW applications due to low Ni (125 mg/kg) and Cr (258 mg/kg) concentrations (Fig. 2.12B) and lower leaching potential (e.g., 0.05% Ni; te Pas et al., 2023). However, non-agricultural application sites may allow higher thresholds for metal release, in which the average Ni (1036 mg/kg) and Cr (1286 mg/kg) content in kimberlite may be accepted. Kimberlites typically contain higher levels of beneficial nutrients (e.g., P and K averages of 2332 and 9814 mg/kg) compared to basalts (1762 and 9244 mg/kg, respectively), suggesting feedstock suitability for agricultural and mine closure purposes (Fig. 2.12C). As kimberlite residues are enriched in MgO improving their CDR capacity, possess a greater abundance of fast weathering

Mg-silicates, and exhibit potential for nutrient co-benefits, kimberlite is presented as a prime candidate for widespread ERW.

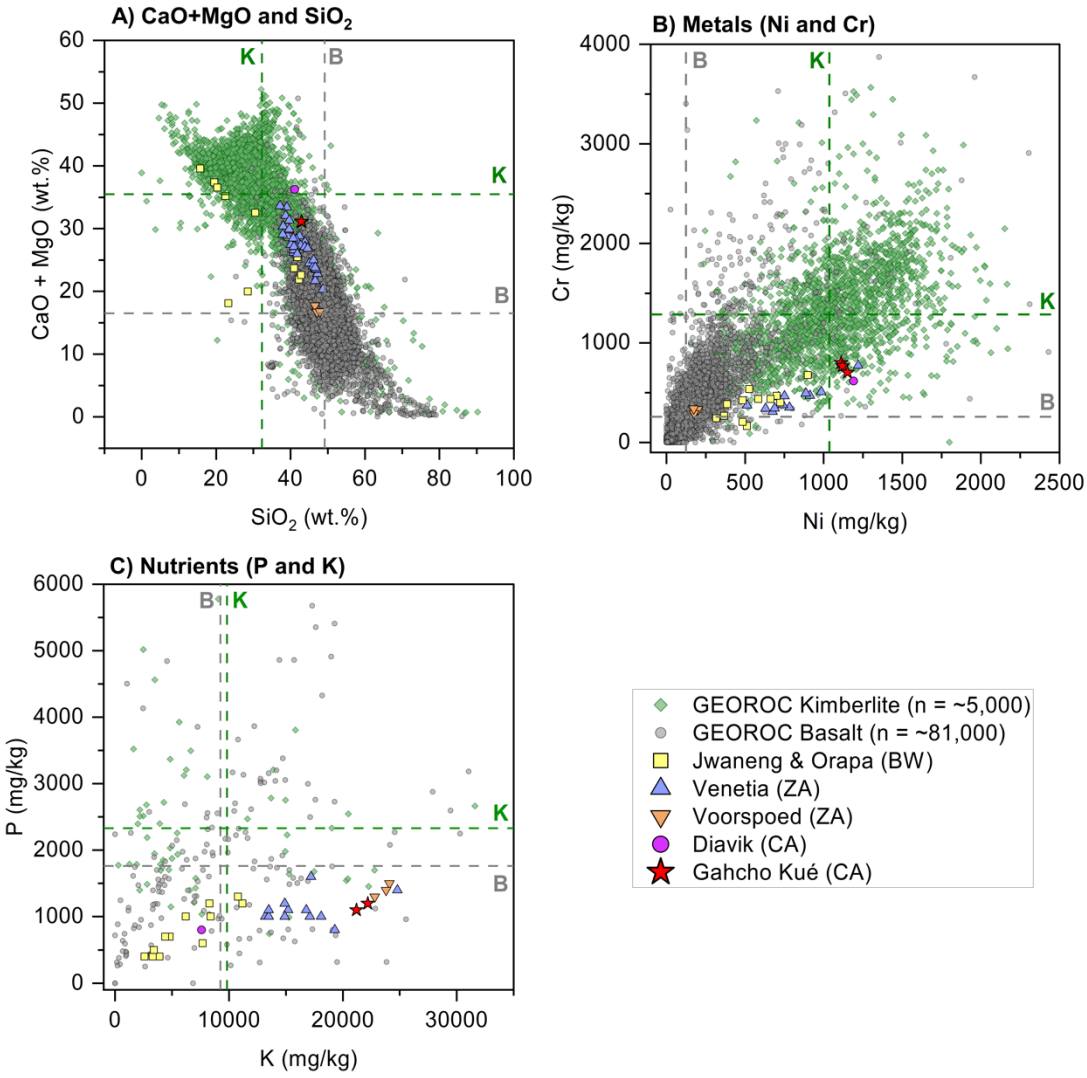

Figure 2.12. Concentrations of CaO+MgO and SiO_2 (wt.%; A), Ni and Cr (mg/kg; B), and P and K (mg/kg; C) in the whole rock geochemistry of kimberlite (K) and basalt (B) samples sourced from the GEOROC database. Additional kimberlites from Botswana, South Africa, and Canada are plotted for comparison. Dashed lines indicate the average parameters for kimberlite (green) and basalt (grey) samples in the GEOROC database.

2.7.2 Leaches: Reactivity assessment and predictors of water chemistry

The leaching tests assessed the reactivity of kimberlite residues in terms of easily released cations and their respective mineral origins. Within two weeks, half of the Ca content (2.8 wt.%) in the 100GK flasks was liberated (14.3 g/kg; Table 2.4), primarily from calcite (1.9 wt.%) dissolution, evident in the increase in pH value from 5.5 to ~6.5. Although initial Mg (16.3 wt.%) and Si (19.7 wt.%) concentrations were high, release of these elements was relatively low compared to Ca (9.2 and 8.9 g/kg; Table 2.4), indicating slower dissolution of Mg-silicate phases (Fig. 2.4; Pokrovsky and Schott, 2000; Brantley and Olsen, 2014; Heřmanská et al., 2023). Although other Mg-bearing phases present at lower abundances (e.g., sepiolite, talc, augite, and clinochlore) are not likely to significantly contribute to the cation pool, divalent cations exchanged from the interlamellar spaces of the smectite mineral saponite (21.5 wt.%) could appreciably enhance CDR rates (Zeyen et al., 2022). The presence of recalcitrant silicate minerals (e.g., quartz 30.7 wt.%; Table 2.2) in the soil explains the lesser Si release (0.4 g/kg) compared to the leaches containing the kimberlite residues (Table 2.4). This finding indicates that Si signals in mixed material flasks originate primarily from kimberlite silicate dissolution. Moreover, the faster dissolution of kimberlite silicate minerals compared to those in the local soil implies a more efficient CDR through silicate weathering in these ultramafic powders.

The experimental field plot amendment was equivalent to the 5GK (K20) and 10GK (K10+30, after reamendment) mixture leaches by mass if considering a 30 cm soil profile with an average bulk density of 1.2 g/cm^3. In a 15 cm profile the K20 and K10+30 plots contained 10 wt.% (10GK) and 25 wt.% (25GK) kimberlite, respectively.

Considering elements only became strongly correlated with kimberlite content in mixtures of at least 50 wt.% kimberlite – a dosage of 90 kg/m^2 with a mixing depth of 15 cm – cations signals were expected to be dominated by soil mineral weathering (Fig. 2.4). Additional or higher amendment applications would likely improve amendment weathering detection by composing a greater proportion of the soil system and therefore ensure CDR signals.

The maximum CDR potential (CDR_{pot}) achieved by the GK residues was estimated using the modified Steinour equation (Steinour, 1959) used by Clarkson et al. (2024; Eq. 1).

$$CDR_{pot} = \frac{M_{CO2}}{100\%} \times [\frac{MgO\%}{M_{MgO}} + \frac{CaO\%}{M_{CaO}} + \frac{K_2O\%}{M_{K2O}} + \frac{Na_2O\%}{M_{Na2O}}] \times \omega \quad (1)$$

where M is the molar mass of the subscripted compound and ω ranges from 1.5–1.7 and represents the additional drawdown per cation flux into the ocean. Based on the kimberlite oxide contents (wt.% of MgO, CaO, K_2O, and Na_2O), the Gahcho Kué residues could remove 500–567 kg CO_2/t. McDonald (2024) conducted reactivity tests using 100% CO_2 and estimated the CO_2 sequestration potential of Gahcho Kué residues at 11.9 kg CO_2/t based on easily extractable cations from non-carbonate sources. However, the leaches in this study resulted in higher releases of Ca and Mg, likely due to the longer experimental period (2 weeks compared to 2 days). Comparably, Paulo et al. (2021) and McDonald (2024) tested the reactivity of Venetia kimberlite residues using the same methodology and report a similar release of Ca attributed to calcite dissolution, and lower Mg release due to a lesser abundance of lizardite and saponite relative to the Gahcho Kué residues. Both studies estimated the CO_2 sequestration potential of Venetia

residues to be ~1–4× lower than that reported by McDonald (2024) for the Gahcho Kué residues.

The leaching tests provide valuable insights into cation release from soil and mineral amendments. Specifically, Si release was mainly attributed to kimberlite silicate dissolution, and Ca release attributed to carbonate dissolution in the soil and kimberlite. These insights aid in monitoring kimberlite residues applied to field conditions, allowing for differentiation between soil mineral and kimberlite mineral dissolution. While these leaches facilitated mineral dissolution due to agitation and exposure to high CO_2 gas beyond what may be expected in the natural environment, these types of preliminary tests are useful for assessing material reactivity, understanding cation release, and evaluating potential metal release.

2.7.3 Quantifying CO_2 removal

Accurately quantifying carbon removed by ERW requires a comprehensive understanding of the numerous geochemical processes and CDR pathways and how mineral weathering is intricately linked to fluid interactions, underscoring the importance of monitoring soil waters. Carbon coulometry is a precise method for measuring DIC and TIC to quantify solubility and mineral trapping, respectively (Fig. 2.13). However, assessing CO_2 fluxes presents a challenge due to the overwhelming CO_2 release from soil respiration that masks relatively minute CO_2 drawdown (Fig. 2.13). Even initial surface fluxes (-40 to -50 t CO_2/ha/yr; Fig. 2.5) only accounted for a small portion of the CDR potential of the kimberlite residues derived from the Steinour equation (K10+30: 50–227 t CO_2/ha, K20: 100–113 t CO_2/ha).

Identifying the prominent weathering minerals within the amendment and their respective molar ratios when removing CO_2 ensures accurate partitioning of total CDR rates. In this study, forsterite and lizardite were the dominant silicates in the kimberlite amendment, leaching Si into porewaters. Based on Equations 2 and 3, forsterite and lizardite weathering generate four and three moles of HCO_3^- for every mole of Si, respectively. Additionally, for every mole of Ca released from calcite weathering (Eq. 4), two moles of HCO_3^- are generated; however, this ratio accounts for the CO_2 molecule within the calcite structure, necessitating halving of this ratio to only account for newly removed CO_2.

$$Forsterite: Mg_2SiO_4 + 4CO_2 + 2H_2O \rightarrow 2Mg^{2+} + 4HCO_3^- + H_4SiO_4 \quad (2)$$

$$Lizardite: Mg_3Si_2O_5(OH)_4 + 6CO_2 + 5H_2O \rightarrow 3Mg^{2+} + 6HCO_3^- + 2H_4SiO_4 \quad (3)$$

$$Calcite: CaCO_3 + CO_2 + H_2O \rightarrow Ca^{2+} + 2HCO_3^- \quad (4)$$

Monitoring the composition of percolating water determines bicarbonate and cation export presumably into the water table (Amann and Hartmann, 2022). Soil percolation transports ERW products, thereby preventing saturation and fostering continued weathering of feedstock minerals (Hartmann et al., 2013). Profile monitoring extends to TIC as well, wherein core sampling aids in evaluating carbonate formation throughout the soil profile. Regardless of the CDR pathway, a better understanding of site-specific hydrology, particularly concerning deeper water percolation, proves necessary for accurately quantifying CO_2 removal.

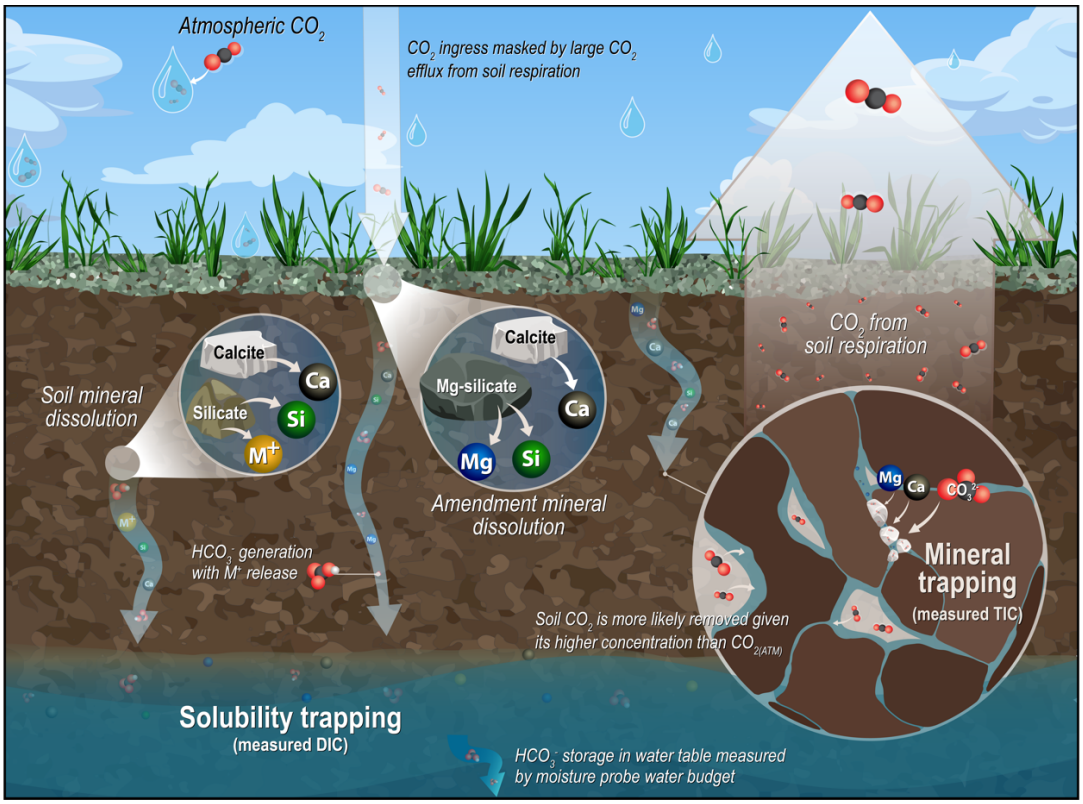

Figure 2.13. Conceptual diagram illustrating geochemical processes facilitating solubility trapping and CO_2 mineralization. Slightly acidic rainfall facilitates soil and amendment mineral weathering, releasing cations into solution generating bicarbonate anions, which can be measured as DIC, or precipitate as carbonate minerals, which can be measured as TIC. CO_2 emissions from soil respiration are depicted as large effluxes that mask the minimal ingress of CO_2 due to mineral weathering.

2.7.3.1 Hydrology and water balance

Timing of porewater sampling should best reflect the local water budget, e.g., after precipitation and during drying periods. However, continuous measurements of soil moisture is necessary for monitoring upper profile recharge and lower profile percolation to determine a site-specific water balance. Soil moisture levels are quantified volumetrically, expressed as cubic meters of water per cubic meter of soil. In this methodology, shallow (15 cm) moisture probes were assumed to detect all rainfall and calibrated so that any increase in moisture corresponded directly to the amount of rainfall

during the observed period. This soil-specific calibration established a direct relationship between moisture values and soil water content. For instance, consider that 1 mm of rainfall equates to 1 L over a 1 m^2 plot. Using this conversion, ~50 instances of moisture increase events were correlated to corresponding rainfall inputs in the control plot, resulting in the derivation of a linear relationship, as described by Equation 5.

$$\Theta = 0.0031V + 0.0036 \quad (5)$$

where Θ is the recorded volumetric water content (in m^3/m^3) and V is the volume of water (in L) in the system correlated with that moisture reading. Some evaporation, residual moisture, and recharge in the upper profile were expected; hence, the deeper (30 cm) moisture probes recorded dampened responses of soil moisture from rainfall inputs. Equation 5 was used to convert the 30 cm moisture to a volume of soil water in the control and amended plots, aiming to accurately characterize porewater percolation in the soil.

Recent protocols for calculating CO_2 removal stipulate that ERW products transported to a depth of at least 30 cm are regarded as removed carbon (Isometric Standard, 2023). Therefore, percolation values in this study comprised the water passing the 30 cm probe (Appendix B). These values assumed negligible lateral flow due to the site possessing no significant slope, and negligible evaporation at depth. Percolation values (V_P) were calculated by determining the difference in average soil water content over 2 h intervals and summing them to derive monthly percolation values (Eq. 6).

$$V_P = \sum_{i=1}^{N_{mo}} \Delta\Theta_i \quad (6)$$

where *mo* represents each month from 1–12, N_{mo} is the total number of 2 h intervals in month *mo*, and $\Delta\Theta_i$ is the change in moisture for each 2 h interval in month *mo*. Periods of active rainfall were omitted from the sum, as soil recharge during these periods mask any signal of percolation. Typically, ~25% of the total rainfall recorded in each monitoring period percolated past the 30 cm probe into the water table. Introducing the percolation factor allowed for the estimation of annual CO_2 removed using DIC (Eq. 7) and quantification of carbonate and silicate weathering using Ca and Si loadings (Eq. 10; Eq. 11).

2.7.3.2 Quantifying CO_2 removal by solubility trapping

Monthly quantities of total CO_2 removed were calculated using DIC, a direct measurement of carbon in waters. To address data gaps resulting from limited sample collection, the monitored months were extrapolated to one year based on precipitation and percolation values, rather than time, to accommodate climate variability. These calculated rates were compared to those calculated using alkalinity expressed as HCO_3^-. The concentrations used in these calculations are water leachates from the 15 cm sampler, as mineral weathering detections in the lower profile for all parameters were less apparent. CDR rates using DIC and alkalinity were calculated using Equations 7 and 8, respectively.

$$CDR\ (g\ CO_2/m^2/yr) = \sum_{mo}\left[([DIC] \times V_P) \times \frac{1\ g}{1000\ mg} \times \frac{M_{CO_2}}{M_C}\right] \times \left(\frac{P_{year}}{P_{period}}\right) \quad (7)$$

$$CDR\ (g\ CO_2/m^2/yr) = \sum_{mo}\left[([Alk] \times V_P) \times \frac{1\ g}{1000\ mg} \times \frac{M_{CO_2}}{M_{HCO_3^-}}\right] \times \left(\frac{P_{year}}{P_{period}}\right) \quad (8)$$

where [*DIC*] and [*Alk*] are the average concentrations (mg/L) for the respective parameter over each month, V_P is the total percolation value (L) for the respective month, and M_{CO2}, M_C, and M_{HCO3}- are the molar masses of each form of carbon. The sequestered CO_2 for each month was summed and extrapolated to one year by multiplying the amount of precipitation throughout that year (P_{year}) and dividing by the amount monitored over the monitoring period (P_{period}; Appendix B). This extrapolation acknowledges the variability of fluid interactions throughout the year and is used as opposed to multiplying the monitoring period removal sum to account for the remaining months nominally.

The K10+30 and K20 plots exhibited comparable CDR rates, achieving 1.2 and 1.3 t CO_2/ha over 3 yr, respectively, in contrast to the local soil CO_2 consumption (~0.2 t CO_2/ha/yr; Fig. 2.14). These CDR rates in the amended plots were derived from local soil and kimberlite mineral weathering (Eq. 9), where ~22–28% was contributed by silicates (Eq. 11) and ~72–78% was from calcite weathering after adjusting to only account for new CO_2 removed (Eq. 10). Through kimberlite weathering alone in the K10+30 and K20 plot, an additional 0.7 and 0.9 t CO_2/ha were removed over 3 yr.

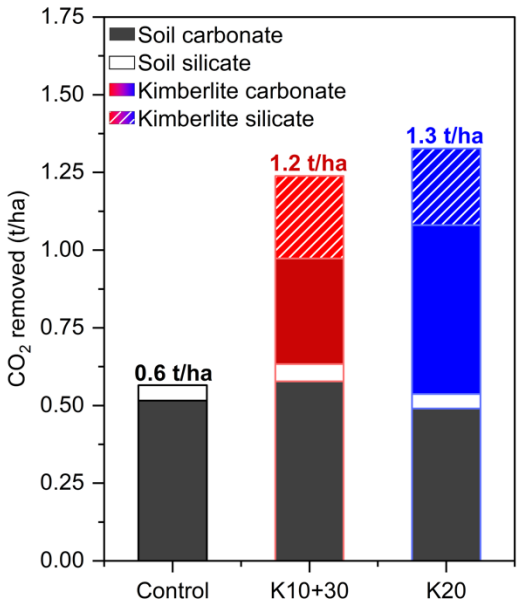

Figure 2.14. Cumulative CO_2 removal (t CO_2/ha) over 3 yr calculated via DIC and divided into carbonate and silicate weathering of the soil and kimberlite residues in the control, K10+30, and K20 plots.

Carbonate weathering must be considered in the case of calcareous soils and carbonate-bearing amendments, therefore, CDR rates must account only for the quantity of new CO_2 removed (Eq. 4). CO_2 removal contributed by calcite dissolution was halved, correcting the overall CDR derived from DIC measurements to account for this contribution. The total CDR rate can be conceptualized as the sum of silicate and carbonate weathering components from both the local soil and the amendment (Fig. 2.13; Eq. 9).

$$CDR_{total} = (CDR_{silicate} + CDR_{carbonate})_{Soil} + (CDR_{silicate} + CDR_{carbonate})_{Amendment} \quad (9)$$

where CDR_{total} is the total amount of CO_2 removed via solubility trapping calculated by DIC content in drainage waters which includes new and old CO_2 (Eq. 8), and $CDR_{silicate}$ and $CDR_{carbonate}$ are determined from mineral contributions in the local soil and added amendment. As mineral weathering is not a direct quantifier for CDR rates, the CDR_{total}

was partitioned into mineral weathering percentages relative to one another. These percentages were derived from dividing removal rates from Equations 10 and 11 by the removal rate sum calculated from cation releases rather than from direct inorganic carbon measurements.

The proportions of CO_2 removal contributed by carbonate and silicate weathering of the soil and kimberlite minerals were determined by comparing the Ca and Si concentrations, respectively. The additional CO_2 removal by kimberlite carbonate and silicate weathering was based on the increase in Ca and Si concentrations in porewaters compared to the control plot. The mineral weathering removal rates using cation release were calculated using Equations 10 and 11, respectively.

Carbonate weathering contribution:

$$CDR_{carbonate}\ (g\ CO_2/m^2/yr) = \sum_{Month}\left[([Ca] \times V_P) \times \frac{1\ g}{1000\ mg} \times {}^1\!/_2 \frac{M_{CO_2}}{M_{Ca}}\right] \times \left(\frac{P_{year}}{P_{period}}\right) \quad (10)$$

Silicate weathering contribution:

$$CDR_{silicate}\ (g\ CO_2/m^2/yr) = \sum_{Month}\left[([Si] \times V_P) \times \frac{1\ g}{1000\ mg} \times n \frac{M_{CO_2}}{M_{Si}}\right] \times \left(\frac{P_{year}}{P_{period}}\right) \quad (11)$$

where $[Ca]$ and $[Si]$ are the average concentrations (mg/L) for the respective cation for that month, n is substituted for the number of moles reacting to form HCO_3^- if assuming 100% lizardite contribution (n=3; Eq. 3) or 100% forsterite contribution (n=4; Eq. 2), and M_{Ca} and M_{Si} are the molar masses of the respective cation. Impacts from other strong acid weathering agents were expected to be negligible as sulfide minerals were not present nor was there any recent use of nitrogen fertilizers in the study site. Concentrations of NO_3^- and SO_4^{2-} were low throughout the experiment providing a negligible shift in the cross plot of HCO_3^- and major cations (remaining below or on a 1:1 line until corrected for Cl concentrations; Fig. 2.9B; Appendix D). Furthermore, non-carbonic acid neutralization

can be approximated based on soil pH and pCO_2, where a pCO_2 value at least 10 times atmospheric suggests that if the pH is above 5.99, which these porewaters are (Fig. 2.6C), stronger acid weathering is negligible (Dietzen and Rosing, 2023).

This methodology draws from the widely adopted practice of monitoring DIC and alkalinity for quantifying carbon removal via solubility trapping in ERW experiments (Amann and Hartmann, 2022; Larkin et al., 2022; Dietzen and Rosing, 2023; Kantola et al., 2023; Knapp et al., 2023; te Pas et al., 2023), and introduces novel applications of a moisture-probe derived water budget in a field setting. Such high dosages ensured solubility trapping detection and allowed for accurate partitioning into mineral weathering contributions derived from cation loadings percolating out of the soil system. Kimberlite residue amendments doubled the natural CDR rate of local circumneutral soils over 3 yr and is expected to continue improving CDR so long as DIC remains elevated from the control (Fig. 2.6B).

2.7.3.3 Quantifying CO_2 removal by mineral trapping

Kimberlite weathering and release of Ca and Mg could potentially precipitate carbonate minerals (e.g., calcite), storing CO_2 by mineral trapping in addition to the previously described solubility trapping quantified using DIC. Calcite remained supersaturated in porewaters throughout the experiment with greater saturation for the amended plots. Furthermore, dolomite supersaturation surpassed calcite in the amended porewaters in all monitoring periods (Appendix C), reflecting Mg release from the kimberlite residues. CO_2 removed via mineral trapping was calculated based on changes in TIC content of the soils over the experiment using Equation 12.

$$Mineral\ trapping\ (g\ CO_2/m^2) = \left(\frac{\Delta TIC}{100} \times \frac{m_{soil}}{m^2}\right) \times \frac{M_{CO_2}}{M_C} \quad (12)$$

where ΔTIC is the change of TIC (%) between the segmented initial and final soil cores, and m_{soil} is the estimated mass of soil in a square metre with a thickness of 10 cm (0–10 cm) and 15 cm (10–25 cm) based on a bulk density of 1.2 g/cm^3 (Table 2.1). Initial TIC content was derived from averaging values measured in 2–5 cm increments throughout ~25 cm cores collected from the control plot in 2022 and 2023 (n=12). The CO_2 removed via mineral trapping and solubility trapping achieved by kimberlite weathering is summarized in Table 2.5.

Table 2.5. CDR (t CO_2/ha) of kimberlite weathering based on changes in TIC (mineral trapping) and DIC (solubility trapping) over 3 yr.

	Mineral trapping (t CO_2/ha)	**Solubility trapping (t CO_2/ha)**	**Total sequestration (t CO_2/ha)**
K10+30	61 ±66	0.7	61.7 ±66
K20	89 ±44	0.9	89.9 ±44

The initial TIC of the kimberlite residues was 0.25%C corresponding with ~2 wt.% calcite (Table 2.2). This abundance suggests that in the 10+30 and 20 kg/m^2 dosage plot, approximately 0.8 and 0.4 kg of calcite was amended to the field soils, respectively. The control soil exhibited an average TIC content of 1.8%C ±0.4 throughout the soil profile (16.1 wt.% calcite), equating to 45 kg of calcite within a square metre to a depth of 25 cm. After three years of weathering, overall TIC content increased from control levels by 1.3%C ±1.9 and 1.4%C ±1.6 in the K10+30 and K20 plots (Fig. 2.11), indicating that 32.5 kg ±50 and 35.0 kg ±42 of carbonate was precipitated, respectively, in a 25 cm profile.

The observed TIC increase was a mixture of existing soil calcite, re-precipitated pedogenic carbonates, and calcite in the kimberlite. Differentiating these sources pose a challenge in accurately accounting for mineral trapped CO_2. These mineral trapping rates in addition to the solubility trapping rates would increase the total amount of CO_2 sequestered via kimberlite weathering substantially; however, the large uncertainty in TIC measurements due to soil heterogeneity results in uncertainty in the overall CDR rate of kimberlite weathering (Table 2.5). Furthermore, the high TIC content of the calcareous soils provides a large background signal that makes mineral trapping quantification unreliable.

Relatively high removal rates via mineral trapping have been demonstrated previously in ERW experiments (Manning et al., 2013; Haque et al., 2019; Vienne et al., 2022). Basalt, which contained no carbonates, applied to a mixture of dolerite and local soil (~0.1 wt.% $CaCO_3$) produced an annual mineral trapping rate of ~18 t CO_2/ha (Manning et al., 2013). Vienne et al. (2022) report a TIC increase of 12.4 t CO_2/ha after 99 d of basalt weathering, but with a high standard deviation that exceeds this rate (± 24.7 t CO_2/ha). Most basalts are characterized by trace amounts of calcite (typically <1 wt.%), and Lewis et al. (2021) reported that weathering of these carbonates have the potential to reduce CDR rates by 3% (Tawau basalt: 0.6 wt.% $CaCO_3$) to 30% (Cragmill basalt: 1.2 wt.% $CaCO_3$). Assuming the entirety of calcite content in the kimberlite amendment weathered out over 3 yr and re-precipitated, removing the same amount of CO_2 as initially released during weathering, the impact relative to the mineral trapping rates would be insignificant. Accurately quantifying mineral trapping remains a hurdle to

overcome in carbon accounting, especially with calcareous soils that are amended with carbonate-rich rock powders.

2.7.4 CO_2 sources

As with any ERW application, potential sources of carbon that may have become sequestered in the field plots included atmospheric CO_2 (0.04%) and its subsequent form as carbonic acid in precipitation and soil pore gas CO_2 (0.4–1.9%) derived from microbial respiration (Fig. 2.13). It is worth noting that soil pore CO_2 concentrations (0.4–1.9%) were 10 to nearly 50 times greater than atmospheric CO_2 concentrations. CO_2 fluxes were negative or less positive immediately following kimberlite amendment due to the initial reactivity of the material (Fig. 2.5B, C); however, there are uncertainties in flux magnitude as they were only measured during dry conditions. Under saturated conditions, soil respiration is reduced as a result of inhibited microbial activity, with rapid activity and increased CO_2 release during the drying period (Howard and Howard, 1993). Regardless, as kimberlite weathering slowed over time, soil CO_2 fluxes became indistinguishable between the control and amended plots (Fig. 2.5). ERW is often described as a NET that removes CO_2 from the atmosphere; however, soil CO_2 is likely the dominant source given its much greater concentration. Nevertheless, this biogenic carbon is likely derived from the atmosphere, fixed through photosynthesis (Wood et al., 2023; Fig. 2.13).

Stable carbon isotope data provides further evidence that DIC in soil porewaters originates from organic sources (Fig. 2.10). The ^{13}C compositions of the soil organic carbon (avg. $\delta^{13}C$ = -27.0‰) are consistent with organics derived from C3 plants (-23 to -

27‰; Schulte et al., 2011). While microbial respiration of the organic matter does not result in isotopic fractionation, soil pore gas (avg. $\delta^{13}C$ = -24.2‰) was enriched in ^{13}C by +2.8‰, suggesting some mixing of atmospheric CO_2 ($\delta^{13}C_{atm}$: -7.7‰; Schulte et al., 2011) either prior to or during sampling (Fig. 2.10). The fractionation between gaseous CO_2 and dissolved bicarbonate at circumneutral pH is +9.0‰ at 15ºC, the approximate pH of the soils (Mook et al., 1974). Given the ^{13}C composition of the pore CO_2, $\delta^{13}C_{DIC}$ values of approximately -18.0‰ would be expected. Porewater $\delta^{13}C_{DIC}$ values averaged -15.5‰, -19.8‰, and -18.1‰ for the control, K10+30, and K20 plots, respectively, consistent with the organic respiration range defined by Dubois et al. (2010). Thus, ERW suppresses soil respiration more than it removes atmospheric CO_2.

Soil inorganic carbon $\delta^{13}C$ values are near zero or slightly positive, reflecting typical values for marine carbonates (e.g., limestone; Fig. 2.10; Rabenhorst et al., 1984). Inorganic carbon isotopic signatures of bulk Gahcho Kué kimberlite residues are within the ranges reported by Giuliani et al. (2014) for $\delta^{13}C$ (-11.9‰ to +0.2‰) and $\delta^{18}O$ (+1.2‰ to +26.6‰), reflecting a global composition of kimberlites. While the kimberlite residues may shift bulk ^{13}C and ^{18}O compositions of amended soil given the high dosages, carbonate precipitation incorporating biogenic CO_2 in soils is unlikely to alter these isotope values as soil TIC is exceedingly high.

2.7.5 Metal and nutrient release

Concerns about releasing harmful metals from the weathering of rock powders applied to soils are a major obstacle for ERW implementation. While batch leaches showed minimal metal release from the kimberlite residues, prolonged weathering of

ultramafic feedstocks could lead to the accumulation of adverse elements (e.g., Ni and Cr; Dupla et al., 2023) posing risks to the environment and human health (Beerling et al., 2020; Haque et al., 2020). To evaluate the safety of kimberlite feedstocks, porewater concentrations were compared to surface water quality thresholds for nickel (25 µg/L) and total chromium (1 µg/L), emplaced by the Ontario Ministry of the Environment (MOE, 1979) and the Canadian Council of Ministers of the Environment (CCME, 1999), respectively.

Ni- or Cr-bearing minerals were not detected by XRD in the Gahcho Kué residues, yet such high initial concentrations suggest compounds below detection limits (e.g., nickel sulphides) or possibly substituted for Mg or Fe in forsterite or lizardite (Wang et al., 2024). The Gahcho Kué residues exceed the average kimberlite Ni content but remains below the Cr average, all the while exceeding the Ni and Cr average for basalt (Fig. 2.12B). Reactivity assessments determined that Cr release from the kimberlite was consistently within water quality regulations, while Ni concentrations exceeded this regulation by ~65 µg/L (Fig. 2.3). However, in the field experiment, Ni and Cr levels in the amended plots exceeded control soils, yet the maximum concentrations of 11.3 and 0.94 µg/L, respectively, remained below surface water quality thresholds (Fig. 2.7F, G).

Initial environmental assessments of reference lakes prior to the construction of Gahcho Kué mine reported Ni and Cr levels well below 1 µg/L (Golder Associates, 2014). In October 2020, as part of a routine water surveillance program, mining activity impacts (e.g., FPK impoundment discharge) on the environment were assessed, including testing of the reference lakes assessed in their initial assessment (De Beers Canada Inc., 2020b). Results showed elevated Ni concentrations to 5 µg/L, while Cr remained below 1

µg/L (De Beers Canada Inc., 2020b). Thus, <0.0005% of the total Ni and Cr content (Fig. 2.12B) became mobile during the weathering of the kimberlite residues at Gahcho Kué and in the experimental plots. The disparity in metal release, with Cr being ~2.5 orders of magnitude lower than Ni, is likely attributed to Cr being present in more resistant chromite sources emplaced in serpentine minerals (Oze et al., 2004; Fig. 2.3). Cr release from the 100GK leachates were also within the blank range (0.2 µg/L ±0.1) suggesting no Cr was released. While the alkaline pH of these environments may prevent the mobility of these deleterious metals in waters, Ni can be adsorbed and retained in sediments for longer periods (Vienne et al., 2022). The presence of clay minerals in kimberlite residues suggests the potential for metal retention, with accumulation possibly facilitated by additional dosages and the adsorptive properties of clays (Pogge von Strandmann et al., 2022). Nevertheless, even with high dosages (e.g., 400 t/ha), Ni and Cr remained below strict water quality guidelines.

The addition of mineral feedstocks can replenish essential macronutrients (e.g., P and K), improving vegetation health and yield (Swoboda et al., 2022). The gradual release of nutrients from amendment weathering can aid revegetation efforts, offering a sustainable alternative to costly fertilizers (Mohammed et al., 2014). Although Gahcho Kué residues are below global kimberlite P averages, they notably exceed the K average due to microcline and phlogopite abundance comprising 27.2 wt.% of the kimberlite (Fig. 2.12C; Table 2.2). PCA of the batch leach data indicated that P originated from soil influence, and as XRD indicated an absence of phosphate minerals [e.g., apatite ($Ca_5(PO_4)_3(OH,F,Cl)$)] and geochemical data showed similarly low percentages of P-bearing oxides compared to soils (Table 2.3), amending soils with kimberlite residues had

no effect on P levels and remained consistent with background levels (Appendix D). Whereas PCA of leachates showed a strong correlation between K and kimberlite content, leaching 25.8% of the initial K concentrations (Fig. 2.4; Table 2.4). The long-term potential for K inputs is substantial, with concentrations remained elevated over multiple monitoring periods without the need for re-amendment (e.g., K20; Fig. 2.7E). K-feldspars (e.g., microcline) compose 12.1 wt.% of the kimberlite residues suggesting a slow-releasing K source; however, K bound to K-feldspars are relatively inert compared to K fertilizers (Bakken et al., 2000). To contrast, Manning et al. (2017) report that K-feldspar rich rock powders would likely perform as a slow-inputting K source, while phlogopite containing rocks, like these kimberlite residues (15.5 wt.%), successfully impact crop yield on par with KCl fertilizer.

2.7.6 Implications for enhanced rock weathering using mine wastes

2.7.6.1 On-site ERW

The Gahcho Kué Diamond Mine plans to process 44.3 Mt of kimberlite ore, yielding 28.8 Mt of coarse processed kimberlite (CPK) and grits (0.25–6 mm) and 15.5 Mt of FPK (De Beers Canada Inc., 2020). Operational activities involve transporting FPK as a slurry to a containment facility with a capacity of 6.1 Mt, while CPK is stockpiled at a second facility capable of holding up to 27 Mt (De Beers Canada Inc., 2024). As part of their closure plan for 2030, FPK will be used as backfill in the Hearne open pit, with any residual FPK in the containment facility capped to mitigate further reactions (De Beers Canada Inc., 2024). The slopes of the CPK facility will be graded to ~35 m above surrounding areas, with excess material used as backfill for the Hearne and 5034 pit (De

Beers Canada Inc., 2024). From construction until mine closure (~16 yr) and based on the estimated CO_2e emission of ~723 kt from 2015 to 2021 and average annual ~130 kt CO2e generated during full operation (De Beers Canada Inc., 2023), Gahcho Kué operations may emit ~1.9 Mt CO_2e, primarily from diesel-powered generators (De Beers Canada Inc., 2024). Although, as Gahcho Kué nears closure, mine production is likely to slow emitting CO_2 emissions below this average; therefore 1.9 Mt CO_2e is an upper estimate of potential emissions.

Novel mine waste management practices offer potential to optimize CDR during operation and improve site remediation post-closure. Conventional impoundments effectively store megatonnes of processed ore slurries, preventing weathering, leaching, and CO_2 reactions. In contrast, the aim of ERW is to widely distribute rock powders to optimize exposure. By strategically distributing mine residues over land, mineral surfaces can interact more effectively with reactive fluids, thereby augmenting ERW efficiency and CDR potential (Power et al., 2013a). For instance, at the Mount Keith Nickel Mine in Western Australia, recommendations were made to modify tailings management practices, such as employing thinner slurry flows and larger impoundments to enhance surface exposure and facilitate brucite [$Mg(OH)_2$] carbonation (Wilson et al., 2014). At Gahcho Kué, assuming complete carbonation of CaO and MgO and subsequent carbonate mineral formation at a 1:1 molar ratio with carbon, the estimated amount of FPK produced over the life of the mine has the potential to remove 5.0 Mt of CO_2, 9.9 Mt of CO_2 if considering solubility trapping. Thus, residue management that facilitates reactions with CO_2 could offset the anticipated emissions at Gahcho Kué by 2–5× through the weathering of their FPK only.

Even with distributed residues, this study demonstrated how high rock-to-water ratios may impede CDR efficiency, as seen in the K10+30 plot (400 t/ha) where porewaters became saturated with respect to lizardite after reamendment (Appendix C). The K20 plot, treated with a dosage of 200 t/ha, achieved comparable CDR to the K10+30 plot after 3 yr, highlighting the efficacy of lower dosage rates. By introducing better on-site management practices for mine residues, passive weathering and CO_2 removal can be optimized, even at a relatively high dosage (e.g., 200 t/ha). Thus, longer field trials are warranted to monitor feedstock weathering and gradual silicate dissolution, particularly at lower rock-to-water ratios (Stubbs et al., 2022).

Upon mine closure, processed residues are further isolated through capping or used as backfill in retired mining pits along with waste rock, often stored sub-aqueously (Reid et al., 2009). Post-closure remediation efforts are necessary to prevent environmental and community impacts (Komljenovic et al., 2020); however, measures preventing further reactions of mafic and ultramafic mine wastes can hinder passive carbonation (Wilson et al., 2011). Exploring storage methods for environmentally safe mine wastes could instead enhance CDR while addressing waste management concerns. For instance, the Gahcho Kué mine footprint (~1300 ha; De Beers Canada Inc., 2024) presents an opportunity for a large-scale ERW deployment, utilizing processed residues to rehabilitate disturbed lands. De Beers plans to revegetate the mine by repurposing overburden and lakebed sediment as a substrate and growing media (De Beers Canada Inc., 2024). Reclamation efforts also include loosening compact zones (e.g., roads) that make up 160 ha of the mine to encourage vegetation establishment (De Beers Canada Inc., 2024), providing opportunities to integrate residues with soil to enhance CDR while

promoting plant growth. Incorporating residues into these remediation efforts would facilitate CDR, offsetting historic GHG emissions when the mine was operational.

Technosols, engineered soils comprised of anthropogenic materials like mine wastes, show promise in promoting vegetation growth, soil stability, fertility, and CDR (Weiler et al., 2024). Incorporating mafic and ultramafic processed residues into technosols offers a cost-effective strategy for mine closure remediation and carbon removal (Allory et al., 2022; Ruiz et al., 2023). For example, Miller and Naeth (2017) demonstrated that kimberlite residues from the Diavik Diamond Mine (Canada) combined with lakebed sediment (25:75) was a successful substrate for revegetation but recommend incorporating crushed rock to increase macropore storage allowing time for seed germination. Diversion of the majority of waste could be through combining coarse and fine residues with waste rock in residue impoundments to improve soil texture and enhance technosol horizonation (Santini and Banning, 2016; Cross et al., 2021), potentially transforming these impoundments into viable agricultural sites post-remediation (Yu et al., 2023).

2.7.6.2 Off-site ERW

The vast reserve of known kimberlite occurrences (~6,500) worldwide presents a significant opportunity for carbon sequestration, but only ~1,000 host macro-diamonds of economic value that are feasible for extraction (Kjarsgaard et al., 2022). The global production of diamonds from 1854 to 2019 is estimated at 5.9 billion carats (Kjarsgaard et al., 2022), which would have generated approximately 8.9 Gt of kimberlite residues assuming an average ore grade of ~1.5 carats per tonne kimberlite (Gurney et al., 2005).

These residues would include both fine and coarse fractions located at active and closed diamond mines in countries such as Angola, Australia, Botswana, Brazil, Canada, China, Democratic Republic of the Congo, Lesotho, Russia, Sierra Leone, South Africa, Tanzania, and Zimbabwe (Kjarsgaard et al., 2022). Existing mine residues are readily available fine-grained feedstocks that offer a pathway towards achieving net-neutral mining operations and for post-closure remediation efforts.

Repurposing industrial waste within the circular economy framework presents an opportunity to optimize global CDR through ERW, while addressing waste management challenges. Renforth et al. (2011b) acknowledge that the prime limitation for sufficient CDR is material availability, showcasing the opportunity for managing disposed silicate waste (e.g., mine waste, cement dust, and slag) and the global carbonation potential of their annual production. Globally, 7–17 Gt of silicate waste is produced annually with Manning and Renforth (2013) equating this production to a solubility trapping capacity of 1.2–2.0 Gt CO_2, excluding historically deposited materials. Applications of environmentally safe industrial wastes have proven effective in remediating degraded soils from mining and agriculture (Baragaño et al., 2019; Ramos et al., 2020, 2021; Díaz-Piloneta et al., 2022), with recent consideration for ERW projects. Steel slag, for instance, contains Ca- and Mg-silicates, free lime [CaO], portlandite [$Ca(OH)_2$], and abundant micronutrients, making it a viable industry waste for CDR (Reddy et al., 2019), with large quantities available (200–250 kg/t of steel; Díaz-Piloneta et al., 2022). Crushed returned concrete has shown promise as a soil amendment, achieving rapid soil neutralization and maximum CDR rates of ~0.5 t CO_2/ha over 10 months due to its reactive Ca phases (e.g., [$Ca(OH)_2$]; McDermott et al., 2024). ERW operations tend to

use quarry by-products from volcanic aggregate mining as they are discarded without prior chemical processing (Ramos et al., 2020), and contain relatively fast-weathering silicate phases (e.g., dunite residues: 20–35 wt.% olivine; Baragaño et al., 2019).

Basalt powder, as mentioned earlier, is the most common quarried feedstock used for ERW, with recent ERW field trials demonstrating varying CDR rates by orders of magnitude (Larkin et al., 2022; Paessler et al., 2023; Beerling et al., 2024). For example, a hectare-scale field trial using andesitic basalt was conducted in Sabah, Malaysia on an oil palm plantation, resulting in a maximum CO_2 removal of 1.0 t CO_2/ha over 3 yr, quantified through alkalinity measurements from catchment stream waters (Larkin et al., 2022). Another ERW study in the United States Corn Belt applied metabasalt at an annual dosage of 50 t/ha, similar to the single dosage applied by Larkin et al. (2022); however, significantly higher rates were observed (6.7–14.3 t CO_2/ha over 4 yr), derived from an element mass balance approach using Ti immobility as a proxy for basalt weathering (Beerling et al., 2024). CDR rates estimated for various ERW projects assessing olivine-bearing basalt range from 0.05–17.6 t CO_2/ha/yr (Manning et al., 2013; Harrington et al., 2023; Holzer et al., 2023) or 42–77 kg CO_2/t basalt (Sissmann et al., 2014; Honvault et al., 2024). While Goll et al. (2021) proposed scaling up basalt quarrying to achieve substantial CO_2 removal, this would lead to increased CO_2 emissions; thus, an alternative strategy involves utilizing processed rock from current and past mining operations alongside basalt to meet CDR goals (Renforth et al., 2011b; Power et al., 2024).

This ERW field experiment applied kimberlite residues off-site yielding similar solubility trapping rates to the basalt distributed in Malaysia reported by Larkin et al.

(2022), although basalt dosages were considerably lower (50 t/ha). It is also important to acknowledge that the kimberlite CDR rates measured in this study were influenced by specific weathering conditions (i.e., a continental climate), which differs from the tropical climate of Malaysia and the subarctic climate at the Gahcho Kué mine. Moreover, CDR rates for other kimberlites would vary depending on their mine site environment and near-by viable lands for off-site transport, such as the farmland adjacent to the Voorspoed mine and desert surrounding the Venetia mine in South Africa, or the diverse conservation parks containing the Jwaneng and Orapa mines in Botswana. Thus, accurate measurements and monitoring of field rates using instrumentation similar to the monitoring plots in this study is recommended for an ERW deployment.

Transporting mine residues off-site raises legal concerns regarding air and water quality and may encounter push-back from local authorities (Webb, 2020). The limitations governing the relocation of mine waste for ERW in the United States were evaluated by Webb (2020) who referred to potential violations of the Clean Air Act due to particulate grain size and the Clean Water Act due to application deposition and runoff into water bodies. However, there is potential for managing the discharge of artificial silicates (e.g., mine waste) onto designated lands for a specific purpose (e.g., ERW), within waste disposal regulations. This approach could be viable provided there is sufficient buffer land between the placement of industrial wastes and nearby agricultural fields (Webb, 2020); although, basalt – a waste product from quarries – is already widely applied to croplands for ERW (Beerling et al., 2024). Still, amending existing regulations specifically for ERW is recommended. The use of rock feedstocks on croplands for agricultural benefits and CDR (Beerling et al., 2020) has outweighed consideration of

their application in industrially degraded lands, due to their substantial landcover and established infrastructure for spreading fertilizers (Power et al., 2024). Repurposing and depositing mine residues offsite, depending on the land use, would require case-specific permits with varying thresholds of acceptable cation leaching and soil impacts. Thus, the establishment of long-term monitoring stations to directly measure feedstock weathering must be incorporated into these regulations, especially given the significant influence of climate on CO_2 sequestration rates. By adhering to robust regulatory frameworks and implementing thorough monitoring protocols, mine residues and other industrial wastes can be managed responsibly and sustainably while maximizing their potential for carbon removal.

2.8 Conclusion

Effective and accurate site-specific carbon accounting methods are essential for advancing ERW as a strategy to help mitigate climate change. This study demonstrates the efficacy of shallow water sampling and soil moisture monitoring in tracking CO_2 removed through solubility trapping. Using a water budget approach and analyzing DIC in porewaters, we quantified the generation of HCO_3^- from weathering kimberlite relative to background signals. Importantly, we differentiated carbonate and silicate weathering contributions based on cation loadings. The choice of cations to track was determined through an initial reactivity assessment of the residues, identifying cations most indicative of kimberlite and soil weathering.

Challenges regarding quantification of CO_2 removal via mineral trapping particularly encompasses differentiating sources of TIC (e.g., existing carbonates vs. amendment carbonates vs. new pedogenic carbonate). Accurately representing CDR

contributions from mineral trapping relies on comprehensive understandings of soil and amendment characterization and interactions, especially when both contain carbonate minerals; however, in applications where no carbonates are applied to non-calcareous soils, mineral trapping may be more easily quantified. Given that the majority of CDR in the field experiments stemmed from carbonate weathering, improving our understanding and measurement methods for mineral trapping is imperative before scaling up ERW.

Over three years, kimberlite residues from Gahcho Kué sequestered 0.7 and 0.9 t CO_2/ha via solubility trapping at application rates of 400 and 200 t/ha, respectively. Shallow porewater samples for both amended plots exhibited clear evidence of elevated DIC and alkalinity relative to the control, with supporting ^{13}C compositions indicating that the sequestered CO_2 originated from organic sources via soil respiration. Throughout the experiment, Ni and Cr concentrations remained within safe limits in porewaters of the amended plots, while porewaters became enriched in K following amendments, validating kimberlite residues as a viable soil amendment. Long-term monitoring of these high dosages could provide valuable insights into silicate mineral dissolution efficiencies, which would be particularly beneficial for ERW projects in regions necessitating higher dosages for waste management (e.g., mine sites).

We encourage the mining industry to consider incorporating ERW of environmentally safe residues into management practices to sustain reactions between residues and CO_2 during operation and post-closure. Dispersing kimberlite residues on-site as a soil substrate for mine remediation and off-site as a soil re-mineralizer would minimize containment and land reclamation costs, while optimizing global CDR by introducing a plentiful feedstock for ERW alongside basalt.

2.9 References

Allory, V., Séré, G., and Ouvrard, S. (2022). A meta-analysis of carbon content and stocks in technosols and identification of the main governing factors. *Eur J Soil Sci* 73, 1–17. doi: 10.1111/ejss.13141

Almaraz, M., Bingham, N. L., Holzer, I. O., Geoghegan, E. K., Goertzen, H., Sohng, J., et al. (2022). Methods for determining the CO_2 removal capacity of enhanced weathering in agronomic settings. *Frontiers in Climate* 4:970429, 1–18. doi: 10.3389/fclim.2022.970429

Amann, T., and Hartmann, J. (2022). Carbon accounting for enhanced weathering. *Frontiers in Climate* 4:849948, 1–9. doi: 10.3389/fclim.2022.849948

Amann, T., Hartmann, J., Struyf, E., De Oliveira Garcia, W., Fischer, E. K., Janssens, I., et al. (2020). Enhanced Weathering and related element fluxes - A cropland mesocosm approach. *Biogeosciences* 17, 103–119. doi: 10.5194/bg-17-103-2020

Bakken, A. K., Gautneb, H., Sveistrup, T., and Myhr, & K. (2000). Crushed rocks and mine tailings applied as K fertilizers on grassland. *Nutr Cycl Agroecosyst* 56, 53–57.

Baragaño, D., Forján, R., Aguado, J. M. M., Martino, M. C., García, P. D., Rubio, J. M., et al. (2019). Reuse of dunite mining waste and subproducts for the stabilization of metal(oid)s in polluted soils. *Minerals* 9, 1–11.

Beerling, D. J., Epihov, D. Z., Kantola, I. B., Masters, M. D., Reershemius, T., Planavsky, N. J., et al. (2024). Enhanced weathering in the US Corn Belt delivers carbon removal with agronomic benefits. *Proc Natl Acad Sci U S A* 121. doi: 10.1073/pnas.2319436121

Beerling, D. J., Kantzas, E. P., Lomas, M. R., Wade, P., Eufrasio, R. M., Renforth, P., et al. (2020). Potential for large-scale CO_2 removal via enhanced rock weathering with croplands. *Nature* 583, 242–248. doi: 10.1038/s41586-020-2448-9

Beerling, D. J., Leake, J. R., Long, S. P., Scholes, J. D., Ton, J., Nelson, P. N., et al. (2018). Farming with crops and rocks to address global climate, food and soil security. *Nat Plants* 4, 138–147. doi: 10.1038/s41477-018-0108-y

Brantley, S. L., and Olsen, A. A. (2014). *Reaction kinetics of primary rock-forming minerals under ambient conditions*., eds. H. Holland and K. Turekian. Oxford: Elsevier. doi: 10.1016/B978-0-08-095975-7.00503-9

Brunauer, S., Emmett, P. H., and Teller, E. (1938). Adsorption of gases in multimolecular layers. *J Am Chem Soc* 60, 309–319.

CCME (1999). Canadian water quality guidelines for the protection of aquatic life. CCME.

Clarkson, M. O., Larkin, C. S., Swoboda, P., Reershemius, T., Suhrhoff, T. J., Maesano, C. N., et al. (2024). A review of measurement for quantification of carbon dioxide removal by enhanced weathering in soil. *Frontiers in Climate* 6, 1345224. doi: 10.3389/fclim.2024.1345224

Cross, A. T., Zhong, H., and Lambers, H. (2021). Incorporating rock in surface covers improves the establishment of native pioneer vegetation on alkaline mine tailings. *Science of the Total Environment* 768, 1–14. doi: 10.1016/j.scitotenv.2021.145373

Daval, D., Hellmann, R., Martinez, I., Gangloff, S., and Guyot, F. (2013). Lizardite serpentine dissolution kinetics as a function of pH and temperature, including effects of elevated pCO_2. *Chem Geol* 351, 245–256. doi: 10.1016/j.chemgeo.2013.05.020

De Beers Canada Inc. (2020a). Gahcho Kué Mine: Geochemical Characterization Plan Version 4.2.

De Beers Canada Inc. (2020b). Gahcho Kué Mine: Monthly Surveillance Network Program Report (MV2005L2-0015).

De Beers Canada Inc. (2023). Gahcho Kué Mine: 2021 Annual Air Quality Report.

De Beers Canada Inc. (2024). Gahcho Kué Mine: Interim Closure and Reclamation Plan.

Díaz-Piloneta, M., Ortega-Fernández, F., Terrados-Cristos, M., and Valeriano Álvarez-Cabal, J. (2022). Application of steel slag for degraded land remediation. *Land (Basel)* 11. doi: 10.3390/land11020224

Dietzen, C., and Rosing, M. T. (2023). Quantification of CO_2 uptake by enhanced weathering of silicate minerals applied to acidic soils. *International Journal of Greenhouse Gas Control* 125, 103872. doi: 10.1016/j.ijggc.2023.103872

Dubois, K. D., Lee, D., and Veizer, J. (2010). Isotopic constraints on alkalinity, dissolved organic carbon, and atmospheric carbon dioxide fluxes in the Mississippi River. *J Geophys Res* 115. doi: 10.1029/2009JG001102

Dupla, X., Möller, B., Baveye, P. C., and Grand, S. (2023). Potential accumulation of toxic trace elements in soils during enhanced rock weathering. *Eur J Soil Sci* 74, e13343. doi: 10.1111/ejss.13343

Farhang, F., Rayson, M., Brent, G., Hodgins, T., Stockenhuber, M., and Kennedy, E. (2017). Insights into the dissolution kinetics of thermally activated serpentine for CO_2 sequestration. *Chemical Engineering Journal* 330, 1174–1186. doi: 10.1016/j.cej.2017.08.073

Giuliani, A., Phillips, D., Kamenetsky, V. S., Fiorentini, M. L., Farquhar, J., and Kendrick, M. A. (2014). Stable isotope (C, O, S) compositions of volatile-rich minerals in kimberlites: A review. *Chem Geol* 374–375, 61–83. doi: 10.1016/j.chemgeo.2014.03.003

Golder Associates (2014). Gahcho Kué Project: 2013 supplemental monitoring report-water quality and sediment quality-core, reference, and raised lakes.

Goll, D. S., Ciais, P., Amann, T., Buermann, W., Chang, J., Eker, S., et al. (2021). Potential CO_2 removal from enhanced weathering by ecosystem responses to powdered rock. *Nat Geosci* 14, 545–549. doi: 10.1038/s41561-021-00798-x

Gunnarsen, K. C., Jensen, L. S., Rosing, M. T., and Dietzen, C. (2023). Greenlandic glacial rock flour improves crop yield in organic agricultural production. *Nutr Cycl Agroecosyst* 126, 51–66. doi: 10.1007/s10705-023-10274-0

Guo, F., Wang, Y., Zhu, H., Zhang, C., Sun, H., Yang, J., et al. (2023). Crop productivity and soil inorganic carbon change mediated by enhanced rock weathering in farmland: A comparative field analysis of multi-agroclimatic regions in central China. *Agric Syst* 210, 103691.

Gurney, J. J., Helmstaedt, H. H., Le Roex, A. P., Nowicki, T. E., Richardson, S. H., and Westerlund, K. J. (2005). Diamonds: crustal distribution and formation processes in time and space and an integrated deposit model. *Economic Geology*, 143–177.

Haque, F., Chiang, Y. W., and Santos, R. M. (2019a). Alkaline mineral soil amendment: A climate change “stabilization wedge”? *Energies (Basel)* 12, 2299. doi: 10.3390/en12122299

Haque, F., Chiang, Y. W., and Santos, R. M. (2020). Risk assessment of Ni, Cr, and Si release from alkaline minerals during enhanced weathering. *Open Agric* 5, 166–175. doi: 10.1515/opag-2020-0016

Haque, F., Santos, R. M., Dutta, A., Thimmanagari, M., and Chiang, Y. W. (2019b). Co-benefits of wollastonite weathering in agriculture: CO_2 sequestration and promoted plant growth. *ACS Omega* 4, 1425–1433. doi: 10.1021/acsomega.8b02477

Harrington, K. J., Hilton, R. G., and Henderson, G. M. (2023). Implications of the riverine response to enhanced weathering for CO_2 removal in the UK. *Applied Geochemistry* 152, 105643. doi: 10.1016/j.apgeochem.2023.105643

Hartmann, J., West, A. J., Renforth, P., Köhler, P., De La Rocha, C. L., Wolf-Gladrow, D. A., et al. (2013). Enhanced chemical weathering as a geoengineering strategy to reduce atmospheric carbon dioxide, supply nutrients, and mitigate ocean acidification. *Reviews of Geophysics* 51, 113–149. doi: 10.1002/rog.20004

Heřmanská, M., Voigt, M. J., Marieni, C., Declercq, J., and Oelkers, E. H. (2023). A comprehensive and consistent mineral dissolution rate database: Part II: Secondary silicate minerals. *Chem Geol* 636, 121632. doi: 10.1016/j.chemgeo.2023.121632

Hetman, C. M., Scott Smith, B. H., Paul, J. L., and Winter, F. (2004). Geology of the Gahcho Kué kimberlite pipes, NWT, Canada: Root to diatreme magmatic transition zones. *Lithos* 76, 51–74. doi: 10.1016/j.lithos.2004.03.051

Hoegh-Guldberg, O., Jacob, D., Taylor, M., Bindi, M., Brown, S., Camilloni, I., et al. (2018). *Impacts of 1.5oC of global warming on natural and human systems. In: Global warming of 1.5°C. An IPCC special report on the impacts of global warming of 1.5°C above pre-industrial levels and related global greenhouse gas emission pathways, in the context of strengthening the global response to the threat of climate change, sustainable development, and efforts to eradicate poverty.*, eds. V. Masson-Delmotte, P. Zhai, H.-O. Pörtner, D. Roberts, J. Skea, P. R. Shukla, et al.

Holzer, I. O., Nocco, M. A., and Houlton, B. Z. (2023). Direct evidence for atmospheric carbon dioxide removal via enhanced weathering in cropland soil. *Environ Res Commun* 5, 101004. doi: 10.1088/2515-7620/acfd89

Honvault, N., Tiouchichine, M. L., Sauze, J., Piel, C., Landais, D., Devidal, S., et al. (2024). Additive effects of basalt enhanced weathering and biochar co-application on carbon sequestration, soil nutrient status and plant performance in a mesocosm experiment. *Applied Geochemistry* 169, 106054. doi: 10.1016/j.apgeochem.2024.106054

Howard, D. M., and Howard, P. J. A. (1993). Relationships between CO_2 evolution moisture content and temperature for a range of soil types. *Soil Biol Biochem* 25(11), 1537–1546. doi: 10.1016/0038-0717(93)90008-Y

Jones, R., Fox, M. G., and Marsh, J. S. (2002). Trent Nature Areas: Geological history.

Kantola, I. B., Blanc-Betes, E., Masters, M. D., Chang, E., Marklein, A., Moore, C. E., et al. (2023). Improved net carbon budgets in the US Midwest through direct measured impacts of enhanced weathering. *Glob Chang Biol* 29, 7012–7028. doi: 10.1111/gcb.16903

Kjarsgaard, B. A., de Wit, M., Heaman, L. M., Pearson, D. G., Stiefenhofer, J., Janusczcak, N., et al. (2022). A review of the geology of global diamond mines and deposits. *Rev Mineral Geochem* 88, 1–117. doi: 10.2138/rmg.2022.88.01

Knapp, W. J., Stevenson, E. I., Renforth, P., Ascough, P. L., Knight, A. C. G., Bridgestock, L., et al. (2023). Quantifying CO_2 removal at enhanced weathering sites: A multiproxy approach. *Environ Sci Technol* 57, 9854–9864. doi: 10.1021/acs.est.3c03757

Komljenovic, D., Stojanovic, L., Malbasic, V., and Lukic, A. (2020). A resilience-based approach in managing the closure and abandonment of large mine tailing ponds. *Int J Min Sci Technol* 30, 737–746. doi: 10.1016/j.ijmst.2020.05.007

Larkin, C. S., Andrews, G. M., Pearce, C. R., Yeong, K. L., Beerling, D. J., Bellamy, J., et al. (2022). Quantification of CO_2 removal in a large-scale enhanced weathering field trial on an oil palm plantation in Sabah, Malaysia. *Frontiers in Climate* 4:959229, 1–20.

Lefebvre, D., Goglio, P., Williams, A., Manning, D. A. C., de Azevedo, A. C., Bergmann, M., et al. (2019). Assessing the potential of soil carbonation and enhanced weathering through Life Cycle Assessment: A case study for Sao Paulo State, Brazil. *J Clean Prod* 233, 468–481. doi: 10.1016/j.jclepro.2019.06.099

Lewis, A. L., Sarkar, B., Wade, P., Kemp, S. J., Hodson, M. E., Taylor, L. L., et al. (2021). Effects of mineralogy, chemistry and physical properties of basalts on carbon capture potential and plant-nutrient element release via enhanced weathering. *Applied Geochemistry* 132, 105023. doi: 10.1016/j.apgeochem.2021.105023

Manning, D. A. C., Baptista, J., Sanchez Limon, M., and Brandt, K. (2017). Testing the ability of plants to access potassium from framework silicate minerals. *Science of the Total Environment* 574, 476–481. doi: 10.1016/j.scitotenv.2016.09.086

Manning, D. A. C., and Renforth, P. (2013). Passive sequestration of atmospheric CO_2 through coupled plant-mineral reactions in urban soils. *Environ Sci Technol* 47, 135–141. doi: 10.1021/es301250j

Manning, D. A. C., Renforth, P., Lopez-Capel, E., Robertson, S., and Ghazireh, N. (2013). Carbonate precipitation in artificial soils produced from basaltic quarry fines and composts: An opportunity for passive carbon sequestration. *International Journal of Greenhouse Gas Control* 17, 309–317. doi: 10.1016/j.ijggc.2013.05.012

McDermott, F., Bryson, M., Magee, R., and van Acken, D. (2024). Enhanced weathering for CO_2 removal using carbonate-rich crushed returned concrete; a pilot study from SE Ireland. *Applied Geochemistry* 169, 106056. doi: 10.1016/j.apgeochem.2024.106056

McDonald, D. T. E. (2023). Predicting and monitoring drainage chemistry during mineral weathering for CO_2 sequestration. [Masters thesis, Trent University].

Mervine, E. M., Wilson, S. A., Power, I. M., Dipple, G. M., Turvey, C. C., Hamilton, J. L., et al. (2018). Potential for offsetting diamond mine carbon emissions through mineral carbonation of processed kimberlite: an assessment of De Beers mine sites in South Africa and Canada. *Mineral Petrol* 112, 755–765. doi: 10.1007/s00710-018-0589-4

Miller, V. S., and Naeth, M. A. (2017). Amendments and substrates to develop anthroposols for northern mine reclamation. *Can J Soil Sci* 97, 266–277. doi: 10.1139/cjss-2016-0145

MOE (1979). Rationale for the establishment of Ontario's provincial water quality objectives.

Mohammed, S. M. O., Brandt, K., Gray, N. D., White, M. L., and Manning, D. A. C. (2014). Comparison of silicate minerals as sources of potassium for plant nutrition in sandy soil. *Eur J Soil Sci* 65, 653–662. doi: 10.1111/ejss.12172

Mook, W. G., Bommerson, J. C., and Staverman, W. H. (1974). Carbon isotope fractionation between dissolved bicarbonate and gaseous carbon dioxide. *Earth Planet Sci Lett* 22, 169–176.

Moosdorf, N., Renforth, P., and Hartmann, J. (2014). Carbon dioxide efficiency of terrestrial enhanced weathering. *Environ Sci Technol* 48, 4809–4816. doi: 10.1021/es4052022

Oelkers, E. H., Declercq, J., Saldi, G. D., Gislason, S. R., and Schott, J. (2018). Olivine dissolution rates: A critical review. *Chem Geol* 500, 1–19. doi: 10.1016/j.chemgeo.2018.10.008

Oelkers, E. H., Gislason, S. R., and Matter, J. (2008). Mineral carbonation of CO_2. *Elements* 4, 333–337. doi: 10.2113/gselements.4.5.333

Oze, C., Fendorf, S., Bird, D. K., and Coleman, R. G. (2004). Chromium geochemistry in serpentinized ultramafic rocks and serpentine soils from the Franciscan Complex of California. *Am J Sci* 304, 67–101.

Paessler, D., Steffens, R., Hammes, J., and Smet, I. (2023). Monitoring CO_2 concentrations in soil gas: A novel MRV approach for cropland-based ERW? Available at: www.carbon-drawdown.de

Palandri, J. L., and Kharaka, Y. K. (2004). A compilation of rate parameters of water-mineral interaction kinetics for application to geochemical modeling. Denver.

Paulo, C., Power, I. M., Stubbs, A. R., Wang, B., Zeyen, N., and Wilson, S. A. (2021). Evaluating feedstocks for carbon dioxide removal by enhanced rock weathering and CO_2 mineralization. *Applied Geochemistry* 129, 104955. doi: 10.1016/j.apgeochem.2021.104955

Paulo, C., Power, I. M., Zeyen, N., Wang, B., and Wilson, S. A. (2023). Geochemical modeling of CO_2 sequestration in ultramafic mine wastes from Australia, Canada, and South Africa: Implications for carbon accounting and monitoring. *Applied Geochemistry* 152, 105630. doi: 10.1016/j.apgeochem.2023.105630

Pogge von Strandmann, P. A. E., Tooley, C., Mulders, J. J. P. A., and Renforth, P. (2022). The dissolution of olivine added to soil at 4°C: Implications for enhanced weathering in cold regions. *Frontiers in Climate* 4, 827698. doi: 10.3389/fclim.2022.827698

Pokrovsky, O. S., and Schott, J. (2000). Kinetics and mechanism of forsterite dissolution at 25°C and pH from 1 to 12. *Geochemica et Cosmochimica Acta* 64, 3313–3325.

Power, I. M., Harrison, A. L., Dipple, G. M., Wilson, S. A., Kelemen, P. B., Hitch, M., et al. (2013a). Carbon mineralization: From natural analogues to engineered systems. *Rev Mineral Geochem* 77, 305–360. doi: 10.2138/rmg.2013.77.9

Power, I. M., Paulo, C., and Rausis, K. (2024). The mining industry's role in enhanced weathering and mineralization for CO_2 removal. *Environ Sci Technol* 58, 43–53. doi: 10.1021/acs.est.3c05081

Power, I. M., Wilson, S. A., and Dipple, G. M. (2013b). Serpentinite carbonation for CO_2 sequestration. *Elements* 9, 115–121. doi: 10.2113/gselements.9.2.115

Rabenhorst, M. C., Wilding, L. P., and West, L. T. (1984). Identification of pedogenic carbonates using stable carbon isotope micro fabric analyses. *SoilGenesis,Morphology,andClassification* 48, 125–132.

Ramos, C. G., Dalmora, A. C., Kautzmann, R. M., Hower, J., Dotto, G. L., and Oliveira, L. F. S. (2021). Sustainable release of macronutrients to black oat and maize crops from organically-altered dacite rock powder. *Natural Resources Research* 30, 1941–1953. doi: 10.1007/s11053-021-09862-0

Ramos, C. G., dos Santos de Medeiros, D., Gomez, L., Oliveira, L. F. S., Schneider, I. A. H., and Kautzmann, R. M. (2020). Evaluation of soil re-mineralizer from by-product of volcanic rock mining: Experimental proof using black oats and maize crops. *Natural Resources Research* 29, 1583–1600. doi: 10.1007/s11053-019-09529-x

Reddy, K. R., Gopakumar, A., and Chetri, J. K. (2019). Critical review of applications of iron and steel slags for carbon sequestration and environmental remediation. *Rev Environ Sci Biotechnol* 18, 127–152. doi: 10.1007/s11157-018-09490-w

Reid, C., Bécaert, V., Aubertin, M., Rosenbaum, R. K., and Deschênes, L. (2009). Life cycle assessment of mine tailings management in Canada. *J Clean Prod* 17, 471–479. doi: 10.1016/j.jclepro.2008.08.014

Renforth, P., Pogge von Strandmann, P. A. E., and Henderson, G. M. (2015). The dissolution of olivine added to soil: Implications for enhanced weathering. *Applied Geochemistry* 61, 109–118. doi: 10.1016/j.apgeochem.2015.05.016

Renforth, P., Washbourne, C.-L., Taylder, J., and Manning, D. A. C. (2011). Silicate production and availability for mineral carbonation. *Environ. Sci. Technol* 45, 2035–2041. doi: 10.1021/es103241w

Ruiz, F., Safanelli, J. L., Perlatti, F., Cherubin, M. R., Demattê, J. A. M., Pellegrino Cerri, C. E., et al. (2023). Constructing soils for climate-smart mining. *Commun Earth Environ* 4, 1–6. doi: 10.1038/s43247-023-00862-x

Santini, T. C., and Banning, N. C. (2016). Alkaline tailings as novel soil forming substrates: Reframing perspectives on mining and refining wastes. *Hydrometallurgy* 164, 38–47. doi: 10.1016/j.hydromet.2016.04.011

Schuiling, R. D., and Krijgsman, P. (2006). Enhanced weathering: An effective and cheap tool to sequester CO_2. *Clim Change* 74, 349–354. doi: 10.1007/s10584-005-3485-y

Schulte, P., van Geldern, R., Freitag, H., Karim, A., Négrel, P., Petelet-Giraud, E., et al. (2011). Applications of stable water and carbon isotopes in watershed research: Weathering, carbon cycling, and water balances. *Earth Sci Rev* 109, 20–31. doi: 10.1016/j.earscirev.2011.07.003

Sissmann, O., Brunet, F., Martinez, I., Guyot, F., Verlaguet, A., Pinquier, Y., et al. (2014). Enhanced olivine carbonation within a basalt as compared to single-phase experiments: Reevaluating the potential of CO_2 mineral sequestration. *Environ Sci Technol* 48, 5512–5519. doi: 10.1021/es405508a

Smith, C. A. S., Webb, K. T., Kenney, E., Anderson, A., and Kroetsch, D. (2011). Brunisolic soils of Canada: Genesis, distribution, and classification. *Can J Soil Sci* 91, 695–717. doi: 10.4141/cjss10058

Steinour, H. H. (1959). Some effects of carbon dioxide on mortars and concrete-discussion. *Journal of American Concrete Institute* 30, 905–907.

Stubbs, A. R., Paulo, C., Power, I. M., Wang, B., Zeyen, N., and Wilson, S. A. (2022). Direct measurement of CO_2 drawdown in mine wastes and rock powders: Implications for enhanced rock weathering. *International Journal of Greenhouse Gas Control* 113, 103554. doi: 10.1016/j.ijggc.2021.103554

Sutherland, K., Matlin-Wainer, M., Holme, E., He, J., Savage, R., Marsland, E., et al. (2023). Enhanced weathering in agriculture v1.0 – Isometric. 1–148. Available at: https://registry.isometric.com/protocol/enhanced-weathering-agriculture (Accessed March 10, 2024).

Swoboda, P., Döring, T. F., and Hamer, M. (2022). Remineralizing soils? The agricultural usage of silicate rock powders: A review. *Science of the Total Environment* 807, 150976. doi: 10.1016/j.scitotenv.2021.150976

te Pas, E. E. E. M., Hagens, M., and Comans, R. N. J. (2023). Assessment of the enhanced weathering potential of different silicate minerals to improve soil quality and sequester CO_2. *Frontiers in Climate* 4, 954064. doi: 10.3389/fclim.2022.954064

UNFCCC (2015). Paris Agreement. Paris, France. Available at: https://treaties.un.org/Pages/ViewDetails.aspx?src=TREATY&mtdsg_no=XXVII-7- (Accessed April 15, 2023).

Vienne, A., Poblador, S., Portillo-Estrada, M., Hartmann, J., Ijiehon, S., Wade, P., et al. (2022). Enhanced weathering using basalt rock powder: Carbon sequestration, co-benefits

and risks in a mesocosm study with solanum tuberosum. *Frontiers in Climate* 4, 869456. doi: 10.3389/fclim.2022.869456

Wang, B., Zeyen, N., Wilson, S., Honda-McNeil, M. J., Hamilton, J. L., Von Gunten, K., et al. (2024). Migration of transition metals and potential for carbon mineralization during acid leaching of processed kimberlite from Venetia diamond mine, South Africa. *Applied Geochemistry* 166, 105986. doi: 10.1016/j.apgeochem.2024.105986

Wani, O. B., Khan, S., Shoaib, M., Zeng, H., and Bobicki, E. R. (2022). Decarbonization of mineral processing operations: Realizing the potential of carbon capture and utilization in the processing of ultramafic nickel ores. *Chemical Engineering Journal* 433, 134203. doi: 10.1016/j.cej.2021.134203

Webb, R. M. (2020). The law of enhanced weathering for carbon dioxide removal. New York.

Weiler, J., Tassinari, C. C. G., De Aquino, T. F., Bonetti, B., and Viola, V. O. (2024). Using mining waste for CO_2 sequestration: exploring opportunities through mineral carbonation, nature-based solutions, and CCUS. *Int J Min Reclam Environ* 38, 425–441. doi: 10.1080/17480930.2024.2318132

Wilson, S. A., Dipple, G. M., Power, I. M., Barker, S. L. L., Fallon, S. J., and Southam, G. (2011). Subarctic weathering of mineral wastes provides a sink for atmospheric CO_2. *Environ Sci Technol* 45, 7727–7736. doi: 10.1021/es202112y

Wilson, S. A., Harrison, A. L., Dipple, G. M., Power, I. M., Barker, S. L. L., Ulrich Mayer, K., et al. (2014). Offsetting of CO_2 emissions by air capture in mine tailings at the Mount Keith Nickel Mine, Western Australia: Rates, controls and prospects for carbon neutral mining. *International Journal of Greenhouse Gas Control* 25, 121–140. doi: 10.1016/j.ijggc.2014.04.002

Wood, C., Harrison, A. L., and Power, I. M. (2023). Impacts of dissolved phosphorus and soil-mineral-fluid interactions on CO_2 removal through enhanced weathering of wollastonite in soils. *Applied Geochemistry* 148, 105511. doi: 10.1016/j.apgeochem.2022.105511

Yu, H., Zahidi, I., and Fai, C. M. (2023). Reclaiming abandoned mine tailings ponds for agricultural use: Opportunities and challenges. *Environ Res* 232, 116336. doi: 10.1016/j.envres.2023.116336

Zeyen, N., Wang, B., Wilson, S. A., Paulo, C., Stubbs, A. R., Power, I. M., et al. (2022). Cation exchange in smectites as a new approach to mineral carbonation. *Frontiers in Climate* 4, 913632. doi: 10.3389/fclim.2022.913632

Chapter 3
Enhanced weathering of olivine powder applied to calcareous soils in Southern Ontario, Canada

3.1 Introduction

CO_2 removal (CDR) by means of silicate weathering was initially proposed nearly 40 years ago by Seifritz (1990) with studies soon after introducing CO_2 sequestration by mineral carbonation of olivine to form Mg-carbonate minerals [e.g., magnesite ($MgCO_3$); Eq. 1; Lackner et al., 1995]. Schuiling and Krijgsman (2006) established the geochemical significance of olivine [$(Mg,Fe)_2SiO_4$] for enhanced rock weathering (ERW) where CO_2 could be trapped as an aqueous phase (e.g., HCO_3^-; Eq. 2). Among the few widely established ERW feedstocks (e.g., basalt and dunite; Vink et al., 2022; Paessler et al., 2023), the olivine Mg-endmember forsterite (Mg_2SiO_4) is often present in significant quantities (Strefler et al., 2018; Amann and Hartmann, 2019; Lewis et al., 2021).

$$Forsterite\ carbonation: Mg_2SiO_4 + 2CO_2 \rightarrow 2MgCO_3 + SiO_2 \quad (1)$$

$$Forsterite\ weathering: Mg_2SiO_4 + 4H_2O + 4CO_2 \rightarrow 2Mg^{2+} + 4HCO_3^- + H_4SiO_4 \quad (2)$$

The prevalence of forsterite in ultramafic deposits, coupled with its relatively fast weathering rates and high capacity for carbon removal, has made it a desirable mineral for CDR applications (Hartmann et al., 2013; Oelkers et al., 2018). A primary challenge for upscaling ERW applications is accurately detecting CDR signals above background interferences, especially when most applications may feature agricultural regulated dosages (e.g., 1–20 t/ha; Swoboda et al., 2022). Natural soils are characterized by a porous, heterogenous texture, varying fluid retention (e.g., preferential flow paths), less favourable dissolution kinetics (e.g., ambient temperature and non-acidic pH values), and influences from biological factors (Calabrese et al., 2022), whereas most ERW studies are

conducted in a laboratory under simplified, controlled conditions (e.g., high temperature and low pH). Although improving the precision of CDR quantification is necessary for unfavourable application sites (e.g., highly weatherable soil or temperate climates), reliable CDR assessments may simply be achieved by monitoring higher application rates of amendments. However, monitoring metal accumulation, such as Ni and Cr, from olivine-rich rocks must be considered when selecting methodologies for measuring CDR rates (Dupla et al., 2023).

CDR quantification in olivine weathering applications include surface CO_2 drawdown (Stubbs et al., 2022), cation mass balances in soils and waters as proxies for mineral weathering (Dietzen and Rosing, 2023; Kantola et al., 2023), and direct monitoring of solid and aqueous inorganic carbon generation to track carbon in its various phases (Holzer et al., 2023; Knapp et al., 2023). Although direct gaseous CO_2 flux measurements provide valuable insights on mineral CDR efficacy, they are often dominated by soil respiration in natural environments (Görres et al., 2016). Consequently, cation mass balances and carbon phase measurements are more commonly used in ERW studies such as in column or pot experiments (ten Berge et al., 2012; Renforth et al., 2015; Amann et al., 2020; Pogge von Strandmann et al., 2022; te Pas et al., 2023) and in the few multi-year field trials consisting of soils amended with olivine-bearing rocks (McDermott et al., 2019; Maxbauer and Yambing, 2022; Guo et al., 2023). However, the small CDR signals can be obscured by the substantial background noise in natural soils (Calabrese et al., 2022). To address this limitation, stoichiometric mineral reactions with CO_2 have been used to estimate carbon capture based on the measured weathering products (e.g., Mg; Dietzen and Rosing, 2023; Iff et al., 2024)). As this approach does not

consider the fate of the numerous carbon phases, it only offers an upper estimate of CDR (Clarkson et al., 2024).

This study used the CDR quantification methods of Chapter 2, assessing a mineral powder that has a simple composition that will result in solubility trapping of CO_2 without substantial mineral trapping. The goals of this research were to (1) predict base cation and potentially toxic metal (e.g., Ni and Cr) release from powdered olivine (2) determine the CDR rate of powdered olivine applied to calcareous soils in Southern Ontario, Canada using porewater chemical data, (3) simulate olivine weathering using a geochemical model with real-world input data, and (4) make recommendations to improve CDR quantification in ERW applications based on the findings of this study. In addition to detailed characterization of the olivine powder, batch leaching experiments were conducted to assess its initial reactivity and predict the release of cations, distinct from the background weathering of the soil. Pulverized olivine was applied to square-metre field plots in Peterborough, Ontario, Canada, at dosages of 10 and 20 kg and monitored for 2 yr. The results of this study will contribute to the understanding of olivine weathering in alkaline soils and support applications of aqueous phase measurements for carbon accounting, while evaluating the safety of applying ultramafic minerals in high dosages to the environment.

3.2 Methods

3.2.1 Material characterization and preparation

The olivine amendment was purchased as a sand from OCL Industrial Materials Ltd with an initial specific surface area (SSA) of 0.24 m^2/g. A total of ~30 kg of olivine

sand was pulverized using a FLSmidth Essa® LM2 Pulverizing Mill in 250 g aliquots for 1.5 min using 400 cc ring and roller pulverizer bowls.

The pulverized olivine was analyzed for specific surface area by the Brunauer-Emmett-Teller (BET) method, total inorganic carbon (TIC) by coulometry, particle size distribution (PSD) by laser diffraction, cation exchange capacity (CEC) by ICP-OES of ammonium acetate leachates, bulk geochemical composition by X-ray fluorescence (XRF) spectroscopy, and mineralogical composition by X-ray diffraction (XRD). Detailed methods are provided in Appendix A. Soil profile characterization for the field weathering site is provided in Chapter 2, with bulk samples of field soils used in the batch leaches.

3.2.2 Batch leaches with CO_2

Pulverized olivine was mixed with field soils to achieve a total mass of 5.0 g, with varying olivine concentrations (0, 0.5, 1, 5, 10, 25, 50, and 100 wt.%), denoted in the results as Soil100, 0.5Ol, 1Ol, 5Ol, 10Ol, 25Ol, 50Ol, and 100Ol, respectively. Aliquots of these mixtures (2.5 g) were micronized prior to XRF spectroscopy.

The batch leach methodology consisted of combining 250.0 mg aliquots of the soil-olivine mixtures (adding 15 wt.% and 75 wt.% olivine mixtures denoted 15Ol and 75Ol) with 100 mL of deionized water (18.2 MΩ·cm) in uncapped polyethylene flasks. After two weeks of agitation on a shaker table (150 rpm) inside a CO_2 incubator (35°C, 10% CO_2, 21.9% O_2) at nearly 100% relative humidity, leachates were filtered (0.22 μm) into 50 mL plastic centrifuge tubes and acidified (2% v/v ultrapure HNO_3, Aristar ®, UK) for ICP-MS analysis. Detailed methods are provided in Chapter 2.

3.2.3 ERW field experiments

In May 2022, at Trent University (Peterborough, Ontario, Canada), three circular plots (1 m^2) separated by 2 m were cleared of vegetation, composed entirely of *Anthoxanthum hirtum* (Sweetgrass), and lightly tilled to loosen the circumneutral soils for mixing the olivine powder (Fig. 3.1). Each plot was equipped with a TEROS12 moisture probe and surface porewater sampler at depths of 15 and 30 cm, a soil gas sampler, and a polyvinyl chloride (PVC) collar for measuring CO_2 surface flux. Installation of each monitoring piece involved backfilling each hole with a slurry of soil and deionized water in approximately equal parts (Fig. 3.2). Detailed methods for setting up the field experiment are provided in Chapter 2.

The experiment included one control plot with existing Brunisol-class soil and two plots amended with 10 and 20 kg of pulverized olivine, denoted Ol10 and Ol20, respectively (Fig. 3.1). The plots were monitored over two periods, the first from May 2022 to December 2022, and the second from January 2023 to November 2023. Water sampling during winter months depended on snowmelt, and CO_2 flux measurements were paused entirely from October to mid-March. A detailed climate description is available in Chapter 2.

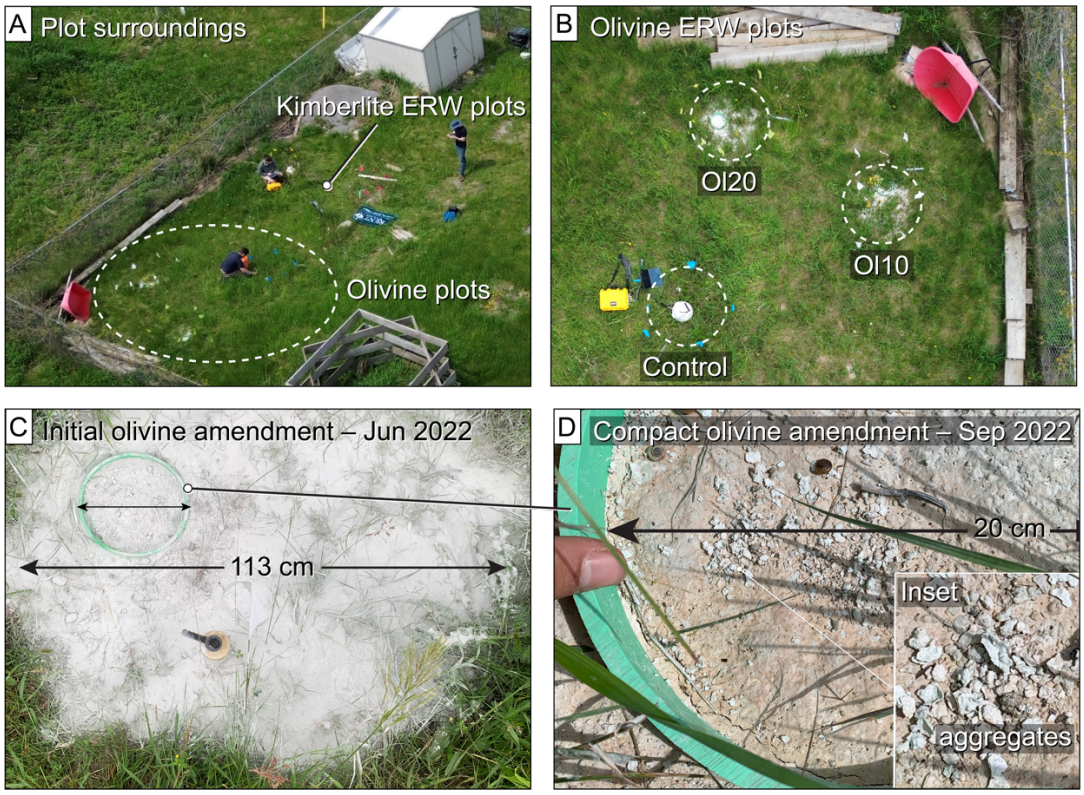

Figure 3.1. Outdoor experimental location at Trent University, Peterborough, Ontario, Canada (A). Orientation of the three square-metre plots, with two different application rates of pulverized olivine (Ol10: 100 t/ha; Ol20: 200 t/ha) and a control (B). Initial olivine amendment loosely applied to a square-metre plot (C). Natural compaction and aggregation of the pulverized olivine 3 months after amendment inside a 20 cm diameter PVC collar used for CO_2 flux measurements (D).

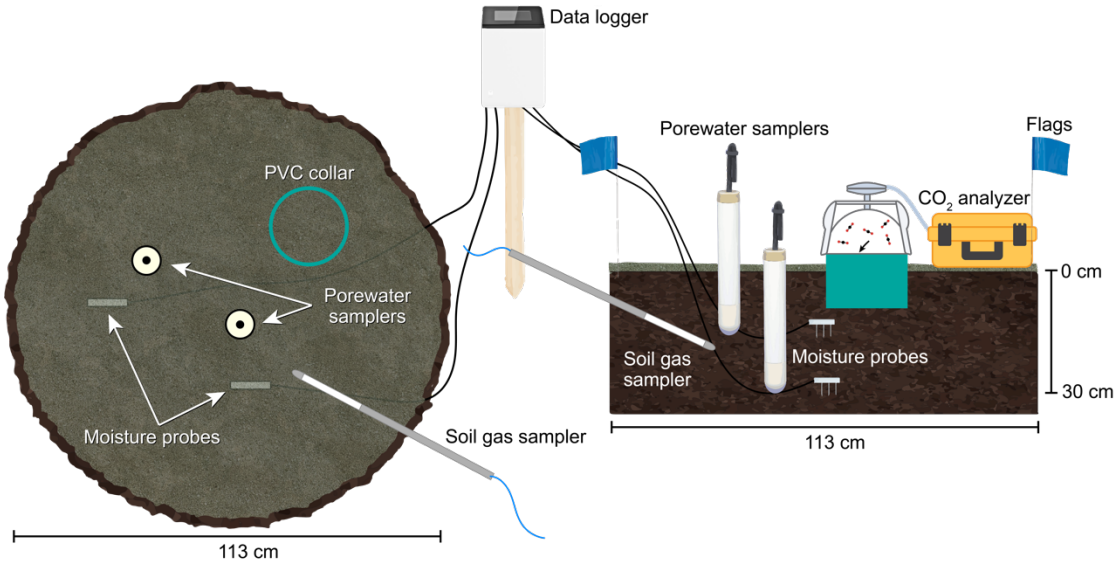

Figure 3.2. Experimental setup for field plots that were equipped with porewater samplers at 15 and 30 cm depths and a soil gas sampler at 20 cm depth. TEROS 12 moisture probes were installed at 15 and 30 cm depths, recording data onto a ZL6 data logger located outside of the plot. A 20 cm diameter PVC collar with a 2 cm offset was used for CO_2 flux measurements using a LI-COR survey chamber and LI-8100A CO_2 analyzer.

3.2.3.1 Field sampling

Porewater samplers were pumped weekly, or following a precipitation event, for opportunistic sample collection with all samples analyzed for pH and dissolved inorganic carbon (DIC). Half of the collected water samples were analyzed for alkalinity and major and trace elements via ICP-MS, and only select waters were analyzed for anions (n=8–9 of ~60 total samples collected per plot). Detailed porewater sampling procedures, sample analysis, and sample storage procedure are provided in Chapter 2.

Soil cores (20–25 cm depth) were collected in triplicate from each plot in December 2022 and March 2024, at which each monitoring period had concluded, and the ground had thawed. Each core was segmented into 2.5 cm increments for the surface

profile (0–5 cm) and 5 cm for the lower profile (5–25 cm). Following one-week of air drying in a fume hood, soils were homogenized and sieved (2 mm) prior to storage. Micronized (~2 g) samples underwent TIC analysis with aliquots of ~100 mg each. Detailed methodologies are provided in Appendix A and Chapter 2. The bulk density of the soil weatherable fraction was determined by water displacement of an undisturbed soil core, with the >2 mm and organic matter (LOI_{550^oC}) mass fraction subtracted from the total soil mass. These soil data are the same reported in Chapter 2 in Table 2.1.

The LI-8100 Soil CO_2 flux system, equipped with a survey chamber (LI-COR, Lincoln, Nebraska, USA), was utilized to measure instantaneous CO_2 fluxes in each plot over a ~120 s interval. CO_2 fluxes were measured daily for one week immediately following olivine amendment, and once weekly throughout each monitoring period. The instrument was programmed to measure the diffusion rate of CO_2 ($\mu mol/m^2/s$) over 2 min, coupled with a 10 s pre-purge of the chamber before measuring and 10 s post-purge between plot measurements. Further details on CO_2 flux and pore gas measurement details are provided in Chapter 2.

3.2.4 Simulation of weathering rates with PROFILE

Release rates of cations via soil mineral and olivine weathering were estimated using the PROFILE v4.0 model (Sverdrup and Warfvinge, 1992). PROFILE is a steady-state geochemical model that simulates the chemical compositions of soil solutions, allowing comparisons with weathering rates derived from field measurements. The model considers weathering of each horizon requiring empirical data for individual layers to define the physical and chemical environment and applies kinetic rate equations

determined from laboratory experimentation and theoretical analyses (Sverdrup and Warfvinge, 1993). PROFILE calculates annual cation release rates (e.g., Ca, Mg, K, Na, Al, Si, PO_4) based on the weathering of silicate minerals, considering transition state theory where reactive sites on minerals are near or reach equilibrium with aqueous reactants (e.g., H^+, H_2O, OH^-, CO_2, and organic acids), with further decomposition of these sites considered rate-limiting (Sverdrup and Warfvinge, 1993; Sverdrup et al., 2019).

The baseline control plot in this study consisted of a single 30 cm soil layer containing the A and B horizons which are visually and physically indifferent in a Brunisol profile. Amended plots consisted of two layers including an upper 2 cm layer of olivine atop a second soil layer similar to the control. Precipitation chemistry (e.g., acidic particulates deposited via precipitation) were recorded at the Canadian Air and Precipitation Monitoring Network (CAPMoN) station operated by Environment and Climate Change Canada (ECCC) in Warsaw, Ontario, the nearest CAPMoN site to the study area (~20 km; Table 3.1). The average temperature of Peterborough, Ontario (6.2ºC), does not reflect the extreme temperatures that characterize a continental climate; therefore, PROFILE runs were divided into warmer (April–October, inclusive) and colder (November–March, inclusive) temperature months where average daily temperatures were >5ºC and <5ºC, respectively. The average daily temperature for the warmer months was 14.5ºC with an average maximum of 20ºC and minimum of 8.6ºC, while the colder months exhibited a daily average of -3.6ºC with average maximum and minimum temperatures of 0.1ºC and -8.0ºC, respectively. These data were retrieved from the 1981–2010 climate normals provided by ECCC.

Key input parameters for the model include mineralogy, soil moisture, surface areas, and bulk density for each layer. Mineralogy data from XRD analyses informed the PROFILE model of layer mineral composition, facilitating the calculation of dissolution rates for soil and olivine minerals categorized by their mineral class (Table 3.2; Phelan et al., 2014). The model assumes residual mineralogy up to 100 wt.% as quartz. Other inputs included annual averages of soil moisture content from moisture probes, percentages of infiltrating precipitation and percolation (termed precipitation surplus) from the water budget used to calculate CO_2 removal rates (Appendix B), and specific surface area determined using the BET method (detailed methodology provided in Appendix A). Precipitation surplus consists of the percentage of soil water percolating out of the bottom layer, thus it is equivalent to the annual percolation values (~200 mm) calculated using the water budget, relative to the total annual rainfall in Peterborough, ON (~800 mm; Appendix B). The partial pressure of CO_2 was measured using a soil gas lance positioned at 20 cm, yielding an average CO_2 value of ~1.5%, the maximum value applicable for PROFILE (35× atmospheric). Surface layer partial pressures were assumed to be in equilibrium with atmospheric CO_2 (1× atmospheric). A fixed concentration of 5 mg/L for dissolved organic carbon (DOC) was used across all solutions to reflect typical values associated with the depth of percolation (20–50 cm; Phelan et al., 2014). Further, adjustments (sensitivity testing) to DOC (e.g., 1, 10, 100 mg/L) did not significantly affect cation release rates. Inputs for the control, Ol10, and Ol20 run are outlined in Table 3.3. Since the plots were cleared of vegetation at the start of the experiment, inputs related to vegetation uptake were excluded from the model simulations.

Table 3.1. Annual atmospheric deposition input data consistent among all PROFILE runs. Temperature is reported as the average ºC for the warmer (colder) months, with standard deviations accounting for daily maximum and minimum air temperatures.

	Peterborough, Ontario Canada
Temperature (ºC)	14.5 ±5.7 (-3.6 ±4.1)
Precipitation (m/yr)	0.8
Wet-only Despoition (keq/ha/yr)	
SO_4	0.12
Cl	0.05
NO_3	0.22
NH_4	0.25
Ca	0.19
Mg	0.03
K	0.01
Na	0.04

Table 3.2. Mineralogy inputs (wt.%) for the control, Ol10, and Ol20 plot.

	Soil layer	Olivine layer
K-feldspar	23.4	
Albite	23.4	
Hornblende	6.5	1.2
Pyroxene		6.2
Olivine		89.4
Chlorite		3.2
Calcite	16.1	

Minerals included under each PROFILE mineral class include K-feldspar– microcline, Hornblende– lizardite, pargasitic hornblende, Pyroxene– enstatite, Chlorite– clinochlore

Table 3.3. PROFILE layer inputs for the control, Ol10, and Ol20 plot.

	Control	Ol10	Ol20
Layer 1 depth	*0.3 m*	*0.02 m*	*0.04 m*
Soil water content (m^3/m^3)	0.22	0.25	0.23
Bulk density (kg/m^3)	1080	500	500
Surface area (m^2/m^3)	3.7×10^6	8.2×10^5	8.2×10^5
CO_2 pressure (×atm)	35	1	1
Precip entering layer (%)	100	100	100
Precip surplus (%)	25	100	100
DOC (mg/L)	5	0	0
Apparent $logK_{gibbsite}$	8.5	9.5	9.5
Layer 2 depth	-	*0.3 m*	*0.3 m*
Soil water content (m^3/m^3)	-	0.23	0.23
Bulk density (kg/m^3)	-	1080	1080
Surface area (m^2/m^3)	-	3.7×10^6	3.7×10^6
CO_2 pressure (×atm)	-	35	35
Precip entering layer (%)	-	100	100
Precip surplus (%)	-	25	25
DOC (mg/L)	-	5	5
Apparent $logK_{gibbsite}$	-	8.5	8.5

3.3 Results

3.3.1 Olivine characterization and batch leaches

The olivine powder had a median particle size of 28.5 μm with a specific surface area of 1.64 m^2/g, which is about half that of the sandy loam soils (3.4 m^2/g). Total CEC of the field soil exceeded that of the olivine powder by ~20× (Table 3.4). Compositionally, the olivine powder was mainly composed of forsterite (89.4 wt.%), with minor abundances of enstatite (6.2 wt.%), clinochlore (3.2 wt.%), and lizardite (1.2 wt.%; Table 3.4). It exhibited high amounts of MgO (49.7 wt.%) and SiO_2 (41.6 wt.%; Table 3.5), leaching 7.4 g Mg/kg and 4.5 g Si/kg, respectively, which were 19× and 9× greater than those leached from the soil. Conversely, the powdered olivine contained a minimal amount of CaO (0.15 wt.%; Table 3.5), resulting in low leaching of Ca (~0.05 g/kg; Table 3.6) compared to the calcareous soil (37.9 g/kg; Table 3.6). Additionally, the

olivine powder contained 7.4 wt.% Fe_2O_3; all other remaining oxides were present at <1 wt.% (Table 3.5).

Table 3.4. Physical, geochemical, and mineralogical characteristics of pulverized olivine and circumneutral pH field soils (n=3).

	Olivine powder	**Soil**
SSA (m^2/g)	1.64	3.4
TIC (%)	0.03	1.9
D80 (µm)	141 ± 7.4	166–339
Total CEC (cmol/kg)	0.53 ± 0.02	11.7 ± 3.3
Ni (mg/kg)	2276	16
Cr (mg/kg)	695	34
Mineralogy		
Ca- and Mg-bearing silicate phases	Fo (89.4 wt.%), En (6.2 wt.%), Clc (3.2 wt.%), Lz (1.2 wt.%)	Prg (6.5 wt.%)
Carbonates	-	Cal (16.1 wt.%)
Non-Ca, Mg-bearing phases	-	Qtz (30.7 wt.%), Ab (23.4 wt.%), Mc (23.4 wt.%)

Minerals identified include Fo– forsterite, Lz– lizardite, En– enstatite, Clc– clinochlore, Prg– pargasite, Cal– calcite, Qtz– quartz, Ab– albite, Mc– microcline.

Table 3.5. Geochemical compositions of local soils and pulverized olivine (n=2) given as weight percentages.

	Al_2O_3	**CaO**	**Cr_2O_3**	**Fe_2O_3**	**K_2O**	**MgO**	**Mn_3O_4**	**Na_2O**	**P_2O_5**	**SiO_2**	**TiO_2**	**V_2O_5**	**$LOI_{1000°C}$**
Soil	10.8	9.07	0.01	4.08	2.14	1.45	0.12	1.94	0.26	53.9	0.55	0.01	15.4
Olivine	0.42	0.15	0.24	7.37	0.02	49.7	0.11	0.05	<0.01	41.6	0.02	<0.01	0.99

Table 3.6. Initial element concentrations (g/kg) of solids and element concentrations leached from the initial material (g/kg) into solution after two weeks in a CO_2 incubator. Labels indicate the percentage of olivine powder (e.g., 25Ol = 25% olivine, 75% soil).

Proportion of olivine powder	Initial concentration (g/kg)					Leached from solids (g/kg)				
	Ca	Mg	Si	Ni	Cr	Ca	Mg	Si	Ni	Cr
Soil100	61.3	8.1	251.9	0.02	0.05	37.9	0.4	0.5	0.0001	0.00005
0.5Ol	61.2	9.8	250.0	0.08	0.07	37.3	0.5	0.5	0.0004	0.00007
1Ol	59.6	11	251.2	0.05	0.06	36.8	0.7	0.5	0.0004	0.00006
5Ol	57.9	22.2	248.3	0.16	0.09	38.5	1.3	1.0	0.001	0.0002
10Ol	56.9	37.3	244.7	0.29	0.12	34.5	1.5	1.2	0.001	0.0001
25Ol	46.5	79.1	237.4	0.68	0.30	28.7	2.6	1.9	0.003	0.0003
50Ol	30.8	153.7	223.0	1.33	0.40	20.9	3.7	2.7	0.008	0.0004
100Ol	1.05	296.4	194.4	2.65	0.78	0.05	7.4	4.5	0.06	<DL
DI Blank (mg/L)						0.04	0.008	0.2	<DL	0.0001

Concern regarding the release of Ni and Cr from the olivine powder primarily stemmed from the characteristically elevated concentrations of mafic minerals compared to levels found in the existing soils (Ni: 16 mg/kg, Cr: 34 mg/kg; Table 3.4). As the proportion of olivine in the solid mixtures increased, so did the concentrations of Ni and Cr. Notably, only Ni concentrations in the leachates exhibited a positive correlation with olivine content, releasing 58.3 mg Ni/kg into the 100Ol leachate (Fig. 3.3). In contrast, the 0Ol sample, consisting solely of soil, released only 0.04 mg Ni/kg into solution. Concentrations of Cr in the leachates of both the Soil100 (0.15 µg/L) and 100Ol samples (<DL) were within instrument margin of error and comparable to the concentration of the blank DI water flask (0.1 µg/L). However, the 50Ol leachate exhibited the greatest amount of Cr released within an acceptable range from instrument error (1.0 µg/L).

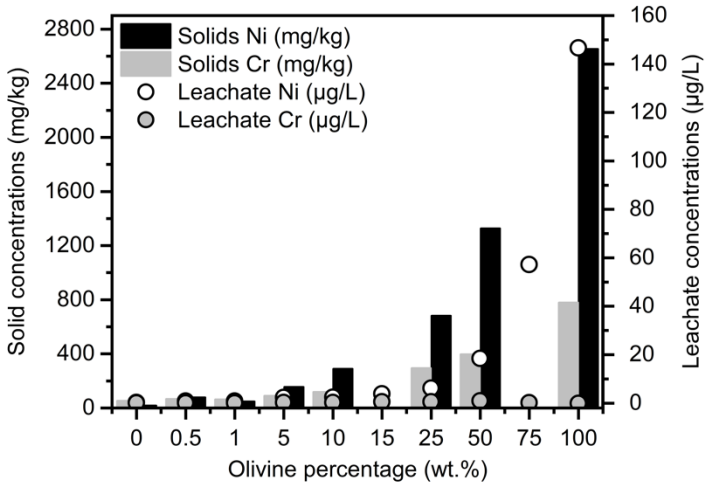

Figure 3.3. Concentrations of Ni and chromium Cr from the batch leachates (µg/L) are represented by circles. The amount of each element in the solid soil-olivine mixtures (mg/kg) is represented by bars on the secondary Y-axis. 15Ol and 75Ol were not analyzed by XRF and were only included in the batch leaching experiment.

Principal component analysis (PCA) was used to identify the influence of olivine and soil on elemental concentrations during the leach test. Analysis of the leachate data suggests that the first principal component (PC1) is positively correlated with soil content and negatively correlated with olivine abundance (Fig. 3.4). This suggests that PC1 predominantly reflects the influence of the soil matrix. Elements K, Na, B, Cu, P, U, Ca, Sr, V, Ti, Al, Fe, and Cr were distributed in olivine-poor leachates (<50% Ol; Fig. 3.4), while elements Si, Mg, Mn, Co, Ni, and Ba were correlated with negative loading scores identifying olivine-rich leachates (≥50% Ol; Fig. 3.4). The second principal component (PC2) shows a strong positive correlation with K, a strong negative correlation with Cr, a weak negative relationship with alloy group elements (Ti, Al, Fe), and weaker negative correlations with Mg and Si (Fig. 3.4). PC1 and PC2 represent 62.7% and 17.8% of the variance, respectively, collectively explaining 80.5% of the variance within the 10 samples analyzed.

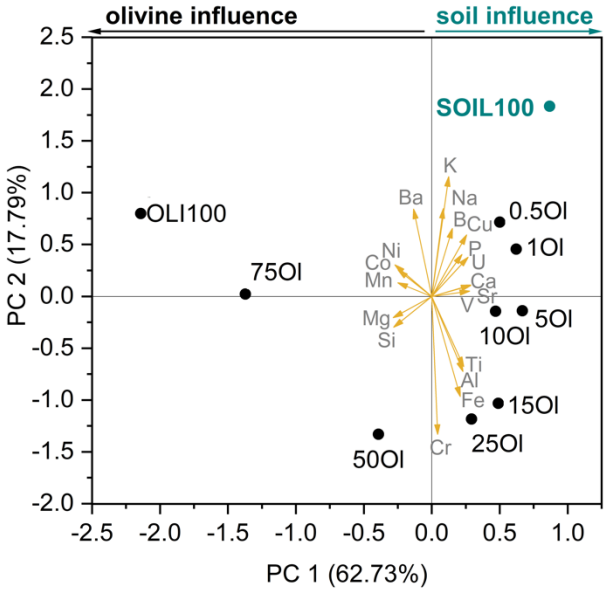

Figure 3.4. Principal component analysis (PCA) biplot showing the multivariance in 10 leached soil-olivine mixtures in terms of element variables. Vectors illustrate the direction and overall variable influence strength. PC1 correlates to the influence of olivine (negative values) and soil (positive values). Labels indicate the percentage of olivine (e.g., 25Ol = 25% olivine, 75% soil).

3.3.2 Field experiment

The olivine field plots were monitored for two consecutive periods: (1) from May 2022 to December 2022, and (2) from January 2023 to November 2023. During these periods, surface CO_2 fluxes, soil porewater chemistry, and TIC measurements with depth were monitored to assess and calculate CDR rates.

3.3.2.1 CO_2 fluxes

CO_2 fluxes in the amended plots consistently showed less positive values compared to the control baseline average of 11.6 kg $CO_2/m^2/yr$, ranging 5.1–18.4 kg $CO_2/m^2/yr$ (Fig. 3.5A). Prior to amendment in May 2022, CO_2 flux variability between plots was assessed. The average flux in the unamended Ol10 and Ol20 plots were 9.2 and 5.6 kg $CO_2/m^2/yr$, respectively, which promptly decreased to negative values of -5.2 and -9.7 kg $CO_2/m^2/yr$ upon olivine application (Fig. 3.5B, C). In the hour following amendment, Ol10 CO_2 fluxes returned to positive values (3.1 kg $CO_2/m^2/yr$), while Ol20 remained negative -5.4 kg $CO_2/m^2/yr$ (Fig. 3.5B, C). The following day, Ol20 returned to positive values (6.3 kg $CO_2/m^2/yr$). Throughout the remainder of the experiment, the amended plots exhibited consistently less positive CO_2 emissions than the control, with ranges of 5.0–14.6 for the Ol10 plot and 2.0–10.9 $kg/m^2/yr$ for the Ol20 plot (Fig. 3.5B, C).

Fluxes showed a positive correlation with soil temperature, increasing during the summer months and approaching net-zero levels during the winter months (Fig. 3.5). The snow cover season was left unmonitored.

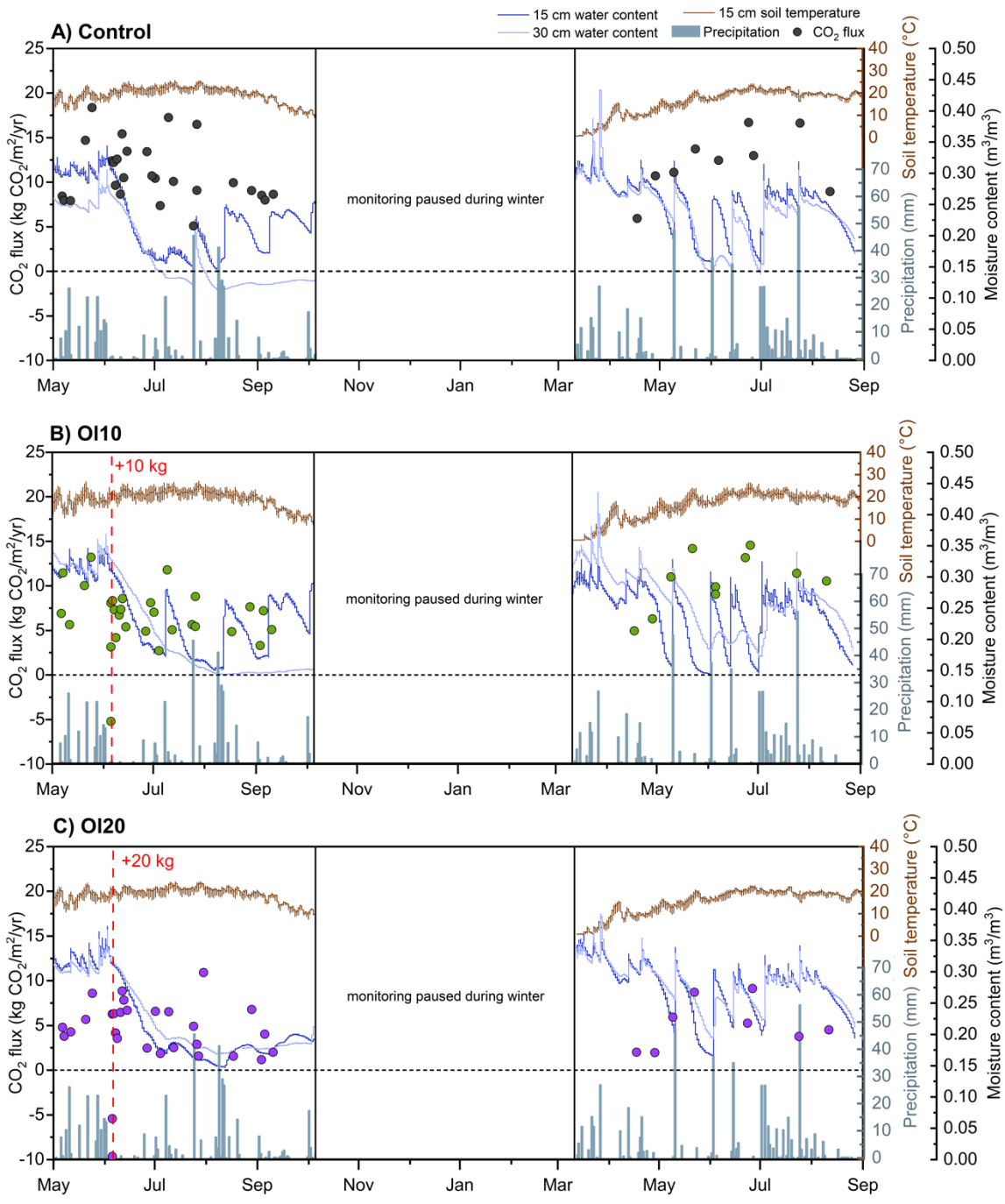

Figure 3.5. CO_2 fluxes (kg $CO_2/m^2/yr$; solid circles) for the control, Ol10, and Ol20 plots. Volumetric water contents (m^3/m^3) from moisture probes at 15 and 30 cm depths are plotted as dark blue and light blue lines, respectively, while 15 cm soil temperature (ºC) is represented as a brown line. Daily precipitation (mm) is illustrated as light blue bars. Olivine dosages of 10 and 20 kg/m^2 were added on June 15, 2022, as denoted by the vertical red dashed lines.

3.3.2.2 Soil porewater chemistry

Alkalinity and DIC were only significantly ($p < 0.05$) increased at deeper depths (30 cm) in the Ol10 plot during the first weathering period (Fig. 3.6A, B). In the first monitoring period, the control plot averaged 51.9 ±8 mg C/L for alkalinity and 44.7 ±12 mg C/L for DIC at 15 cm, and 52.3 ±7 mg C/L for alkalinity and 51.5 ±10 mg C/L for DIC at 30 cm, with a pH of 7.8 at 15 cm and 7.7 at 30 cm (Fig. 3.6). In response to a 10 kg dose of powdered olivine relative to the control, alkalinity in the 30 cm porewater increased to an average of 65.3 ±9 mg C/L ($p < 0.05$), surpassing the 95th percentile, while DIC increased to the upper quartile range just outside the 95th percentile (averaging 61.9 ±9 mg C/L; $p < 0.05$), and pH insignificantly ($p > 0.05$) decreased to 7.6 within the lower quartile (Fig. 3.6). In the Ol10 plot at 15 cm and in all depths of the Ol20 plot, average values of all parameters remained within the 25th–75th percentile range of the control.

During the second monitoring period, alkalinity and DIC of porewaters at 15 cm were within the control range of 68.4 ±12 mg C/L and 57.3 ±12 mg C/L, respectively, although DIC of Ol20 porewaters were within the upper quartile with maximum values exceeding the 95th percentile (Fig. 3.6A, B). At 30 cm depth, average alkalinity and DIC of Ol10 (72.7 ±11 mg C/L and 69.0 ±16 mg C/L) and Ol20 (81.5 ±8 mg C/L and 70.4 ±14 mg C/L) porewaters were within or above the 95th percentile of the control, respectively (Fig. 3.6A, B), although not significantly ($p > 0.05$). Overall, alkalinity values correlated closely with DIC concentrations, showing a maximum variance of ~20%, confirming that DIC is the primary contributor to alkalinity. Deeper porewaters of the amended plots and shallow porewaters in the Ol20 plot exhibited pH values within

the 25th–75th percentile of the control, whereas pH in shallow porewaters of the Ol10 plot (7.8) were below the 5th percentile of the control (Fig. 3.6C).

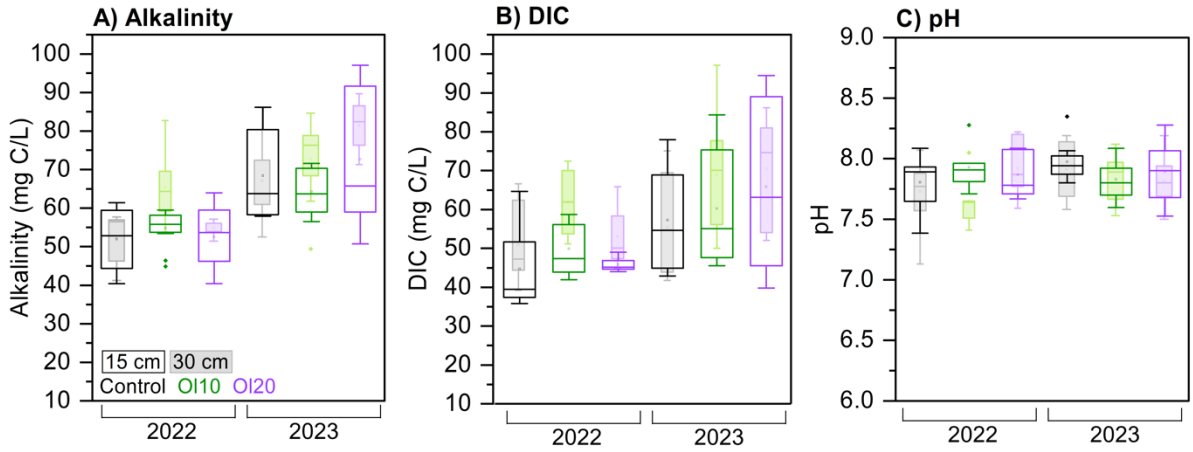

Figure 3.6. Alkalinity (A), DIC (B), and pH (C) at 15 (open box) and 30 cm (shaded) depths in the control, Ol10, and Ol20 plot over two monitoring periods. The rectangular box represents 25th–75th percentile range, the horizontal line inside the box is the median, the hollow square inside the box the mean, and the vertical lines outside the box are lower (5th percentile) and upper (95th percentile) whiskers. Outliers are shown as solid diamonds.

Elements influenced by olivine (e.g., Mg, Si, and Ni), as identified through PCA of batch leach data, showed increased concentrations only in the amended plots relative to the control during the second monitoring period. Weathering of Mg-silicates likely contributed to elevated Mg and Si concentrations in the amended plots, with concentrations during the first monitoring period remaining within the control range (1.0–3.3 mg/L and 2.4–5.6 mg/L at 15 cm, 1.7–3.0 mg/L and 2.7–8.4 mg/L at 30 cm; Fig. 3.7A, B). In the Ol20 plot, Mg and Si concentrations ranged from 1.0–6.4 mg/L and 2.5–7.9 mg/L at 15 cm depth, and from 1.0–4.2 mg/L and 1.8–5.8 mg/L at 30 cm depth, respectively, peaking in the summer months of the second monitoring period at 15 cm depths (Fig. 3.7A, B). The Ol10 exhibited Mg and Si ranges of 0.9–3.6 mg/L and 2.6–6.9

mg/L at 15 cm, and 1.6–2.9 mg/L and 2.0–8.5 mg/L at 30 cm, respectively, with notable increases in Si concentrations at 30 cm (Fig. 3.7A, B). Ni concentrations remained <3 µg/L in all plots, with concentrations in the amended plots generally within the control range of 0.4–1.7 µg/L (Fig. 3.7F). Exceedances of control Ni concentrations were observed briefly at the end of the first monitoring period in shallow depths of the Ol10 plot (~2.2 µg/L), and again at the end of the second monitoring period in the deeper Ol10 porewaters (~2.6 µg/L) and shallow Ol20 porewaters (~2.2 µg/L; Fig. 3.7F).

All porewaters were dominated by Ca with concentrations ranging from 41.1–132.0 mg/L in the control, 47.7–158.3 mg/L in Ol10, and 39.3–172.0 mg/L in Ol20 (Fig. 3.7C). Deeper porewaters exhibited increased Ca concentrations following olivine amendment, but all other measurements remained within the control range. The soil-influenced metal, Cr, released in the olivine plots, remained within the control range of 0.05–0.8 µg/L (Fig. 3.7G). Elements Na and K, weakly influenced by soil weathering and strongly correlated with each other according to PCA (Fig. 3.4), showed increases from the control average (1.7 mg/L for Na and 1.8 mg/L for K) in the amended plots (Fig. 3.7D, E). Shallow porewaters in the Ol20 plots particularly increased in Na concentrations during the second monitoring period to a maximum of 2.9 mg/L (Fig. 3.7D). K concentrations peaked in the Ol10 plot at ~5 mg/L and the Ol20 plot at ~6 mg/L; however, for most of the experiment, concentrations in the amended plots were within the control average range of 0.3–4.4 mg/L (Fig. 3.7E).

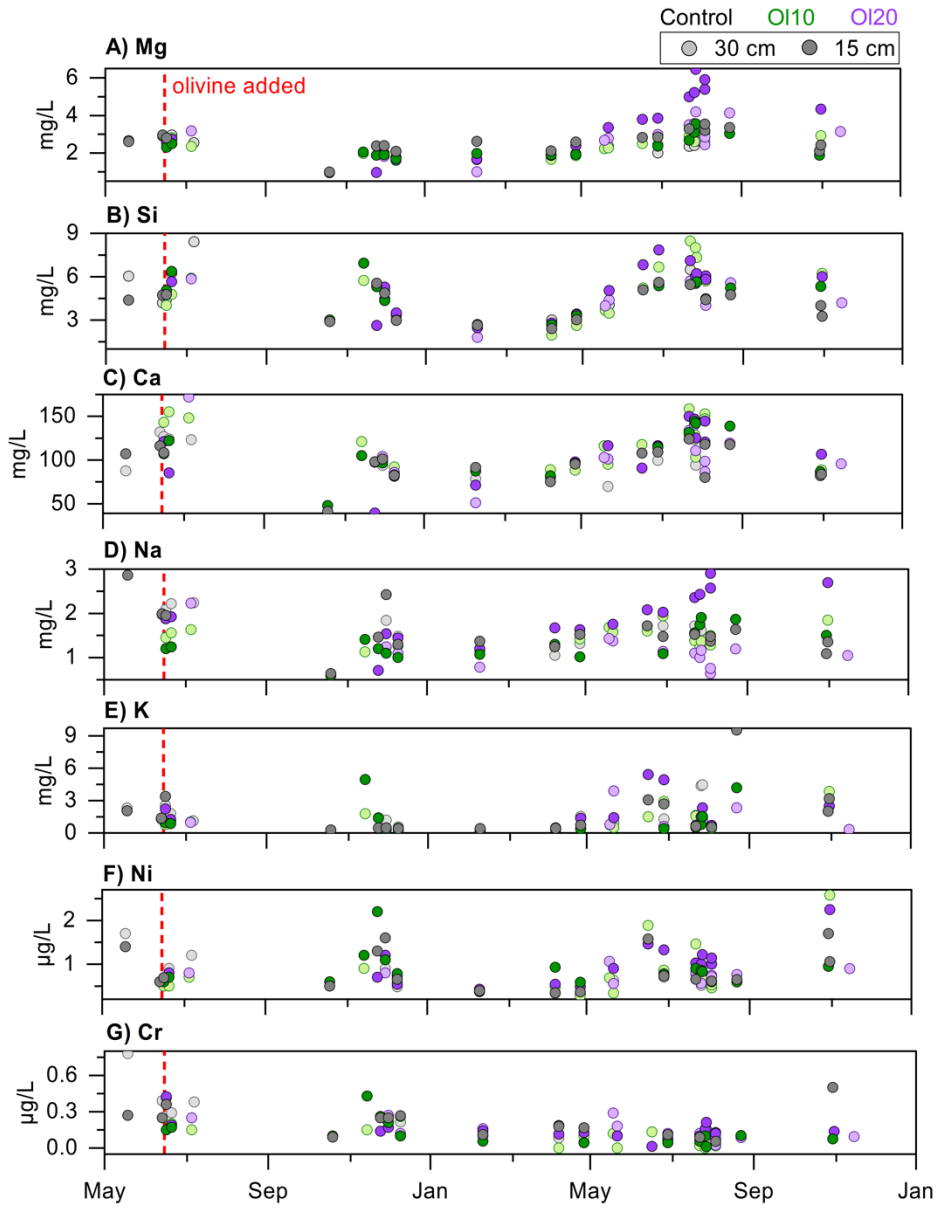

Figure 3.7. Concentrations of major cations, trace elements, and macronutrients in porewaters at 15 and 30 cm depths in the control, Ol10, and Ol20 plot over two monitoring periods. Larger data gaps occur when water samples were unobtainable, e.g., during winter months.

The relationship between alkalinity and the sum of base cations at 15 cm consistently aligned along or below the 1:1 stoichiometric ratio for calcite weathering, irrespective of the amendment (Fig. 3.8). These data points show a strong correlation

with calcite dissolution and bicarbonate formation, plotting well below the 1:2 carbonic acid weathering line (Fig. 3.8). In contrast, nearly all 30 cm porewater samples plot along the 1:2 carbonic acid weathering reference line. According to Dietzen and Rosing (2023), the impact of nitric [NO_3^-] and sulfuric [SO_4^{2-}] acid weathering can be ignored due to circumneutral porewaters and soil pore gas CO_2 concentrations ~12–50× atmospheric levels. Additionally, the measured NO_3^- (3.5 ±4.7 mg/L) and SO_4^{2-} (1.9 ±1.6 mg/L) concentrations over time were not significantly elevated from atmospheric inputs (1.9 and 0.8 mg/L, respectively; Appendix D).

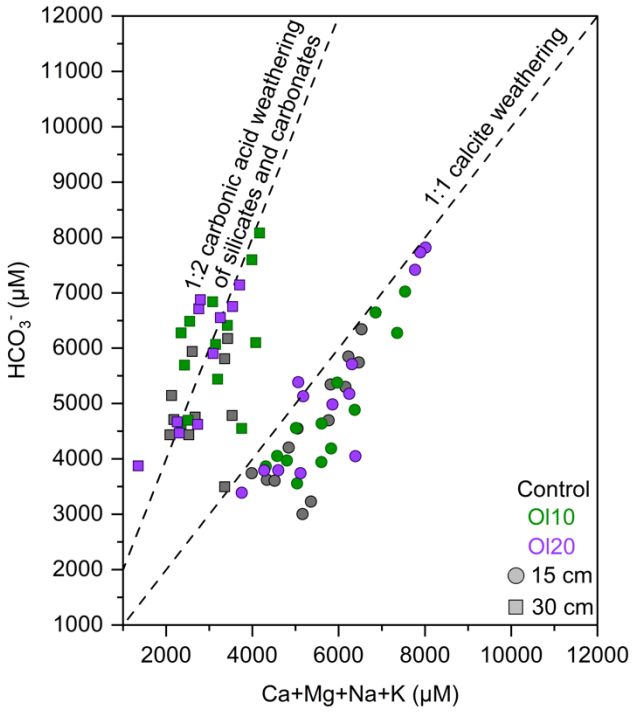

Figure 3.8. Major cation sum (Ca+Mg+Na+K) molar concentrations as a function of alkalinity in 15 cm and 30 cm porewater samples across all plots. Dashed lines indicate the stoichiometric ratio for calcite weathering and bicarbonate formation (1:1) and carbonic acid weathering of silicate and carbonate minerals (1:2).

Porewaters from the control and amended plots exhibit a strong positive correlation between Mg and Ca concentrations (Fig. 3.9A). However, the similarity in

magnitude and trend between Mg and Ca across all plots suggests minimal olivine dissolution. The control and Ol10 porewaters show near-parallel slopes, indicating consistent Mg depletion in the amended plot relative to the control, whereas Ol20 exhibits Mg enrichment in the final four samples collected for the experiment (Fig. 3.9A). Throughout, Ca remained the dominant cation in all samples showing little fluctuation from the control range (Fig. 3.9A).

Conversely, relationships between Mg and Si were less distinct, supported by a weak covariance in the control, Ol10, and majority of Ol20 plot samples (Fig. 3.9B). All amended porewaters showed enrichment in Si compared to Mg concentrations, with only the Ol20 porewaters having demonstrated an increase in Mg concentrations near the end of the second monitoring period (Fig. 3.9B). Still, all samples plotted below the stoichiometric forsterite dissolution ratio.

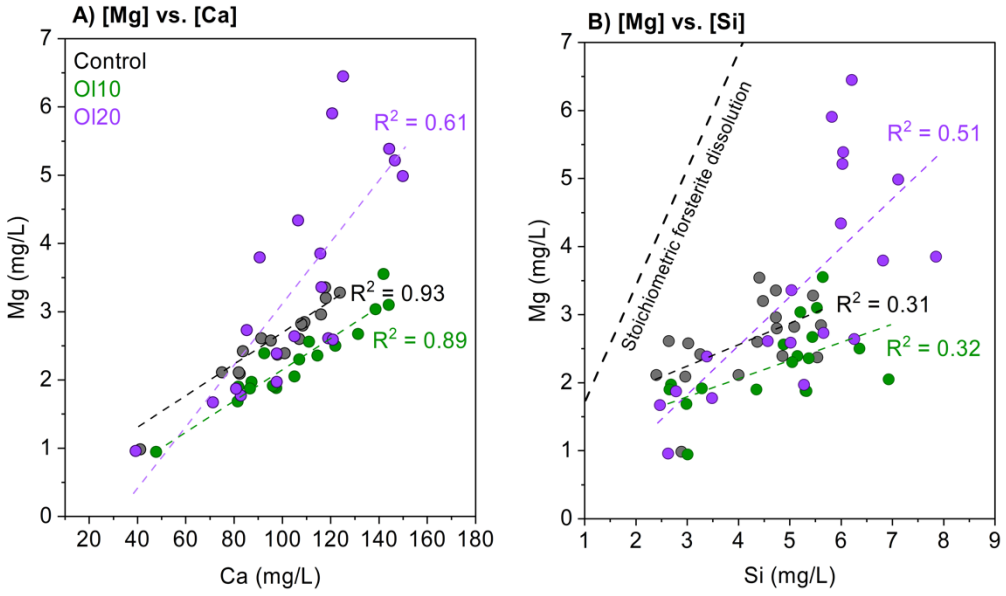

Figure 3.9. Concentrations of Mg against Ca (A), and Si (B) in porewaters from the control, Ol10, and Ol20 plots over 2 yr.

3.3.2.3 Carbonate precipitation

The olivine amendment did not affect TIC content throughout the soil profile in either monitoring periods (Fig. 3.10). The control soil showed fluctuations within 1–2%C, with notably high variability at the lowest analyzed increment (±1.0 %C). A dilution effect was observed within the top 5 cm of soil due to the application of olivine (0.02% TIC), resulting in TIC levels that were 0.5–1.5% lower compared to the control. The majority of TIC measurements remained within the control range, except for the mid-profile of the Ol20 plot in both monitoring periods, where TIC was slightly below the control range.

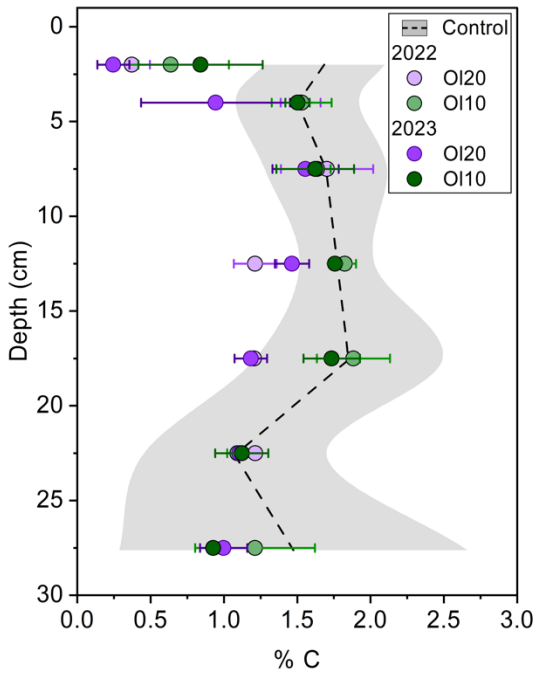

Figure 3.10. Total inorganic carbon (%C) of field plot soil cores (0–25 cm) from the Ol10 and Ol20 plots in 2022 (n=6) and 2023 (n=6), approximately 1 yr apart. The control baseline for TIC was averaged over both monitoring periods (n=12).

3.3.3 PROFILE

Weatherable base cations (BCw: Ca + Mg + K + Na) release minimally varied between the control and amended plots, with the only differences being slightly higher Ca and Si release rates in the amended plots (Table 3.7). Ca contributed the most to the total BCw rate releasing 23.1 of the 24.6 keq/ha/yr total in the control, and 24.1 of the 25.7 keq/ha/yr in the amended plots. Si release was within the same order of magnitude exhibiting rates of 11.5 keq/ha/yr in the control and 12.1 keq/ha/yr in the amended plots. Remaining BCs, Mg, K, and Na exhibited release rates of approximately 0.6, 0.3, and 0.7 keq/ha/yr, respectively in all plots.

The minerals most likely to contribute to the cation pool were assumed to be the added olivine in the amended plots, and calcite and albite in the pre-existing soils due to their abundance (16.1 wt.% and 23.4 wt.%, respectively) and least-recalcitrant properties compared to the remaining minerals (e.g., quartz and microcline). Olivine content was positively correlated with Mg and Si release, which was supported further by the greater cation release rate from olivine weathering in the Ol20 plot (0.2 eq/ha/yr) compared to the Ol10 plot (0.1 eq/ha/yr; Table 3.8); however, on a per-mass-basis, these plots exhibit identical BCw release rates. Calcite weathering was estimated to be slightly greater in the amended plots (24.5 keq/ha/yr) compared to the control soils (23.5 keq/ha/yr), likely due to cation exchange as a result of the added Mg. Pre-existing silicate weathering was consistent in all plots yielding an average BCw release rate from albite of ~0.7 keq/ha/yr.

Table 3.7. Cation release rates (keq/ha/yr) in the control and amended plots.

	Ca	Mg	K	Na	Si	BCw
Control	23.1	0.62	0.27	0.64	11.5	24.6
Amended	24.1	0.65	0.28	0.66	12.1	25.7

Table 3.8. Model predicted BCw rates (keq/ha/yr) for primary minerals in the control, Ol10, and Ol20 runs. Dominant BCw ion released from each mineral is in parentheses.

	Cal (Ca)	Ab (Na)	Mc (K)	Hbl (Mg)	Px (Mg)	Chl (Mg)	Ol (Mg)
Control	23.5	0.71	0.25	0.21	-	-	-
Ol10	24.5	0.74	0.26	0.22	0.0002	0.00007	0.0001
Ol20	24.5	0.74	0.26	0.22	0.0003	0.0001	0.0002

Minerals modelled include Cal calcite, Ab– albite, Mc– microcline, Hbl– hornblende, Px– pyroxene, Chl– chlorite, Ol– olivine.

3.4 Discussion

3.4.1 Olivine field weathering rates

The powdered olivine, comprised of 89.4 wt.% forsterite, provides a relatively reactive mineral for CO_2 removal (Eq. 1) in neutral environments (~$10^{-10.6}$ mol/m^2/s; Palandri and Kharaka, 2004). Assessing feedstock CDR potential in dissolution experiments often relies on Mg release from reacting Mg-silicates as a proxy (Amann et al., 2020; te Pas et al., 2023). However, variations in experimental conditions lead to considerable discrepancies in cation releases and thus, estimated CDR rates (0.02–4.2 t CO_2/ha/yr; (ten Berge et al., 2012; Dietzen et al., 2018; Amann et al., 2020; Pogge von Strandmann et al., 2022). In the batch leach experiments, the olivine powder yielded cation releases of 7.5 ±0.2 g Mg/kg, 4.5 ±0.1 g Si/kg (with a Mg:Si ratio of 1.7), and 0.05 ±0.002 g Ca/kg after two weeks under enhanced conditions. Based on the Steinour equation used in Chapter 2, the geochemical oxide data translates to a CDR potential of 808–916 kg CO_2/t. Thus, the Ol10 and Ol20 plots have maximum CDR potentials of ~81–92 and 162–183 t CO_2/ha upon complete weathering.

3.4.1.1 CDR via solubility trapping

In the amended weathering plots, the olivine amendment, soil silicates (e.g., albite), and soil carbonates (calcite) would have reacted with CO_2, potentially contributing to overall CDR. The control plot CDR would only involve contributions from the latter two phases. Since the olivine powder did not provide a substantial source of Ca, the CO_2 removed through calcite weathering was derived from Ca concentrations specific to each plot rather than applying the control Ca concentrations uniformly across all calculations. The water budget method from moisture probe calibration is identical to Chapter 2. Equations for calculating CDR via solubility trapping are summarized by Equations 3–5.

$$CDR_{total} = (CDR_{silicate} + CDR_{carbonate})_{Soil} + (CDR_{silicate})_{Amendment} \quad (3)$$

$$CDR_{total,carbonate,silicate} = \sum_{mo}\left[([DIC, Ca, Si] \times V_P) \times \frac{1\ g}{1000\ mg} \times n\frac{M_{CO_2}}{M_{C,Ca,Si}}\right] \times \left(\frac{P_{year}}{P_{period}}\right) \quad (4)$$

$$CDR_{total} = (CDR_{silicate} + CDR_{carbonate})_{Soil} + (CDR_{silicate} + CDR_{carbonate})_{Amendment} \quad (5)$$

where CDR_{total} (g/m^2/yr) is the total amount of CO_2 removed via solubility trapping calculated from DIC concentrations in porewaters, with contributions from $CDR_{silicate}$ and $CDR_{carbonate}$ derived from mineral inputs in the local soil and the amendment (Eq. 3). Monthly averages of [*DIC*], [*Ca*], and [*Si*] concentrations (mg/L) were used to calculate total weathering and carbonate and silicate weathering contributions, factoring in V_P as the total percolation value (L) for the respective month (Eq. 4). Molar masses of carbon forms (M_{CO2} and M_C) and cations (M_{Ca} and M_{Si}) were utilized with *n* representing the moles reacting to form CO_2, which is 1 for DIC (CDR_{total}), ½ for carbonates ($CDR_{carbonate}$), 2 for soil silicate (i.e., albite dissolution) and 4 for amendment silicate (i.e.,

forsterite dissolution; $CDR_{silicate}$). Summed monthly CO_2 sequestration extrapolated annually considered the total precipitation amount throughout that year (P_{year}) and precipitation during the monitoring period (P_{period}). Equation 5 partitioned the total CDR rate, allocating mineral weathering contributions based on Si and Ca loadings. These percentages were applied to the CDR_{total} derived from direct inorganic carbon measurements, correcting the overall CDR rate to account for carbonate contribution.

Olivine weathering was quantified using Si fluxes rather than Mg as Ca tends to readily exchange with Mg. Additionally, the silicates in the pH-neutral soil possess slower weathering rates (e.g., albite: $10^{-11.2}$ mol/m^2/s, microcline: $10^{-12.5}$ mol/m^2/s, quartz: $10^{-11.2 \text{ to } -15}$ mol/m^2/s; Heřmanská et al., 2022) compared to forsterite ($10^{-10.6}$ mol/m^2/s; Palandri and Kharaka, 2004); however, due to the unknown magnitude of secondary silicate precipitation, these solubility trapping rates via olivine weathering are likely underestimated. Furthermore, porewater measurements rely on regular sampling as there is a risk for missed cation leaching signals due to drainage. A dunite field trial observed water chemistry concentrations ~14% higher in an in-situ mesocosm compared to the field plots, possibly due to sustained weathering reactions from non-draining soil moisture (Vink et al., 2022).

Total CDR derived from 15 cm porewater DIC, treated as a direct HCO_3^- measurement in circumneutral waters (Fig. 3.6A, B), indicated greater DIC loadings in the Ol20 plot, yielding ~0.1 t CO_2/ha higher CDR rate over 2 yr relative to the control, while the Ol10 plot showed ~0.01 t CO_2/ha less (Fig. 3.11). The primary CDR contributor across all plots was soil carbonate weathering (Fig. 3.8), with Ca concentrations alone driving rates of 0.46, 0.44, and 0.53 t CO_2/ha over 2 yr in the

control, Ol10, and Ol20 plots, respectively. Calcite weathering primarily facilitated the DIC increases at 30 cm, supported by the cross plot of major cations and alkalinity plotting deeper porewaters along the 1:2 ratio depicting carbonate mineral dissolution and HCO_3^- generation (Fig. 3.8). Soil silicate weathering, mainly of albite (23.4 wt.%), contributed ~0.05 t CO_2/ha over 2 yr in all plots. Olivine powder in the Ol10 plot achieved a 0.02 t CO_2/ha CDR over 2 yr, not exceeding the control. However, the olivine powder in the Ol20 plot removed an additional 0.04 t CO_2/ha over 2 yr, with peak removal in July 2023, coinciding with maximum Mg and Si concentrations recorded (Fig. 3.7A, B).

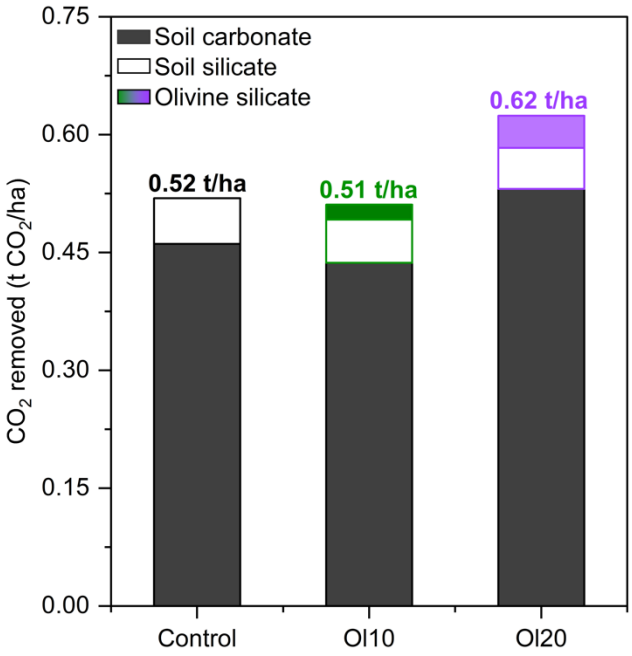

Figure 3.11. Cumulative CO_2 removal (t CO_2/ha) over 2 yr calculated via DIC and divided into soil mineral weathering and olivine powder dissolution in the control, Ol10, and Ol20 plots.

3.4.1.2 CDR via mineral trapping

In the olivine plots, carbonate precipitation was not anticipated since there were no additional sources of Ca available to form excess Ca-carbonates (e.g., calcite), and the field conditions were not conductive to the precipitation of Mg-carbonates (e.g., magnesite). Furthermore, saturation indices confirmed that porewaters were undersaturated with respect to magnesite and hydromagnesite (Appendix C). TIC values in soil cores from the amended plots generally fell within the control range during both monitoring periods, except near the surface where amendment mixing diluted soil carbonate (Fig. 3.10).

3.4.1.3 Field olivine dissolution rate

Comparison of Mg, Ca, and Si concentrations in porewaters from each plot allows for assessment of the extent of mineral dissolution (i.e., soil carbonate, soil silicate, olivine). Solutions in the control and olivine-amended plots exhibited a strong correlation between Ca and Mg concentrations, aligning primarily with the control trend, which reflected ongoing dissolution of pre-existing soil carbonates (Fig. 3.9A). Notably, the Ol20 plot showed enrichment in Mg during the second monitoring period, deviating from the control average. This enrichment was similarly evident in the covariance of Mg and Si concentrations, where Ol20 concentrations approached those expected from stoichiometric forsterite dissolution (Fig. 3.9B). Like most silicates, olivine tends to weather incongruently in nature, with Mg-O bonds breaking faster than Si-O bonds (Farhang et al., 2017). Unexpectedly, in this experiment Mg/Si molar ratios, which should ideally be ≥2, favoured Si and ranged from 0.5–1.6 in porewaters where Mg

exceeded control levels. These increases in Mg towards the end of the experiment coincided with ~40 mg/L increases in Ca (Fig. 3.7A, C), suggesting potential divalent cation exchange or adsorption involving excess Mg released from olivine dissolution (Hartmann et al., 2013), which would otherwise elevate Mg/Si to >2. This delayed increase demonstrates a possible lag in cation transport, with the total lag time ranging from years to decades dependent on the cation exchange capacities of the background soils (Kanzaki et al., 2024). Despite these observations, evidence of olivine dissolution persisted through elevated Si concentrations, which was quantified using a modified version of the weathering rate equations utilized by Amann et al. (2020) and Iff et al. (2024) (Eq. 6).

$$W_r = \frac{[(V_P \times [Si]_{olivine}) - (V_P \times [Si]_{control})]}{SSA \times m_{olivine}} / t \quad (6)$$

where W_r represents the surface area normalized dissolution rate of olivine (mol/m^2/s), V_P denotes the percolation volume in each plot for a given month (L), and $[Si]$ is the average Si molar concentration (mol/L) in the porewaters of the amended plot and control plot for a given month. This molar flux of Si is equal to the olivine molar flux assuming 1 mol Si per mole olivine. SSA is the specific surface area of the olivine powder (1.64 m^2/g) determined using the BET method, and $m_{olivine}$ is the mass of olivine added to each plot (g). Time factor (t) converts the flux measured in one month to seconds.

Initially, olivine weathering rates were not discernible due to soil interference, with Si concentrations in the amended plots consistently aligned with the control range (Fig. 3.7B). Si-based weathering rates for the Ol20 plot ($10^{-14.4}$ to $10^{-13.2}$ mol Ol/m^2/s) were only detected in the last five months of the experiment, and in the last two months

for the Ol10 plot (~$10^{-13.8}$ mol Ol/m^2/s). These rates approximate to those calculated by Amann et al. (2020) ($10^{-13.8}$ mol Ol/m^2/s), who reported Mg-based CDR rates similar to those reported in this study. Overall, these olivine weathering rates are substantially slower than experimental dissolution rates by 3–4 orders of magnitude (Heřmanská et al., 2022).

3.4.2.4 Rate comparison

The olivine CDR rates in this study were orders of magnitude slower than most ERW studies amending a controlled system with olivine (Table 3.9). Only CDR rates reported by Amann et al. (2020), who used a similarly high dosage rate (220 t/ha) of coarse dunite in a mesocosm experiment, aligned with the field CDR rates of the 200 t/ha olivine plot. The olivine powder used in this field experiment characteristically aligned with a medial class between the fine and coarse dunite used by Amann et al. (2020), including a SSA that was slightly greater than the coarse dunite and a D80 ~100 μm larger than the fine dunite. The CDR similarities are attributed to comparable experimental features including near-neutral soil pH, natural simulation of climate (e.g., drying out periods), and irrigation inputs that match annual precipitation recorded in Peterborough, Ontario. Although this mesocosm study used a Mg mass-balance approach, quantified CDR rates were extrapolated from outflow concentrations omitting the Mg adsorbed to soil particles which would increase rates by one order of magnitude had soil samples been analyzed (Amann et al., 2020). Amann et al. (2020) recognized that the ideal derivation of CDR rates is from direct inorganic measurements (e.g., DIC), but study constraints restricted their design to Mg-flux derived rates with consideration of

amorphous silica layer formation. However, the similarities in conditions and acknowledgement of cation exchange throughout the soil profile are agreeable for comparing to this field study.

A field experiment by Holzer et al. (2023) measured CDR rates using alkalinity measurements of porewaters in circumneutral soils amended with just metabasalt or a mixture of metabasalt and olivine. The difference between these amendment CDR rates, conservatively assuming that the difference is contributed by the extra olivine amendment, was 0.03 t CO_2/ha over a three-month monitoring period. This study was conducted in California during their winter months which still experienced an average daily temperature maximum of 22ºC and two substantial rainfall events (33 and 58 mm) that occurred over ~3 days, which facilitated weathering and increased alkalinity concentrations of the metabasalt and olivine amended soils to over 500 mg C/L (Holzer et al., 2023). Although the estimated olivine CDR rates were accelerated in the California field study likely due to climate influence, they are on the same order of magnitude as the rates calculated in this study subject to a much colder climate.

Magnesium mass balances methodologies are a popular method used in contained Mg-silicate dissolution experiments, assessed through water budget analyses (Renforth et al., 2015; te Pas et al., 2023; Clarkson et al., 2024) and solid samples analyses from field trials (Dietzen and Rosing, 2023; Beerling et al., 2024). Olivine-rich (Fo: >80 wt.%) column experiments conducted at varying temperatures (4ºC, 19ºC, and 32ºC) have provided insights into temperature-influenced CDR rates calculated from Mg and Si releases in soil (Renforth et al., 2015; Pogge von Strandmann et al., 2022; Iff et al., 2024). For instance, Iff et al. (2024) estimated that at 4ºC and 19ºC, approximately 0.15 t

CO_2/ha/yr could be sequestered with an application of ~127 t/ha of olivine, using Si-based weathering rates. Conversely, Mg-based rates suggested higher CDR rates of ~2 and ~13 t CO_2/ha/yr at those temperatures, respectively (Renforth et al., 2015; Pogge von Strandmann et al., 2022). In a pot experiment using olivine (1.6–204 t/ha), ten Berge et al. (2012) reported CDR rates of 0.3–2.7 t CO_2/ha over ~7 months, derived from bioavailable Mg accumulated in soil and plant biomass as a proxy for olivine weathering. Similarly, Dietzen et al. (2018) applied olivine at 10–50 t/ha and estimated rates of 3.1–4.2 t CO_2/ha after just three months.

Discrepancies in CDR rates between pure olivine and dunite studies primarily stem from differences in dosage rates, surface area, and the soil type amended, given their nearly identical monomineralic compositions. The ERW laboratory studies by ten Berge et al. (2012) and Dietzen et al. (2018) reported CDR rates of fine olivine applied to soils up to two orders of magnitude faster than this study despite lower application dosages. This discrepancy is attributed to the acidic sandy soils (pH: 3.6–4.8) used in these experiments facilitating faster dissolution rates, as well as their use of Mg mass balances in soil samples to quantify CDR rates which includes Mg adsorbed to soil particles. Additionally, ten Berge et al. (2012) irrigated from the top and bottom of the pots to ensure no preferential flow paths formed, sustaining soil moisture and mineral reactions.

Element proxies assume that all cation loss results from leached cations reacting with carbonic acid to generate bicarbonate and dissolved cations, thus representing an upper estimate of CDR. Flow-through leaching experiments showed CDR rates 45.1% slower when derived from inorganic carbon analyses (e.g., DIC and alkalinity) compared to those calculated from cation releases (te Pas et al., 2023). Additionally, experimental

dissolution rates are orders of magnitude faster than those observed in field experiments (Brantley and Olsen, 2014 and references therein); thus, laboratory results do not accurately extrapolate to field conditions necessitating in-field carbon monitoring.

Table 3.9. Olivine ERW in soil studies.

	Study type	Dosage (t/ha)	CDR rate (t CO_2/ha [time])	Methodology
ten Berge et al., 2012	Pot	1.6–204	0.3–2.7 [7 months]	Mg mass balance (soil)
Dietzen et al., 2018	Pot	10–50	3.1–4.2 [3 months]	Mg mass balance (soil)
Amann et al., 2020	Pot	220 (coarse & fine)	0.02 & 0.05 [1 yr]	Mg mass balance (water)
Holzer et al., 2023	Field	80 (metabasalt) + 27 (olivine)	0.15 [3 months]	Inorganic carbon
Iff et al., 2024*	Column	127	0.15 or 2–13 [1 yr]	Si or Mg mass balance (water)

* Recalculating rates using Si reported by Renforth et al. (2015) and Pogge von Strandmann et al. (2022).

3.4.2 PROFILE for ERW

3.4.2.1 CDR via PROFILE modelling

PROFILE was used to estimate the release of base cations (BC_w) from individual minerals to calculate CDR rates from the weathering of soil carbonates, soil silicates, and the olivine amendment. Ca releases were attributed to calcite weathering, which was ~0.5 t Ca/ha/yr in all plots, with CDR rates halved to account only for newly removed CO_2 (0.27 ±0.01 t CO_2/ha/yr), assuming calcite only reacted with carbonic acid. Soil silicate weathering, primarily of albite, was quantified using Na concentrations, while olivine weathering was evaluated based on Mg releases. The estimated natural CO_2 consumption rates (0.03 ±0.0007 t CO_2/ha/yr) as a result of Na release from albite weathering (~0.02 t Na/ha/yr) were relatively consistent across all PROFILE runs. PROFILE estimated slightly faster Mg releases from olivine weathering in the Ol20 plot (2.4×10^{-6} t

Mg/ha/yr) compared to the Ol10 plot (1.4×10^{-6} t Mg/ha/yr), resulting in CDR rates of 1.5×10^{-5} and 8.5×10^{-6} t CO_2/ha/yr, respectively.

Soil CO_2 consumption rates estimated by PROFILE were only 3–18% higher than the empirically measured rates from DIC and porewater chemistry, whereas empirically derived olivine CDR rates for the Ol10 and Ol20 plot were ~3 orders of magnitude greater than those estimated by PROFILE (Table 3.10). PROFILE estimated olivine weathering at a rate much slower than albite which does not reflect their experimental weathering rates under neutral pH conditions (olivine: $10^{-10.6}$ mol/m^2/s, albite: $10^{-11.2}$ mol/m^2/s). This discrepancy is likely due to the dominance of albite distributed throughout a 30 cm soil profile (~84 kg) in contrast to the dense layer of olivine at only the surface of the amended plots. The amended plots were expected to exhibit negligible olivine CDR contributions since the olivine appeared inert in terms of changes in DIC (Fig. 3.6B) and cation fluxes (Fig. 3.9) relative to the control.

Table 3.10. CDR rates generated by PROFILE and the porewater chemistry approach.

	PROFILE rates (t CO_2/ha over 2 yr)				Empirical rates (t CO_2/ha over 2 yr)			
	Soil carbonate	Soil silicate	Olivine	Total	Soil carbonate	Soil silicate	Olivine	DIC
Control	0.52	0.06	-	0.58	0.46	0.06	-	0.52
Ol10	0.54	0.06	0.00002	0.60	0.44	0.05	0.02	0.51
Ol20	0.54	0.06	0.00003	0.60	0.53	0.05	0.04	0.62

3.4.2.2 Sensitivity analysis

Using a static model to estimate annual rates in a dynamic system introduces uncertainties influenced by numerous climatic sensitivities (e.g., temperature and soil moisture), as well as assumptions about mineral weathering behaviour (e.g., reactive surface area). To evaluate the model sensitivity to these variables, temperature, soil

moisture, and olivine surface area were assigned a maximum and minimum value representing climatic extremes, fluid-mineral interactions, and potential reactive surface areas. Since surface area inputs from N_2 gas-adsorption analyses may not accurately quantify accessible mineral sites (i.e., excluding micropores and assuming a uniform geometry), surface area of the amendment layer was increased until empirical CO_2 removal rates were achieved.

High heat is well established as a beneficial factor for mineral weathering in ERW applications (White et al., 1999; Hartmann et al., 2013; Iff et al., 2024), with sustained high temperatures (the maximum daily average in Peterborough, ON) yielding accelerated weathering rates and improved CDR (Table 3.11). Warmer months during the field experiment also corresponded with the greatest measured concentrations of Mg and Si released from the amended plots (Fig. 3.7A, B). The extreme temperatures experienced in a temperate zone were accounted for in the initial modelling run (Table 3.10) by dividing PROFILE inputs into summer and winter weathering, combining rates via a weighted average to best reflect the continental climate (Liu et al., 2024). Additionally, increasing soil moisture improved olivine weathering and CO_2 removal even during the winter weathering sequence (Table 3.11), likely as a result of sustained interactions between olivine and reactive aqueous fluids (Oelkers et al., 2018). High temperatures and soil moisture are characteristics of tropical regions, which are recognized as site for the most efficient mineral weathering, and thus ERW projects (Taylor et al., 2016; Beerling et al., 2018, 2020).

Increasing surface area by further crushing materials has proven effective in significantly improving CDR rates (Amann et al., 2022). However, relying on the initial

specific surface area often rests on the incorrect assumption that weathering occurs uniformly across the mineral surface. Rather, weathering is favoured at defect sites in the crystal structure (e.g., etch pits; Oelkers et al., 2018) leading to more rapid weathering and leaching at the beginning of an experiment (Swoboda et al., 2022; Vandeginste et al., 2024). Thus, the specific surface area measured does not accurately reflect the true surface area available for weathering reactions. Given that a three-order-of-magnitude increase in amendment layer surface area was required to achieve the empirically measured CDR rates (Table 3.11), this discrepancy suggests that specific surface area measurements might significantly underestimate the reactive surface areas involved, calling into question the reliability of geochemical models used in ERW field experiments.

Table 3.11. Sensitivity analysis of temperature, soil moisture, and surface area on the olivine BCw release rate (negative or positive % influence) and CDR rate (t CO_2/ha over 2 yr).

Input	Input value		Effect on olivine weathering rate[a]		Ol20 CDR (t CO_2/ha over 2 yr)
	Min	Max	Min	Max	Min–Max
Temperature (ºC)	-13	27	-45%	+43%	0.00001–0.0001
Soil moisture (m^3/m^3)	0.1	0.5	-56%	+54%	0.00001–0.0001
Surface area (m^2/m^3)	8.2×10^8		×1000 increase		0.03

Empirical and PROFILE Ol20 CDR rates were 0.04 and 0.00003 t CO_2/ha over 2 yr, respectively.

3.4.2.3 Geochemical modelling implications

While PROFILE modelling has not yet been used in large-scale ERW field trials, it has demonstrated its value in mapping regional soil weathering rates across Europe, the mid-Atlantic United States, and Southern Ontario (Koseva et al., 2010; reviewed by Sverdrup et al., 2019). PROFILE could be strategically integrated into various phases of an ERW field study to ensure optimal CDR. Initially, empirical data can help estimate the

climate suitability for mineral weathering and determine optimal application rates and surface densities for effective weathering. During deployment, PROFILE can estimate CDR and mineral weathering rates as soil conditions change in response to the amendment (e.g., pH adjustments), using updated empirical measurements. For remote deployments, reduced sampling frequency can be adopted with PROFILE providing estimates of ongoing weathering rates.

Models applied in carbon removal studies, including inverse (mass-balance) geochemical modelling (Paulo et al., 2023; Gill et al., 2024), 1-D reactive transport modelling (Beerling et al., 2020; Lewis et al., 2021; Kantzas et al., 2022; Vienne et al., 2022; Baek et al., 2023), variations of shrinking core models (Haque et al., 2019; Rinder and von Hagke, 2021; Vink and Knops, 2023; McDermott et al., 2024), and reduced order modelling (Jerden et al., 2024), are often used as predictive tools when combined with laboratory tests and field data calibration (Lu et al., 2024). As ERW sites scale to multiple hectares, evaluation of these models applied to natural systems is required due to inherent limitations (Vienne et al., 2022). Even simple systems with singular reacting amendments (e.g., monomineralic feedstocks) have shown substantial discrepancies between modelled and observed dissolution rates, especially regarding cation release (Lu et al., 2024). Paulo et al. (2023) emphasized the value of using accurate, low-maintenance models for estimating passive weathering rates but also stressed the importance of regular sampling to calibrate these models and verify extrapolated CDR rates to reduce uncertainties.

Recent evaluations of mesocosm studies (Kelland et al., 2020; Vienne et al., 2022) and an ERW field experiments (Beerling et al., 2024) using a reduced order model

– which performs mass balance and dissolution kinetic calculations while accounting life-cycle variables – reported net CDR rates for the applied basalt (Jerden et al., 2024). Although mesocosm CDR rates estimated by the model were agreeable with the published ranges, field rates reported by Beerling et al. (2024) were underestimated by a factor of three, likely due to their derivation of CDR rates from a mineral weathering proxy (Jerden et al., 2024). Additionally, the shrinking core model (Hangx and Spiers, 2009) – which predicts the time taken for spherical grains to be completely consumed – has undergone various modifications to suit ERW projects (Rinder and von Hagke, 2021; Vink and Knops, 2023). For example, Vink and Knops (2023) accounted for the non-uniformity of particle sizes in applied feedstocks and developed a size-fractionated weathering component with a pre-determined field weathering rate of olivine (Vink et al., 2022). This approach allowed for separate calculations of CO_2 uptake and Mg and Ni release. Their model predicted that complete consumption of a 1-tonne per hectare dosage of olivine would take 250 yr and anticipated a substantial decline in Ni release after just one year due to the rapid weathering of ultra-fine particles (<50 μm; Vink and Knops, 2023). While models are valuable for predicting the effectiveness of rock powders, application sites, and dosages, they must be calibrated with empirical measurements to ensure accurate representation of sites for ERW projects (Jerden et al., 2024).

3.4.3 Elements of concern

In the context of ERW deployments using olivine, the release and potential accumulation of toxic elements like Ni and Cr is a probable outcome that would inadvertently impact the surrounding environment (Dupla et al., 2023). There is a threat

to food safety by adding alkaline minerals to agricultural lands, potentially leading to metal leaching into porewaters, adsorption to soils, and increased crop uptake (Dupla et al., 2023).

Ni and Cr were monitored to assess the safety of high olivine applications applied to soils, with results transferrable to olivine-rich feedstocks (e.g., dunite). In the 10 kg and 20 kg amended plots, 22.8 and 45.5 g of Ni and 7.0 and 13.9 g of Cr were added to the soil, respectively. Soil porewater concentrations of these elements were compared to surface water quality thresholds set by the Ontario Ministry of the Environment (25 µg/L Ni: MOE, 1979) and the Canadian Council of Ministers of the Environment (1 µg/L Cr: CCME, 1999). While Ni concentrations in pure olivine leachates from the CO_2 incubator were nearly 500× that of the soil leachate and about 6× the maximum threshold (147 µg/L; Table 3.6), only trace amounts were observed in porewaters from the amended plots (maximum: ~2.2–2.6 µg/L Ni; Fig. 3.7F), well below regulatory limits set by the MOE. These results suggest that the vast majority of Ni remained within the olivine or immobilized within the soil profile, which aligns with previous olivine dissolution experiments (Pogge von Strandmann et al., 2022; Iff et al., 2024).

Similarly, Cr concentrations, although showing variability, remained largely below detection limits in olivine leachates and were minimal in soil porewaters of the amended plots (maximum: ~0.43 µg/L Cr; Fig. 3.7G), indicating low mobility attributed to the neutral pH range measured in these soils (pH values of 7–8; Dupla et al., 2023). Maximum Cr concentrations in the field plot porewaters were observed in the control plot (~0.8 µg/L) and averaged 0.21 ±0.16 µg/L, reflecting the influence of PC1 porewater chemistry concentrations (Fig. 3.4).

Considering the application rates of olivine feedstocks, concerns primarily focus on Ni accumulation due to its prevalence in porewaters and likely retention within the soil profile. The low concentrations of Ni and Cr in porewaters from the Ol10 and Ol20 plots are reassuringly below water quality thresholds, highlighting the feasibility of alkaline minerals in ERW without significant environmental risk related to water contamination. Longer term weathering and accumulation still remain a risk for ultramafic applications, restricting dosage applications at agricultural sites; although ERW deployments on industrially degraded lands could also be remediated with rock powders and are subject to industrial regulations that tend to have a higher threshold (Miller and Naeth, 2017).

Soil accumulation ($CCME_{agricultural/residential}$: 45 mg Ni/kg, 64 mg Cr/kg; $CCME_{commercial/industrial}$: 89 mg Ni/kg, 87 mg Cr/kg) was not assessed in this experiment. Haque et al. (2020) reviewed metal leaching data related to ERW projects and proposed 113 t/ha as a maximum application for olivine containing ~3 g Ni/kg olivine (3,200 t/ha with concern of Cr in olivine containing 150 mg Cr/kg). Renforth et al. (2015a) performed a similar calculation based on empirical data from olivine-amended soil columns, considering the density of soil and accumulation depth (20 cm), reporting a maximum dosage of 95 t/ha to satisfy a Ni threshold of ~100 mg Ni/kg soil (near the Canadian commercial/industrial land use threshold). Dupla et al. (2023) modelled toxic metal accumulation in soils from ultramafic rock (~3 g Ni/kg) applied annually (40 t/ha), reporting exceedances of Canadian thresholds in less than 5 years. However, these soil cumulation values are calculated from the entire quantity of metals within a sample after digestion and do not consider the low leaching potential from resistant phases and

immobility of metals in neutral pH environments. Rapid exceedances of toxic element thresholds primarily occur in acidic conditions, such as a pH value of 4.2 used by Dupla et al. (2023), facilitating the mobility of metals. Instead, circumneutral soils that promote buffering HCO_3^- ions are sufficient for CDR while preventing metal leaching.

3.4.4 High dosage monitoring plots for field scale ERW projects

Large-scale ERW deployments necessitate robust monitoring, reporting, and verification methods to accurately quantify carbon removal (Clarkson et al., 2024). While further field testing is required to refine our method, we recommend integrating smaller-scale monitoring plots (e.g., square metre) adjacent to field-scale projects, in addition to the inset monitoring plots such as those recommended by Isometric's Enhanced Rock Weathering Protocols (Sutherland et al., 2023). These plots would be equipped with monitoring equipment and receive varying higher dosages (e.g., 2×, 5×, 10×) to ensure an ERW signal can be confidently detected amid soil interference. Higher application rates also provide insight into annual dosage strategies (Beerling et al., 2024) and the potential for toxic element accumulation (Dupla et al., 2023).

Monitoring weathering signals of amendments at lower dosages presents challenges due to variability in local and regional soil mineral weathering. Differentiating soil and feedstock mineral weathering contributions to overall CDR rates is complicated when amendments are mineralogically complex and share common minerals with the host soil. High dosages of the amendment in the research plots would ensure distinguishable signals and allow for the detection of DIC generation in the short term. Recent ERW experimentation have slightly increased minimum application rates in field and column studies, likely to ensure CDR detection (Fig. 3.12); however, the optimal

application rate of ERW feedstocks realistically applied to fields is still a subject of debate.

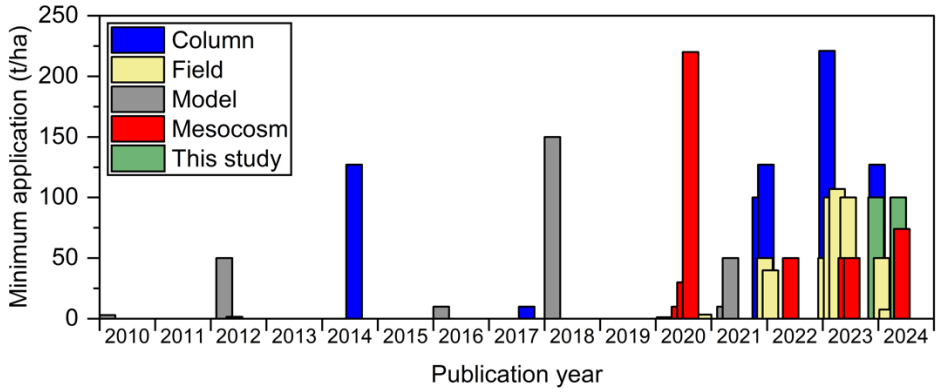

Figure 3.12. Minimum application dosages applied in ERW experiments from 2010 to 2024.

A series of plots varying in feedstock application dosages could serve as a calibration curve to understand the relationship between CDR rates and amendment dosage. However, due to the inherent variability in mineral reactivity under field conditions, this relationship is not expected to be linear (Calabrese et al., 2022; Clarkson et al., 2024). Generally, higher application rates of rock feedstocks are anticipated to enhance CO_2 removal by increasing the availability of leached cations and reactive surface areas (Abdalqadir et al., 2024). Yet, the precise thresholds for rock powder applications, beyond which CDR efficiency may decline due to porewater supersaturation or surface passivation from secondary minerals that are saturated in porewaters, remain unknown for most ERW projects (Calabrese et al., 2022; Clarkson et al., 2024).

While ERW projects commonly apply rock powders at relatively high dosages (50–200 t/ha) compared to agricultural fertilizing dosages (1–20 t/ha; Swoboda et al., 2022) to ensure a measurable signal, the potential for more efficient rates at lower

dosages due to increased fluid:rock interactions is often overlooked (Stubbs et al., 2022; Clarkson et al., 2024). The Carbon Drawdown Initiative observed diminishing CDR efficiency with higher dosage basalt applications, reporting that a 100 t/ha dose is 3× more effective than a 400 t/ha dose on a per mass basis (Paessler et al., 2023). Column experiments have similarly shown that lower dosages (<50 t/ha) exhibit a positive correlation between CDR and application rate (Dietzen et al., 2018), whereas rates above this threshold lead to significantly reduced CDR rates (Pogge von Strandmann et al., 2022). By systematically monitoring the efficiency across a wide range of dosages (e.g., 50 to 400 t/ha), projects can determine the optimal application rate to achieve specific objectives, such as maximizing CDR, providing nutrients, adjusting soil pH, and adhering to metal concentrations in waters regulations. This approach ensures that ERW strategies are both effective and environmentally sustainable, addressing global climate challenges while mitigating potential risks associated with excessive mineral application.

3.5 Conclusion

ERW experiments and field trials have demonstrated variable CDR rates, even when employing a relatively fast weathering mineral such as olivine. While the application equivalent to 200 t/ha demonstrated increased CO_2 removal rates (0.05 t/ha over 2 yr), the 100 t/ha plot did not surpass control levels despite the high application rate. Although CDR by olivine weathering was estimated to be negligible, surface area normalized dissolution rates derived from elevated Si concentrations in amended plot porewaters confirmed olivine dissolution, aligning closely with findings from mesocosm olivine weathering experiments (Amann et al., 2020). Incongruent weathering of silicates

in nature has led to popular use of Mg-fluxes to monitor olivine dissolution; however, this study demonstrated the potential of Si-fluxes in porewaters as a reliable indicator for olivine dissolution in calcareous soils where leached Mg is easily exchanged.

Existing geochemical models, such as PROFILE, designed to estimate regional soil weathering rates, could be utilized to estimate base cation release rates from soil and amendment mineral dissolutions in larger field trials. By quantifying the release of reactive elements such as Ca and Mg from alkaline minerals, PROFILE can help predict mineral dissolution efficiencies and inform decision-making regarding optimal feedstock application rates and treatment strategies at ERW deployment sites. Nevertheless, applying a static model to a dynamic system introduces uncertainties, primarily driven by climate sensitivity and simplification of complex environmental interactions. Based on base cation release rates, olivine weathering was severely underestimated by two orders of magnitude. Sensitivity analysis and evaluation against empirical data is essential to enhance the accuracy and reliability of these models in predicting CDR efficacy but should not be relied on entirely.

As ERW experimentation continues, efforts will aim to refine dosage recommendations and enhance environmental monitoring practices to support safe and effective implementation of ERW. Given the variability in feedstock mineralogy, geochemistry, and physical properties in addition to variable environmental conditions, implementing high-dosage research plots could ensure CDR signals and provide insights into the impacts of subsequent feedstock application on CDR efficiency, mineral reactivity, and potential adverse metal leaching impacts.

3.6 References

Abdalqadir, M., Hughes, D., Gomari, S. R., and Rafiq, U. (2024). A state of the art of review on factors affecting the enhanced weathering in agricultural soil: strategies for carbon sequestration and climate mitigation. *Environmental Science and Pollution Research* 31, 19047–19070. doi: 10.1007/s11356-024-32498-5

Amann, T., and Hartmann, J. (2019). Ideas and perspectives: Synergies from co-deployment of negative emission technologies. *Biogeosciences* 16, 2949–2960. doi: 10.5194/bg-16-2949-2019

Amann, T., and Hartmann, J. (2022). Carbon accounting for enhanced weathering. *Frontiers in Climate* 4:849948, 1–9. doi: 10.3389/fclim.2022.849948

Amann, T., Hartmann, J., Hellmann, R., Pedrosa, E. T., and Malik, A. (2022). Enhanced weathering potentials—the role of in situ CO_2 and grain size distribution. *Frontiers in Climate* 4, 929268. doi: https://doi.org/10.3389/fclim.2022.929268

Amann, T., Hartmann, J., Struyf, E., De Oliveira Garcia, W., Fischer, E. K., Janssens, I., et al. (2020). Enhanced Weathering and related element fluxes - A cropland mesocosm approach. *Biogeosciences* 17, 103–119. doi: 10.5194/bg-17-103-2020

Baek, S. H., Kanzaki, Y., Lora, J. M., Planavsky, N., Reinhard, C. T., and Zhang, S. (2023). Impact of climate on the global capacity for enhanced rock weathering on croplands. *Earths Future* 11. doi: 10.1029/2023EF003698

Beerling, D. J., Epihov, D. Z., Kantola, I. B., Masters, M. D., Reershemius, T., Planavsky, N. J., et al. (2024). Enhanced weathering in the US Corn Belt delivers carbon removal with agronomic benefits. *Proc Natl Acad Sci U S A* 121. doi: 10.1073/pnas.2319436121

Beerling, D. J., Kantzas, E. P., Lomas, M. R., Wade, P., Eufrasio, R. M., Renforth, P., et al. (2020). Potential for large-scale CO_2 removal via enhanced rock weathering with croplands. *Nature* 583, 242–248. doi: 10.1038/s41586-020-2448-9

Beerling, D. J., Leake, J. R., Long, S. P., Scholes, J. D., Ton, J., Nelson, P. N., et al. (2018). Farming with crops and rocks to address global climate, food and soil security. *Nat Plants* 4, 138–147. doi: 10.1038/s41477-018-0108-y

Brantley, S. L., and Olsen, A. A. (2014). *Reaction kinetics of primary rock-forming minerals under ambient conditions*., eds. H. Holland and K. Turekian. Oxford: Elsevier. doi: 10.1016/B978-0-08-095975-7.00503-9

Calabrese, S., Wild, B., Bertagni, M. B., Bourg, I. C., White, C., Aburto, F., et al. (2022). Nano- to global-scale uncertainties in terrestrial enhanced weathering. *Environ Sci Technol* 56, 15261–15272. doi: 10.1021/acs.est.2c03163

CCME (1999). Canadian water quality guidelines for the protection of aquatic life. CCME.

Clarkson, M. O., Larkin, C. S., Swoboda, P., Reershemius, T., Suhrhoff, T. J., Maesano, C. N., et al. (2024). A review of measurement for quantification of carbon dioxide removal by enhanced weathering in soil. *Frontiers in Climate* 6, 1345224. doi: 10.3389/fclim.2024.1345224

Dietzen, C., Harrison, R., and Michelsen-Correa, S. (2018). Effectiveness of enhanced mineral weathering as a carbon sequestration tool and alternative to agricultural lime: An incubation experiment. *International Journal of Greenhouse Gas Control* 74, 251–258. doi: 10.1016/j.ijggc.2018.05.007

Dietzen, C., and Rosing, M. T. (2023). Quantification of CO_2 uptake by enhanced weathering of silicate minerals applied to acidic soils. *International Journal of Greenhouse Gas Control* 125, 103872. doi: 10.1016/j.ijggc.2023.103872

Dupla, X., Möller, B., Baveye, P. C., and Grand, S. (2023). Potential accumulation of toxic trace elements in soils during enhanced rock weathering. *Eur J Soil Sci* 74, e13343. doi: 10.1111/ejss.13343

Farhang, F., Rayson, M., Brent, G., Hodgins, T., Stockenhuber, M., and Kennedy, E. (2017). Insights into the dissolution kinetics of thermally activated serpentine for CO_2 sequestration. *Chemical Engineering Journal* 330, 1174–1186. doi: 10.1016/j.cej.2017.08.073

Gill, M. J., Poduska, K. M., and Morrill, P. L. (2024). Evaluation of carbon dioxide sequestration via interaction with peridotite and peridotite-hosted groundwaters: an experimental case study with Bay of Islands Ophiolite rocks, western Newfoundland, Canada. *Can J Earth Sci* 61, 296–311. doi: 10.1139/cjes-2022-0116

Görres, C. M., Kammann, C., and Ceulemans, R. (2016). Automation of soil flux chamber measurements: Potentials and pitfalls. *Biogeosciences* 13, 1949–1966. doi: 10.5194/bg-13-1949-2016

Guo, F., Wang, Y., Zhu, H., Zhang, C., Sun, H., Yang, J., et al. (2023). Crop productivity and soil inorganic carbon change mediated by enhanced rock weathering in farmland: A comparative field analysis of multi-agroclimatic regions in central China. *Agric Syst* 210, 103691.

Hangx, S. J. T., and Spiers, C. J. (2009). Coastal spreading of olivine to control atmospheric CO_2 concentrations: A critical analysis of viability. *International Journal of Greenhouse Gas Control* 3, 757–767. doi: 10.1016/j.ijggc.2009.07.001

Haque, F., Chiang, Y. W., and Santos, R. M. (2019). Alkaline mineral soil amendment: A climate change “stabilization wedge”? *Energies (Basel)* 12, 2299. doi: 10.3390/en12122299

Haque, F., Chiang, Y. W., and Santos, R. M. (2020). Risk assessment of Ni, Cr, and Si release from alkaline minerals during enhanced weathering. *Open Agric* 5, 166–175. doi: 10.1515/opag-2020-0016

Hartmann, J., West, A. J., Renforth, P., Köhler, P., De La Rocha, C. L., Wolf-Gladrow, D. A., et al. (2013). Enhanced chemical weathering as a geoengineering strategy to reduce atmospheric carbon dioxide, supply nutrients, and mitigate ocean acidification. *Reviews of Geophysics* 51, 113–149. doi: 10.1002/rog.20004

Heřmanská, M., Voigt, M. J., Marieni, C., Declercq, J., and Oelkers, E. H. (2022). A comprehensive and internally consistent mineral dissolution rate database: Part I: Primary silicate minerals and glasses. *Chem Geol* 597. doi: 10.1016/j.chemgeo.2022.120807

Holzer, I. O., Nocco, M. A., and Houlton, B. Z. (2023). Direct evidence for atmospheric carbon dioxide removal via enhanced weathering in cropland soil. *Environ Res Commun* 5, 101004. doi: 10.1088/2515-7620/acfd89

Iff, N., Renforth, P., and Pogge von Strandmann, P. A. E. (2024). The dissolution of olivine added to soil at 32°C: the fate of weathering products and its implications for enhanced weathering at different temperatures. *Frontiers in Climate* 6, 1252210. doi: 10.3389/fclim.2024.1252210

Jerden, J., Mejbel, M., Filho, A. N. Z., Carroll, M., and Campe, J. (2024). The impact of geochemical and life-cycle variables on carbon dioxide removal by enhanced rock

weathering: Development and application of the Stella ERW model. *Applied Geochemistry* 167, 106002. doi: 10.1016/j.apgeochem.2024.106002

Kantola, I. B., Blanc-Betes, E., Masters, M. D., Chang, E., Marklein, A., Moore, C. E., et al. (2023). Improved net carbon budgets in the US Midwest through direct measured impacts of enhanced weathering. *Glob Chang Biol* 29, 7012–7028. doi: 10.1111/gcb.16903

Kantzas, E. P., Martin, M. V., Lomas, M. R., Eufrasio, R. M., Renforth, P., Lewis, A. L., et al. (2022). Substantial carbon drawdown potential from enhanced rock weathering in the United Kingdom. *Nat Geosci* 15, 382–389. doi: 10.1038/s41561-022-00925-2

Kanzaki, Y., Planavsky, N. J., Zhang, S., Jordan, J., and Reinhard, C. T. (2024). Soil cation storage as a key control on the timescales of carbon dioxide removal through enhanced weathering. *Earths Future*, 1–19.

Kelland, M. E., Wade, P. W., Lewis, A. L., Taylor, L. L., Sarkar, B., Andrews, M. G., et al. (2020). Increased yield and CO_2 sequestration potential with the C4 cereal Sorghum bicolor cultivated in basaltic rock dust-amended agricultural soil. *Glob Chang Biol* 26, 3658–3676. doi: 10.1111/gcb.15089

Knapp, W. J., Stevenson, E. I., Renforth, P., Ascough, P. L., Knight, A. C. G., Bridgestock, L., et al. (2023). Quantifying CO_2 removal at enhanced weathering sites: A multiproxy approach. *Environ Sci Technol* 57, 9854–9864. doi: 10.1021/acs.est.3c03757

Koseva, I. S., Watmough, S. A., and Aherne, J. (2010). Estimating base cation weathering rates in Canadian forest soils using a simple texture-based model. *Biogeochemistry* 101, 183–196. doi: 10.1007/s10533-010-9506-6

Lackner, K. S., Wendt, C. H., Butt, D. P., Joyce, E. L., and Sharps, D. H. (1995). Carbon dioxide disposal in carbonate minerals. *Energy* 20, 1153–1170.

Lewis, A. L., Sarkar, B., Wade, P., Kemp, S. J., Hodson, M. E., Taylor, L. L., et al. (2021). Effects of mineralogy, chemistry and physical properties of basalts on carbon capture potential and plant-nutrient element release via enhanced weathering. *Applied Geochemistry* 132, 105023. doi: 10.1016/j.apgeochem.2021.105023

Liu, W., Song, Y., Men, X., Chen, Z., Chang, H., Zhang, S., et al. (2024). Spatio-temporal response and projection of CO_2 capture rates by different rock weathering to climate change in subtropics in China Chunjun Tao Geological Survey Institute of Anhui Province. *[Preprint]*. doi: 10.21203/rs.3.rs-3961192/v1

Lu, P., Apps, J., Zhang, G., Gysi, A., and Zhu, C. (2024). Knowledge gaps and research needs for modeling CO_2 mineralization in the basalt- CO_2-water system: A review of laboratory experiments. *Earth Sci Rev* 254, 104813. doi: 10.1016/j.earscirev.2024.104813

Maxbauer, D. P., and Yambing, J. R. (2022). Carbon sequestration by enhanced silicate weathering in agricultural soils. *Keck Geology Consortium* 34, 1–5.

McDermott, F., Barros, R., and Cooper, M. (2019). An investigation of waste basalt (quarry dust) as a soil amedment to sequester atmospheric CO_2., in *Geophysical Research Abstracts 21: EGU2019-5908-1*.

McDermott, F., Bryson, M., Magee, R., and van Acken, D. (2024). Enhanced weathering for CO_2 removal using carbonate-rich crushed returned concrete; a pilot study from SE Ireland. *Applied Geochemistry* 169, 106056. doi: 10.1016/j.apgeochem.2024.106056

Miller, V. S., and Naeth, M. A. (2017). Amendments and substrates to develop anthroposols for northern mine reclamation. *Can J Soil Sci* 97, 266–277. doi: 10.1139/cjss-2016-0145

MOE (1979). Rationale for the establishment of Ontario's provincial water quality objectives.

Oelkers, E. H., Declercq, J., Saldi, G. D., Gislason, S. R., and Schott, J. (2018). Olivine dissolution rates: A critical review. *Chem Geol* 500, 1–19. doi: 10.1016/j.chemgeo.2018.10.008

Paessler, D., Steffens, R., Hammes, J., and Smet, I. (2023). Monitoring CO_2 concentrations in soil gas: A novel MRV approach for cropland-based ERW? Available at: www.carbon-drawdown.de

Palandri, J. L., and Kharaka, Y. K. (2004). A compilation of rate parameters of water-mineral interaction kinetics for application to geochemical modeling. Denver.

Paulo, C., Power, I. M., Zeyen, N., Wang, B., and Wilson, S. A. (2023). Geochemical modeling of CO_2 sequestration in ultramafic mine wastes from Australia, Canada, and South Africa: Implications for carbon accounting and monitoring. *Applied Geochemistry* 152, 105630. doi: 10.1016/j.apgeochem.2023.105630

Phelan, J., Belyazid, S., Kurz, D., Guthrie, S., Cajka, J., Sverdrup, H., et al. (2014). Estimation of soil base cation weathering rates with the PROFILE model to determine critical loads of acidity for forested ecosystems in Pennsylvania, USA: Pilot application of a potential national methodology. *Water Air Soil Pollut* 225. doi: 10.1007/s11270-014-2109-4

Pogge von Strandmann, P. A. E., Tooley, C., Mulders, J. J. P. A., and Renforth, P. (2022). The dissolution of olivine added to soil at 4°C: Implications for enhanced weathering in cold regions. *Frontiers in Climate* 4, 827698. doi: 10.3389/fclim.2022.827698

Renforth, P., Pogge von Strandmann, P. A. E., and Henderson, G. M. (2015). The dissolution of olivine added to soil: Implications for enhanced weathering. *Applied Geochemistry* 61, 109–118. doi: 10.1016/j.apgeochem.2015.05.016

Rinder, T., and von Hagke, C. (2021). The influence of particle size on the potential of enhanced basalt weathering for carbon dioxide removal - Insights from a regional assessment. *J Clean Prod* 315. doi: 10.1016/j.jclepro.2021.128178

Seifritz, W. (1990). CO_2 disposal by means of silicates. *Nature* 345, 486. doi: 10.1038/345486b0

Strefler, J., Amann, T., Bauer, N., Kriegler, E., and Hartmann, J. (2018). Potential and costs of carbon dioxide removal by enhanced weathering of rocks. *Environmental Research Letters* 13. doi: 10.1088/1748-9326/aaa9c4

Stubbs, A. R., Paulo, C., Power, I. M., Wang, B., Zeyen, N., and Wilson, S. A. (2022). Direct measurement of CO_2 drawdown in mine wastes and rock powders: Implications for enhanced rock weathering. *International Journal of Greenhouse Gas Control* 113, 103554. doi: 10.1016/j.ijggc.2021.103554

Sutherland, K., Matlin-Wainer, M., Holme, E., He, J., Savage, R., Marsland, E., et al. (2023). Enhanced weathering in agriculture v1.0 – Isometric. 1–148. Available at: https://registry.isometric.com/protocol/enhanced-weathering-agriculture (Accessed March 10, 2024).

Sverdrup, H. U., Oelkers, E., Erlandsson Lampa, M., Belyazid, S., Kurz, D., and Akselsson, C. (2019). Reviews and synthesis: Weathering of silicate minerals in soils and watersheds: Parameterization of the weathering kinetics module in the PROFILE and ForSAFE models. *Biogeosciences Discussions*, 1–58. doi: 10.5194/bg-2019-38

Sverdrup, H., and Warfvinge, P. (1992). PROFILE - A mechanistic geochemical model for calculation of field weathering rates., in *International symposium on water-rock interaction*, (Park City: A.A. Balkema, Rotterdam), 585–590.

Sverdrup, H., and Warfvinge, P. (1993). Calculating field weathering rates using a mechanistic geochemical model PROFILE. *Applied Geochemistry* 8, 273–283.

Swoboda, P., Döring, T. F., and Hamer, M. (2022). Remineralizing soils? The agricultural usage of silicate rock powders: A review. *Science of the Total Environment* 807, 150976. doi: 10.1016/j.scitotenv.2021.150976

Taylor, L. L., Quirk, J., Thorley, R. M. S., Kharecha, P. A., Hansen, J., Ridgwell, A., et al. (2016). Enhanced weathering strategies for stabilizing climate and averting ocean acidification. doi: 10.1038/NCLIMATE2882

te Pas, E. E. E. M., Hagens, M., and Comans, R. N. J. (2023). Assessment of the enhanced weathering potential of different silicate minerals to improve soil quality and sequester CO_2. *Frontiers in Climate* 4, 954064. doi: 10.3389/fclim.2022.954064

ten Berge, H. F. M., van der Meer, H. G., Steenhuizen, J. W., Goedhart, P. W., Knops, P., and Verhagen, J. (2012). Olivine weathering in soil, and its effects on growth and nutrient uptake in ryegrass (Lolium perenne L.): A pot experiment. *PLoS One* 7. doi: 10.1371/journal.pone.0042098

Vandeginste, V., Lim, C., and Ji, Y. (2024). Exploratory review on environmental aspects of enhanced weathering as a carbon dioxide removal method. *Minerals* 14. doi: 10.3390/min14010075

Vienne, A., Poblador, S., Portillo-Estrada, M., Hartmann, J., Ijiehon, S., Wade, P., et al. (2022). Enhanced weathering using basalt rock powder: Carbon sequestration, co-benefits and risks in a mesocosm study with solanum tuberosum. *Frontiers in Climate* 4, 869456. doi: 10.3389/fclim.2022.869456

Vink, J., Giesen, D., and Ahlrichs, E. (2022). Olivine weathering in field trials.

Vink, J. P. M., and Knops, P. (2023). Size-fractionated weathering of olivine, its CO_2-sequestration rate, and ecotoxicological risk assessment of nickel release. *Minerals* 13. doi: 10.3390/min13020235

White, A. F., Blum, A. E., Bullen, T. D., Vivit, D. V, Schulz, M., and Fitzpatrick, J. (1999). The effect of temperature on experimental and natural chemical weathering rates of granitoid rocks.

Chapter 4
Conclusions

Widespread deployment of negative emission technologies (NETs) is recognized as the only approach to reduce the cumulated CO_2 in the atmosphere (Hoegh-Guldberg et al., 2018). Natural rock weathering plays a crucial role in regulating the carbon cycle, annually removing ~1 Gt of the estimated 35 Gt CO_2e generated by human activities (Strefler et al., 2018; Liu et al., 2023). Enhanced rock weathering (ERW) represents one such NET that capitalizes on this natural process, aiming to accelerate the rate of CO_2 removal (CDR) by increasing the exposure of rocks to CO_2 through comminution and dispersal across terrestrial lands. Recent advancements in ERW research have transitioned from laboratory and controlled environment experimentation to full-scale field trials (Larkin et al., 2022; Beerling et al., 2024; Honvault et al., 2024; McDermott et al., 2024). However, quantifying the carbon removed remains challenging and variable, contributing to significant uncertainties (Clarkson et al., 2024). This thesis endeavoured to evaluate environmentally safe mine wastes as a potential feedstock alternative used in ERW projects, while improving understandings of carbon accounting in an open system. Through field experimentation and using porewater chemistry as a direct approach for measuring carbon, the solubility trapping rates of processed kimberlite and powdered olivine could be quantified.

4.1 Summary of research outcomes

The research conducted in Chapter 2 demonstrated that monitoring porewater dissolved inorganic carbon (DIC), coupled with a water budget, provides a direct measure

of CO_2 removed as HCO_3^- (i.e., solubility trapping). The rapid generation of DIC correlated with increased kimberlite application and remained elevated for 3 yr post-application; however, these plots were equipped with high feedstock dosages (100–400 t/ha) to ensure signal detection. Prior to the field experiment, batch leaching and principal component analysis (PCA) of leachates identified unique cations sourced from field soils and kimberlite residues. Monitoring these cations allowed for partitioning of the total CO_2 removal derived from DIC into contributions from mineral weathering (e.g., soil minerals vs. kimberlite minerals), establishing carbonates as the predominant contributor due to their faster dissolution rates.

Secondly, Chapter 2 evaluated processed kimberlite residues as a potential ERW feedstock, assessing CO_2 removal efficiency, metal (Ni and Cr) leaching, and potential nutrient (K) release. Regardless of application rate, kimberlite-amended plots showed CO_2 removal rates at least double that of the control. Ni concentrations were elevated in porewaters, but within environmental regulations, and >99.9% of Cr was retained, consistent with batch leach results. Kimberlite residues hold promise as a potential K-source, suggesting applications in land reclamation, whereby this diamond mine waste could be spread at the mine site for post-closure remediation or transported off-site as a globally abundant ERW feedstock.

Thirdly, Chapter 2 highlighted the complexity of differentiating mineral trapping sources from the calcareous soils and carbonate-bearing amendment. Total inorganic carbon (TIC) was measured throughout the soil profile of the control and amended plots in the second and third monitoring period, where both amended plots yielded a significant increase in %C which equated to over 30 kg of carbonate precipitated. Despite significant

mineral trapping rates reported in several studies with inherent uncertainties (Manning et al., 2013; Haque et al., 2019; Vienne et al., 2022), improved methodologies are needed for accurate measurement, especially in heterogenous soil environments rich in carbonate minerals.

Chapter 3 simplified the experimental environment by amending soils with a monomineralic feedstock (powdered olivine), establishing grounds for better understanding feedstock weathering in complex soil environments. The mineral reactivity and porewater carbon accounting methods developed in Chapter 2 were applied, with results compared to previous ERW studies that used olivine. The estimated CO_2 removal rates were relatively low compared to reported literature values of controlled lab experiments (ten Berge et al., 2012; Renforth et al., 2015; Dietzen et al., 2018), attributed to the non-representative lab dissolution rates of field conditions, in addition to more acidic starting soils facilitating rapid weathering of olivine. Due to the simplicity of olivine cation release (Mg and Si only), cation exchange between soil Ca and olivine Mg was evident, with Si-fluxes used to determine olivine silicate weathering– deviating from traditional olivine dissolution study methods focusing on Mg fluxes (Amann et al., 2020; Almaraz et al., 2022; Dietzen and Rosing, 2023). Safety assessments of such high applications of alkaline minerals indicated minimal Ni and Cr leaching; however, potential for metal leaching remains a concern regarding plant uptake and accumulation in soil.

Chapter 3 research evaluated PROFILE with empirical data performing a sensitivity analysis to assess optimal characteristics regarding mineral applications and environmental conditions. Applying PROFILE for ERW has been mentioned (Taylor et

al., 2017), but this is the first time the model has been applied to an ERW field experiment. By simply inputting climatic, field site, and mineralogical data, the estimated (PROFILE) CO_2 consumption by soil was relatively agreeable with field rates, whereas olivine weathering rates and extrapolated CDR were several orders of magnitude slower. Critical PROFILE input parameters influencing results included climatic and environmental variables (temperature and soil moisture), and most critically mineral surface area. This sensitivity analysis confirmed underestimation of amendment weathering by using specific surface area as a three-order-of-magnitude increase – likely more representative eof reactive mineral surface area – was required to attain empirical rates. There is potential for PROFILE use in ERW projects, particularly in predicting natural soil CO_2 consumption and weathering rates during site assessment, which could aid in CDR rate partitioning.

4.2 Recommendations for designing a large-scale ERW deployment

4.2.1 Characterization and reactivity assessment

Acquisition of feedstocks for ERW projects relies heavily on the availability of materials within the vicinity of the deployment site. Chapter 2 demonstrated that crushed mafic or ultramafic rock from mining activities could serve as an effective and abundantly produced ERW feedstock, thereby addressing both local waste management issues and feedstock procurement challenges when upscaling projects. When multiple feedstock options are available, an initial characterization and reactivity assessment of each feedstock and the site soil via batch leaching with CO_2 should ideally be conducted.

Each system can be divided into four mineralogical categories: soil carbonate, soil silicate, amendment carbonate, and amendment silicate. The dominant minerals (i.e., fastest weathering) in each category will preferentially release certain cations, which can be identified through the reactivity assessment. To assess mineral weathering, safety concerning metal leaching, and potential nutrient release, principal component analysis (PCA) of leachate data discerns correlations between element release and material influence. Under enhanced conditions (e.g., high temperatures, agitation, constant CO_2 supply), the mineral weathering in various soil-to-amendment mixtures will release significant quantities of weatherable base cations, nutrients, and potentially harmful elements. PCA of the leachate data can help to determine unique tracer cations, that indicate the weathering of specific mineral phases, the feedstock capacity for nutrient provision and metal release, and the predominance of certain minerals (e.g., Mg and Si vector overlap indicates Mg-silicate dissolution). Thus, through this comprehensive evaluation, feedstocks are assessed for their reactivity at a given site, providing measurable indicators for effective field application.

4.2.2 Initial site protocols

Before amending a deployment site for ERW, a baseline for soil mineralogy, soil CDR capacity contributed by pre-existing minerals, general site hydrology (e.g., slope influence), and metal concentrations must be established. Sutherland et al. (2023), the Isometric team, suggested thorough soil sampling across the site to ensure that the control zone — the region to remain unamended — accurately represents the site. Given the inherent heterogeneity of soil, it is expected that there will be variability in chemical

characteristics. Isometric recommends collecting one 30 cm soil core per hectare, leaving 5% of the project area as a control zone.

In flat application sites, such as the field experiments deployed in this thesis, monitoring plots at a frequency of one per hectare may suffice. The separate control plots in Chapter 2 and Chapter 3 yielded similar annual solubility trapping rates despite variations in surface vegetation and distance from one another. Although methods for monitoring mineral trapping requires refinement, initial total inorganic carbon analysis of soil cores can identify potential carbonate-rich locations, while XRD can determine the dominant carbonate phases in the environment.

Isometric suggests two in-field monitoring approaches: the 2-plot method, where a small, unamended area is used as a control and the remainder is amended and comprehensively monitored, and the 3-plot method, where only a small, representative area of the treated field is monitored (see Fig. 4.1 for 3-plot method). This thesis proposes a third approach that involves a series of small plots with dosages ranging from that of the larger field to very high dosages (e.g., 2×, 5×, and 10×). These plots would primarily ensure CDR detection and predict porewater chemistry outcomes following site reamendment (Fig. 4.1). Although, these plots could also be used to assess soil degradation from metal accumulation as a result of re-amendment of the site. It is recommended that one series of comprehensively monitored research plots are established with application rates ranging from 100–400 t/ha over square metre plots. These plots should be implemented prior to full deployment and monitored for one year alongside the control area to evaluate feedstock weathering in the given climate relative to baseline CDR rates.

In addition to these initial site determination protocols, PROFILE modelling can be utilized to predict the impact of climate on feedstock weathering and soil CDR based on feedstock characterization and baseline site data. By incorporating mineralogical, hydrological, and climatic inputs into the PROFILE model, adjustments to the amendment layer can be made to optimize CDR, such as modifying the mineral surface area, depth of the amendment layer, and soil moisture levels.

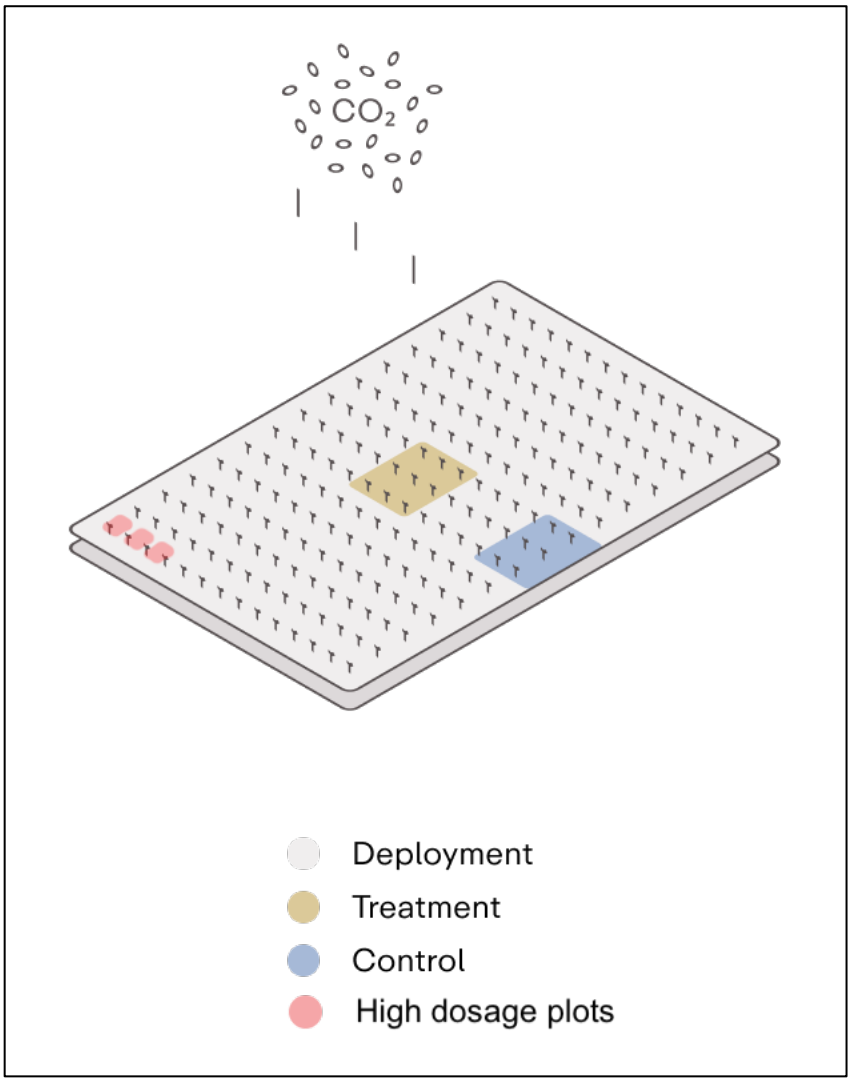

Figure 4.1. Schematic of in-field monitoring approach illustrating the relative size of the control, treatment, deployment, and high dosage research plots in the 3-plot approach. Schematic is modified from Sutherland et al. (2023).

4.2.3 Carbon monitoring

After the application of feedstocks, monitoring carbon dynamics primarily involves porewater sampling coupled with a water budget derived from moisture probes placed in representative monitoring plots. In neutral pH environments, DIC is typically composed mainly of alkalinity. Therefore, all water samples must be analyzed for DIC. By averaging these concentrations monthly, these data can be integrated into the water budget to quantify the amount of DIC percolating from the system, thereby determining the total CDR by solubility trapping across the site.

To allocate the total CDR among various mineral contributions, mineral phases respective cation releases determined by batch leaching tests can be assessed relative to one another. Weathering of the soil and feedstock will favour the release of certain cations; for example, Mg and Si will be more prominent in matrices rich in Mg-silicates. The combined CDR rates from soil carbonates, soil silicates, feedstock carbonates, and feedstock silicates will generally exceed the DIC rate, reflecting the maximum removal capacity. Thus, the percentage contribution of each mineral category can be used to partition the DIC value into contributions from different mineral weathering processes. This approach allows for a more precise measurement of CO_2 removal, enabling direct comparisons across different rock types and field sites, rather than relying on indirect proxies like the volume of material weathered.

Mineral trapping can be a significant contributor to net CDR in ERW deployments (Manning et al., 2013; Haque et al., 2020), albeit less effective than solubility trapping, but still requires a more reliable method for detecting small quantities of TIC generation. At sites lacking pre-existing carbonates, this signal may be easily

detected. However, this thesis highlights the complexities of ERW applications at sites with high carbonate content in the soil. Chapter 2 demonstrated the utility of ^{13}C compositions to distinguish between carbon sources in DIC, determining the primary source of carbon removed being that of organic origin from soil respiration. Radiocarbon measurements offer an improved correlation with carbon sources sequestered by ERW, refining estimates derived from stable C and O isotopes, which often reflect a mix of geologic sources of carbon (Knapp et al., 2023). Although more costly, annual isotopic measurements could provide a more accurate assessment of new carbonate sources and enhance our understanding of the CDR process.

Incorporating ERW protocols into the mining industry framework could solve concerns with regards to sufficient material acquisition as CDR technologies approach global implementation. In-field monitoring of environmentally safe mine residues spread over the mine land footprint and in some cases the surrounding areas, could scale up CDR to achieve carbon-neutral operations. However, there needs to be a shift in carbon accounting efforts from weathering proxies to direct measurements of carbon in order to improve accuracy of reported rates while expanding to industry collaboration.

4.3 References

Almaraz, M., Bingham, N. L., Holzer, I. O., Geoghegan, E. K., Goertzen, H., Sohng, J., et al. (2022). Methods for determining the CO_2 removal capacity of enhanced weathering in agronomic settings. *Frontiers in Climate* 4:970429, 1–18. doi: 10.3389/fclim.2022.970429

Amann, T., Hartmann, J., Struyf, E., De Oliveira Garcia, W., Fischer, E. K., Janssens, I., et al. (2020). Enhanced Weathering and related element fluxes - A cropland mesocosm approach. *Biogeosciences* 17, 103–119. doi: 10.5194/bg-17-103-2020

Beerling, D. J., Epihov, D. Z., Kantola, I. B., Masters, M. D., Reershemius, T., Planavsky, N. J., et al. (2024). Enhanced weathering in the US Corn Belt delivers carbon removal with agronomic benefits. *Proc Natl Acad Sci U S A* 121. doi: 10.1073/pnas.2319436121

Clarkson, M. O., Larkin, C. S., Swoboda, P., Reershemius, T., Suhrhoff, T. J., Maesano, C. N., et al. (2024). A review of measurement for quantification of carbon dioxide removal by enhanced weathering in soil. *Frontiers in Climate* 6, 1345224. doi: 10.3389/fclim.2024.1345224

Dietzen, C., Harrison, R., and Michelsen-Correa, S. (2018). Effectiveness of enhanced mineral weathering as a carbon sequestration tool and alternative to agricultural lime: An incubation experiment. *International Journal of Greenhouse Gas Control* 74, 251–258. doi: 10.1016/j.ijggc.2018.05.007

Dietzen, C., and Rosing, M. T. (2023). Quantification of CO_2 uptake by enhanced weathering of silicate minerals applied to acidic soils. *International Journal of Greenhouse Gas Control* 125, 103872. doi: 10.1016/j.ijggc.2023.103872

Haque, F., Santos, R. M., and Chiang, Y. W. (2020). CO_2 sequestration by wollastonite-amended agricultural soils – An Ontario field study. *International Journal of Greenhouse Gas Control* 97. doi: 10.1016/j.ijggc.2020.103017

Haque, F., Santos, R. M., Dutta, A., Thimmanagari, M., and Chiang, Y. W. (2019). Co-benefits of wollastonite weathering in agriculture: CO_2 sequestration and promoted plant growth. *ACS Omega* 4, 1425–1433. doi: 10.1021/acsomega.8b02477

Hoegh-Guldberg, O., Jacob, D., Taylor, M., Bindi, M., Brown, S., Camilloni, I., et al. (2018). *Impacts of 1.5oC of global warming on natural and human systems. In: Global warming of 1.5°C. An IPCC special report on the impacts of global warming of 1.5°C above pre-industrial levels and related global greenhouse gas emission pathways, in the context of strengthening the global response to the threat of climate change, sustainable development, and efforts to eradicate poverty.*, eds. V. Masson-Delmotte, P. Zhai, H.-O. Pörtner, D. Roberts, J. Skea, P. R. Shukla, et al.

Honvault, N., Tiouchichine, M. L., Sauze, J., Piel, C., Landais, D., Devidal, S., et al. (2024). Additive effects of basalt enhanced weathering and biochar co-application on carbon sequestration, soil nutrient status and plant performance in a mesocosm experiment. *Applied Geochemistry* 169, 106054. doi: 10.1016/j.apgeochem.2024.106054

Knapp, W. J., Stevenson, E. I., Renforth, P., Ascough, P. L., Knight, A. C. G., Bridgestock, L., et al. (2023). Quantifying CO_2 removal at enhanced weathering sites: A multiproxy approach. *Environ Sci Technol* 57, 9854–9864. doi: 10.1021/acs.est.3c03757

Larkin, C. S., Andrews, G. M., Pearce, C. R., Yeong, K. L., Beerling, D. J., Bellamy, J., et al. (2022). Quantification of CO_2 removal in a large-scale enhanced weathering field trial on an oil palm plantation in Sabah, Malaysia. *Frontiers in Climate* 4:959229, 1–20.

Liu, Z., Deng, Z., Davis, S., and Ciais, P. (2023). Monitoring global carbon emissions in 2022. *Nat Rev Earth Environ* 4, 205–206. doi: 10.1038/s43017-023-00406-z

Manning, D. A. C., Renforth, P., Lopez-Capel, E., Robertson, S., and Ghazireh, N. (2013). Carbonate precipitation in artificial soils produced from basaltic quarry fines and composts: An opportunity for passive carbon sequestration. *International Journal of Greenhouse Gas Control* 17, 309–317. doi: 10.1016/j.ijggc.2013.05.012

McDermott, F., Bryson, M., Magee, R., and van Acken, D. (2024). Enhanced weathering for CO_2 removal using carbonate-rich crushed returned concrete; a pilot study from SE Ireland. *Applied Geochemistry* 169, 106056. doi: 10.1016/j.apgeochem.2024.106056

Renforth, P., Pogge von Strandmann, P. A. E., and Henderson, G. M. (2015). The dissolution of olivine added to soil: Implications for enhanced weathering. *Applied Geochemistry* 61, 109–118. doi: 10.1016/j.apgeochem.2015.05.016

Strefler, J., Amann, T., Bauer, N., Kriegler, E., and Hartmann, J. (2018). Potential and costs of carbon dioxide removal by enhanced weathering of rocks. *Environmental Research Letters* 13. doi: 10.1088/1748-9326/aaa9c4

Sutherland, K., Matlin-Wainer, M., Holme, E., He, J., Savage, R., Marsland, E., et al. (2023). Enhanced weathering in agriculture v1.0 – Isometric. 1–148. Available at: https://registry.isometric.com/protocol/enhanced-weathering-agriculture (Accessed March 10, 2024).

Taylor, L. L., Beerling, D. J., Quegan, S., and Banwart, S. A. (2017). Simulating carbon capture by enhanced weathering with croplands: an overview of key processes highlighting areas of future model development. *Biol Lett* 13, 20160868. doi: 10.1098/rsbl.2016.0868

ten Berge, H. F. M., van der Meer, H. G., Steenhuizen, J. W., Goedhart, P. W., Knops, P., and Verhagen, J. (2012). Olivine weathering in soil, and its effects on growth and nutrient uptake in ryegrass (Lolium perenne L.): A pot experiment. *PLoS One* 7. doi: 10.1371/journal.pone.0042098

Vienne, A., Poblador, S., Portillo-Estrada, M., Hartmann, J., Ijiehon, S., Wade, P., et al. (2022). Enhanced weathering using basalt rock powder: Carbon sequestration, co-benefits and risks in a mesocosm study with solanum tuberosum. *Frontiers in Climate* 4, 869456. doi: 10.3389/fclim.2022.869456